A thesis submitted in partial fulfilment
of the requirements for the degree of
Master of Engineering
in
Electrical and Computer Engineering
at the
University of Canterbury,
Christchurch, New Zealand.
2015

Thermal Modelling and Optimisation of Building-Integrated Photo-Voltaic Thermal Systems

---

Alastair MCDOWELL

Supervisors:
Dr. Christopher E. Hann
Assoc. Prof. Greg Macrae
Dennis Chapman

June 30, 2015

Dedicated to Nan,

Abstract

This Masters project has involved detailed thermal analysis of a unique renewable energies building. A TRNSYS model of this building has been developed and validated by real measurements and has shown to be capable of accurately predicting room temperatures and total heat gain from a solar-thermal roofing system. Supporting experiments were conducted experimentally and numerically. An experimental solar thermal testing unit constructed for the purpose of validating the solar-thermal roof concept. This experimental apparatus has been used to evaluate the effect of various operating procedures on the total heat gain from the system under a range of meteorological conditions. The validated thermal building model is used to conduct long-term simulations to provide a measure of year-round thermal performance of the building and estimated gains from renewable energy systems. Similar techniques are used to assist in the design and optimisation of a new transportable sustainable building concept in association with StoneWood Homes. It was found that a $4.5kW$ BIVP/T system could supply the small building with 100% of the yearly electrical energy and space heating requirements.

Acknowledgements

The completion of this Masters of Engineering thesis could not have been achieved without the help of many people along the way. I would like to extend my gratitude to those who assisted me during this research project.

Firstly I would like to acknowledge Callaghan Innovation and DARC Technologies for their funding of this project.

Dennis Chapman, for providing the opportunity to study a unique renewable energy building. Many thanks for opening up your home for my various experiments, helping to explain the many systems and assisting in setting up the monitoring equipment. Your design intuition and ability to innovate new concepts has been inspirational.

Dr Chris Hann, for his guidance and advice through the modelling and validation stages of this project. His vision to initiate this project, secure funding and guide my research towards this point has been invaluable. His encouragement to strive for minimal modelling has challenged my modelling approach and I thank him for his helpful advice throughout the whole project.

Greg MacRae, Associate Professor in Civil Engineering, for his assistance with the fundamental building concepts.

Alan Chapman, for helping to secure funding for this project and the hard administrative work associated. Your knowledge of building design was a real asset, and your intuition of expected thermal dynamics in the building has helped me to be more critical of my work on many occasions.

Sean Cooney, fellow Masters student, for providing a sounding board and constructive ideas and feedback throughout this project. Thank you for your assistance with constructing the experimental testing apparatus, and for sharing his extensive practical knowledge and conceptual insights.

David Burkitt, Rob Stuart and Ben Greenway at DARC Technologies for their frequent help with setting up the hardware and software for the various experimental systems in this project.

Jeremy Osborne from Energy AE, for support with the TRNSYS software, and hosting me in Sydney during the AIRAH Solar Heating and Cooling conference. Thank you for introducing me to the beautiful world of solar thermal technology. Your advice in the final stages of the project was greatly appreciated.

My colleagues at the New Zealand Innovation Institute (NZi3), for their good

company during the year of this project. Working alongside so many other keen outdoors people has made this work environment a fun and enjoyable place to share stories of adventure and future plans.

Finally, a huge thanks to my family, for their support and guidance through the years of my education to this grand finale, which is really just the beginning. Each one of you have helped me in many special ways, and for that I'm deeply grateful.

Thanks to you all.

Alastair McDowell

June, 2015.

Contents

List of Figures

List of Tables

Nomenclature

Acronyms

BIPV/T	Building integrated photo-voltaic thermal
GUI	Guided user interface
HTC	Heat transfer coefficient
MATLAB	Matrix Laboratory
NIWA	National Institute of Water and Atmospheric research
PV	Photo-voltaic
SEL	Solar Energy Laboratory
TESS	Thermal Energy System Specialists
TMY	Typical meteorological year
TRNSYS	Transient system simulation

Symbols

a_1	thermal efficiency slope (-)
A	BIPV/T collector area (m^2)
C	concentration (ppm)
C_p	specific heat capacity ($J/kg.K$)
D_h	hydraulic diameter (m)
F_R	heat recovery factor (-)
G	solar radiation (W/m^2)
h	heat transfer coefficient ($W/m^2.K$)
I	infiltration ($1/hr$)
k	thermal conductivity ($W/m.K$), turbulent kinetic energy (J/kg)
k_T	clearness index (-)
L	collector length (m)
m	mass (kg)

$\dot{m}$	air mass flow rate (kg/s)
Nu	Nusselt number (-)
Pr	Prandtl number (-)
$\dot{Q}$	energy rate / power (W);
R	thermal resistance $(m^2.K/W)$
R^2	regression correlation coefficient (-)
R_B	geometric factor (-)
Re	Reynolds number (-)
S	absorbed solar radiation
P	pressure (Pa)
t	time (s)
T	air temperature ($^\circ$C)
U	heat loss coefficient $(W/m^2.K)$
V	wind velocity (m/s)
W	collector width (m)
x	distance (m)
V	volume (m^3)

Greek Symbols

α	absorptivity (-)
β	collector tilt angle ($^\circ$)
δ	boundary layer thickness (m), solar declination angle ($^\circ$)
ϵ	emissivity (-), turbulent dissipation rate $(J/kg.s)$
η	efficiency (-)
η_0	collector optical efficiency (-)
ν	kinematic viscosity (m^2/s)
μ	dynamic viscosity $(kg/m.s)$, mean (-)
ω	solar hour angle ($^\circ$)
ρ	density (kg/m^3)
σ	Stefan-Boltzmann constant $(W/m^2.K^4)$, standard deviation (-)
τ	transmissivity (-)
θ	angle ($^\circ$)

Subscripts

0	initial, extra-terrestrial
amb	ambient

av	average
b	beam
c	collector
d	diffuse
in	inlet, input
max	maximum
out	outlet, output
T	total
u	useful
w	window
Z	zenith
$*$	perturbed

Chapter 1

Introduction and Motivation

1.1 Introduction

Sustainable building systems are becoming increasingly popular in the design of low energy homes. Maximising the use of the solar energy resource through passive and active technologies is one of the best ways to reduce domestic energy requirements for space and water heating. A study into energy use in New Zealand households revealed space heating and hot water accounts for 34% and 29% of total energy usage respectively (BRANZ 2006). Renewable sources have the potential to meet these requirements in a sustainable way.

Photo-voltaics currently lead the way towards achieving truly self sustainable buildings. Current solar photo-voltaic (PV) systems are able to absorb as much as 80% of incident solar radiation, yet they are only capable of converting up to 20% of this total solar radiation to electricity. The remaining energy is lost due to conversion to heat. During peak operation, PV cells reach temperatures of up to 50°C, which reduces their electrical efficiency and degrades the PV cell over time. Standard PV installations combat this by allowing a certain air gap between the PV panels and the roof surface to which they are mounted. However, for countries with a good solar resource but also a significant heating demand, this thermal energy, which is otherwise wasted to the ambient air, can be harnessed in a useful way. Systems designed to simultaneously generate both electrical and thermal energy from the sun are known as photo-voltaic/thermal (PV/T).

A large range of PV/T systems have been developed worldwide, which all operate under the same principle - harnessing the wasted heat from the back

of PV panels as useful thermal energy that can be used in a wide variety of applications, such as air space heating, drying, water pre-heating. The hybrid generation of both electrical and thermal energy is a revolutionary idea that can greatly increase the overall efficiency of PV installations.

However, retro-fitting renewable energy systems on buildings is prohibitively expensive, thus it is important to integrate these systems into new designs for a more cost-effective solution. By incorporating a PVT system into the initial design, building integrated photo-voltaic/thermal systems (BIPV/T) can form a cohesive design, construction and energy solution for a building (Bazilian et al. 2001).

Both air and water are used as the PV-cooling agent and have respective advantages and disadvantages. While water provides better thermal performance, air systems require less maintenance and are easier and less expensive to implement. Air can then be used as the sole agent to heat the building. An effective strategy to raise the building's core temperature is to cycle air from inside the building through the BIPV/T system and ventilate the heated air back into the room.

Thermal storage is equally as important in the building design to ensure that the heat harnessed during cold, sunny days can be retained within the building. Incorporating thermal mass into the building achieves this by absorbing the warm ventilated air into the core of the structure, and also prevents the building from overheating during BIPV/T operation.

Figure 1.1: Building integrated photovoltaic panels on the Dennis Chapman Eco-Castle, Tai Tapu, Christchurch.

1.2 Literature

Energy efficient homes and residential renewable energy systems have been a popular research subject over the past thirty years.

Chen et al. (2010) investigated a building-integrated photovoltaic-thermal (BIPV/T) system thermally coupled with a ventilated concrete slab (VCS) in a prefabricated, two-storey detached, low energy solar house in Canada. Detailed numerical models were developed for the linked systems, and results indicate that the overall system had a thermal efficiency of 20%. As a result of this innovative design, the building's annual space heating energy consumption is 5% of the national average.

A number of researchers have used an experimental process to assist computational studies of a full scale system and to determine the thermal and electrical performance of a BIPV/T system. Experiments are carried out both indoor and outdoor, each have respective advantages and disadvantages.

(Solanki et al. 2009) developed and performed a controlled indoor test procedure for a photovoltaic thermal air collector so that manufacturers could analyse different types of PV modules to optimise their products.

Diarra et al. (2008) carried out an experimental study of the air flow and heat transfer coefficients for roof-integrated PV/T systems. Their tests included a *Particle Image Velocity* (PIV) device to accurately measure air mass flow rate. Thermocouples were placed along the duct to measure the temperature distribution. A heated top plate simulated the solar radiant heat flux. The results were used to validate a detailed CFD study on the convective heat transfer coefficients in the duct for a range of design parameters and operating conditions (Candanedo et al. 2010).

Indoor testing has also been used to test the performance of various manufacturer's PV modules when set up for an air based PVT configuration (Solanki et al. 2009).

BIPV/T systems have been studied computationally by many authors in numerous ways. The total rate of useful thermal energy generated can be determined analytically by solving a heat energy balance across the separate components of the structure. For more complex PVT structures, detailed information can be produced by using CFD software such as ANSYS-CFX.

Liao et al. (2007) performed a CFD analysis of a vertically mounted PVT system with a front inflow duct. CFD results showed how the inlet flow profile affected the heat transfer coefficients along the length of the PV module.

(a) Experimental apparatus used by Zogou & Stapountzis (2011) to validate their improved BIPV/T concept in Greece.

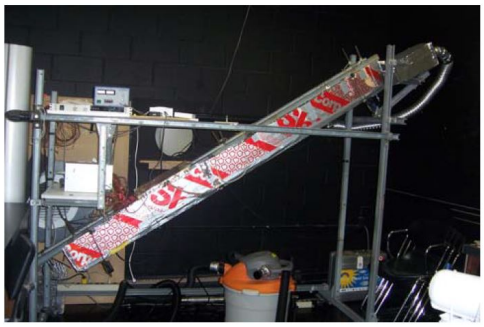

(b) Indoor experimental BIPV/T system designed by Diarra et al. (2008)

Figure 1.2: Other experimental BIPV/T systems used for validation purposes.

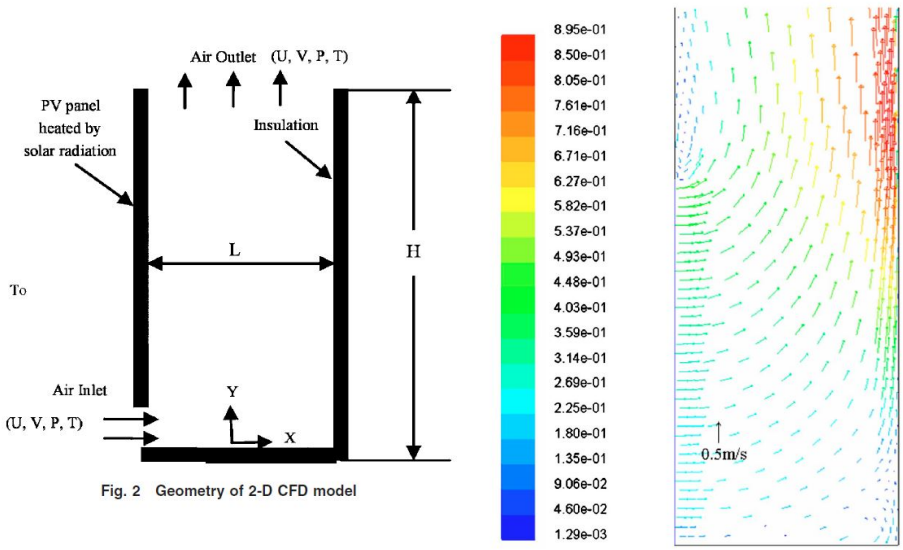

Figure 1.3: CFD analysis undertaken by Liao et al. (2007)

Chen et al. (2010) modelled the BIPV/T system as part of a building with a thermally-coupled concrete slab. His approach was to assume a quasi-two dimensional, control volume, steady state model of the air channel and PV

module, and used a finite difference system of equations to solve for the outlet air temperature.

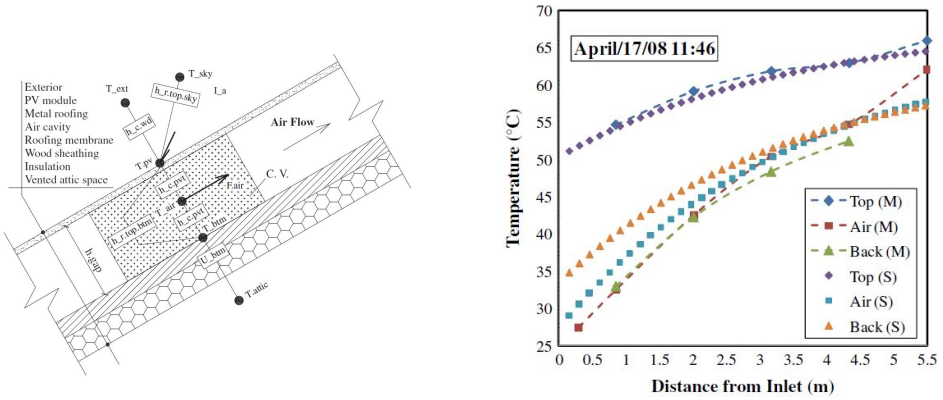

(a) Two dimensional BIPVT model used to discretise the system into a series of equations

(b) Validation results comparing simulated and measured temperatures along the length of the duct

Figure 1.4: Analytical approach used by Chen et al. (2010) to study a BIPVT system

Sweet & McLeskey Jr (2012) used TRNSYS to simulate an underground Seasonal Solar Thermal Energy Storage (SSTES), and Wahab et al. (2011) coupled the MATLAB/Simulink fuzzy logic control toolbox with TRNSYS to optimise control strategies for the air ventilation loop in a BIPV/T system.

Work has also been done to optimise the design of BIPV/T systems. Hegazy (1999) found an optimum channel height to length ratio for variable flow rates. Farshchimonfared et al. (2015) expanded on this concept by incorporating fan work into the optimisation function, and developed a new way of calculating overall energy output considering the value of the thermal energy relative to electrical energy. This work also established rules for the optimum mass flow rate relative to the collector area. However, few works have optimised these systems linked to a residential building with active control strategies, or optimised with regards to local year-round energy requirements.

Very little work on BIPV/T systems has been undertaken in New Zealand. Dr Tim Anderson of AUT is one of the leading researchers in this field and has carried out a detailed investigation into the thermal aspects of BIPV/T systems thus laying down the ground work for aspects that influence the thermal efficiency of the system (Anderson 2009). Dr Anderson has also investigated various processes for manufacturing BIPV/T systems.

Currently, there are very few suppliers or manufacturers of BIPV/T systems in New Zealand. SUNZ offer a retro-fit, hybrid PVT collector system (SUNZ 2015). For a building-integrated PVT to be implemented, the system must be built into the initial design. StoneWood Homes are among the first to adopt this design into their architectural plans.

There is a wide variety of work done on this subject world-wide, but in general not commercially implemented.

There exist many simulation programs designed to allow the user to simulate the thermal performance of a building and associated sustainable building systems. One of the major simulation programs available on the market is TRNSYS - a transient system simulation tool, developed by Duffie & Beckman (2013) and the Solar Energy Laboratory (SEL) at the University of Madison, with additional libraries written by Thermal Energy Systems Specialists (TESS). The software is available in New Zealand, distributed through an Australian energy consulting firm, EnergyAE (ENERGYAE 2015).

1.3 Motivation: Chapman Castle

The Chapman Residence is a unique building development in the sphere of renewable energy homes in New Zealand. The building features a wide range of automated systems across the sectors of electrical, water, HVAC and grid-tied solar. The 22.6 kW building-integrated solar roof provides the building with all required electricity as well as year-round solar heating and cooling. Inspiration and motivation behind the development is Dennis Chapman, director of Enatel Ltd, and DARC Technologies Ltd. The overall aim behind this work and future projects is to use existing and emerging technology to prove that all housing in the future can be built for minimal ongoing requirements from the outside world, while maintaining all the luxuries that society requires. These new ideas and new technologies will be made available for others to use (Chapman 2010).

Figure 1.5: North face of the Chapman Residence, Great Hall exterior

1.3.1 Building overview

The Chapman Castle site occupies a total area of 4.6 hectares, including 2 hectares of native forest, 2 hectares of paddocks, and 0.6 hectares for the house and garden. The building contains a total floor area of $1020m^2$ across 16 zones.

The architecture and furnishings are based on a medieval castle with detailed stonework, turreted balconies, gargoyles, a moat, and complete themed artwork and furniture. The northern roofs and walls of the building are constructed with 22.6kW of grid-tied building-integrated photo-voltaic panels. 17.6kW are tilted at 30° optimised for summer electricity production, and 5kW are vertical for maximum winter thermal gains. A building with solar panels integrated into the roof structure and built-in air ducting beneath the panels for the harvesting of hot air is known as a *building integrated photo-voltaic/thermal* or BIPV/T system. Two 15kW heat pumps in an attic space at the outlet of these air ducts allows either hot air to be circulated through the Great Hall, or heated water to be circulated through heated floor systems in other rooms of the Castle.

The basement holds a 12-car garage and a total of 123,000 L of water storage: 60,000 L non potable, 3,000 L potable, and 60,000 fire fighting and thermal storage.

The main level contains all the main zones available for ease of access: great hall, lounge, dining room, kitchen, 2 bedrooms, 2 bathrooms, 3 toilets, 2 car garage.

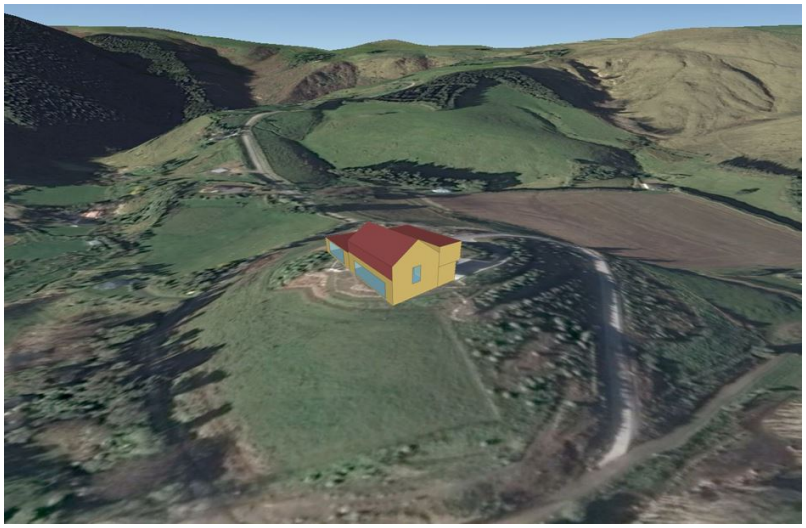

Figure 1.6: Sketchup model overlaid on Google Earth satellite image of building location, Tai Tapu, Christchurch

1.3.2 HVAC Systems

Water

The basement area located beneath the Great Hall is the water management hub. Four 30,000 L capacity water tanks supply water for fire spinklers and irrigation. A 1000 litre water tank is used for the supply loop to the BIPV/T heat pumps that take the heated air from the solar panel outlet ducts to produce heated water. This heated water is fed through the underfloor heating systems in six zones on the ground floor, including the Great Hall.

Figure 1.7: Water systems control room

Ventilation

Fresh air is ventilated through the Castle using three separate systems, located in the basement office, main floor and upstairs.

Forced ventilation is provided using counter cross flow heat exchangers. These exchangers are bypassed on cold summer nights to cool the house. Incoming air can be pre cooled using the same air to water heat pump as used for the potable hot water. Incoming air can also be preheated using water from the 60,000 L heat storage tank. The control system governing this ventilation uses various sensors measuring air temperature, humidity and carbon dioxide levels.

1.3.3 Great Hall Design

The Great Hall is the major focus area of this research as it contains a high proportion of the renewable energy systems. The building integrated photovoltaic thermal (BIPV/T) system is thermally coupled with the Great Hall and upper Balcony zone through the circulation of air through the input and output vents. A high thermal mass construction in the room ensures that during colder months, thermal gains are stored for longer periods of

time. Well sealed fittings ensure minimal infiltration losses. Floors consist of an upper level of concrete, and under-floor water-heated pipes within a 15MPa low-shrinkage concrete base with more insulation below. This under-floor heating system is used to increase the temperature of the thermal mass structure during winter.

Figure 1.8: Great Hall lay-out: (a) Balcony level air zone connection to the Great Hall. (b) Great Hall floor interior. Eight visible rectangular tapestries on the right wall form the bottom motorised flaps for the BIPV/T system.

1.4 Industry Partners

This Masters research project is sponsored by two leading corporate partners in the building industry.

1.4.1 DARC Technologies

DARC Technologies was formed in 2008 as a technology development company, funded by Dennis and Alan Chapman. The company's primary purpose was the development of electronic and thermal energy solutions to be deployed in the Chapman Castle. These solutions, if proven successful in the Chapman Castle, will be evaluated for future commercialisation, targeting both the domestic and commercial building industries.

1.4.2 Stonewood Homes

Stonewood Homes NZ Ltd are one of the largest home builders in New Zealand having built over 4000 homes throughout the country since being established in 1987. Christchurch is their largest market with build numbers rising explosively during the 'Christchurch Rebuild'. The head office is in Christchurch which houses multiple financial, administrative and technical staff to support the wider franchise network. Stonewood Homes currently offers 'green' energy efficient options when building a home with one of their show homes being the first to achieve a 7 Star Homestar rating. This project outlined in this report will add to the company's existing knowledge base in energy efficient housing.

In conjunction with this project, another Masters student, Sean Cooney, has been taken on by Stonewood Homes and DARC Technologies and will work on the structural design, implementation and testing of a self-contained, transportable building. This building will be highly energy efficient with the possibility of being entirely energy self-sufficient. The key philosophies employed are state-of-the-art insulation techniques and a large integrated partially-dynamic thermal mass.

1.4.3 Project personnel

Primary and co-supervisors and industry collaborators:

Chris Hann Senior Lecturer, Rutherford Discovery Fellow - Primary Supervisor

Greg MacRae Associate Professor, Civil Engineering - Co-supervisor

Dennis Chapman Director of Enatel Ltd - Industry supervisor

Alan Chapman Managing Director, DARC Technologies Ltd - Industry supervisor

1.5 Project Aims

The aim of the project as a whole is to utilise ideas and technology established in the construction of Dennis Chapmans Eco-Castle and combine them in to a smaller scale, commercially viable product.

The overall aim is to be able to predict the thermal performance of building integrated photo-voltaic thermal systems linked with residential buildings. Thermal performance relates to the quantity of thermal energy harnessed by the BIPV/T system under different climatic conditions, and the resulting thermal response of the building structure. This research will focus on the development of thermal models using TRNSYS to aid in the optimisation of building operation and design.

1.6 Thesis Structure

The thesis is divided into four sections. Chapter 2 describes the modelling methodology used throughout this thesis. Chapter 3 presents the results for the experimental BIPV/T model. Chapter 4 provides a detailed thermal analysis, validation and optimisation for the Chapman Castle Great Hall and BIPV/T system. Chapter 5 describes the transportable building concept and uses a simulation-based approach to optimise the design of the building and BIPV/T system.

Chapter 2

Modelling Methodology

2.1 Thermal Modelling Approach

The methodology comprises of two main areas of research: experimental and computational. The experimental section uses practical means to measure data and investigate existing systems used by the Chapman castle. The computational section models these systems to capture the measured response. These two distinct techniques mesh together during the important validation process where measured and simulated results are compared. Various techniques are then used to improve the computational model until a satisfactory fit is achieved. The computational model can then be applied with confidence to predict long-term thermal performance. The general method used can be summarised in a flow chart as shown in Figure 2.1.

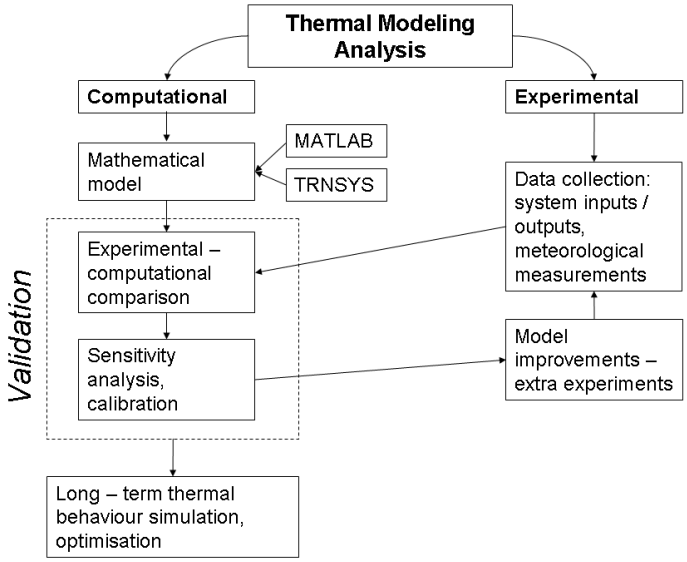

Figure 2.1: Thermal modelling method

The following sections give the basis of the tools used throughout this thesis. Section 2.2 gives an overview of the TRNSYS suite, section 2.4 describes the treatment of solar radiation in all thermal models, section 2.9 shows how MATLAB is linked with TRNSYS to automate simulations, and section 2.7 describes the overall energy balance calculation for BIPV/T systems, divided into thermal, electrical and hydraulic components.

2.2 TRNSYS

TRNSYS is a widely used software tool for conducting transient simulations of solar thermal energy systems. The mathematical representations of the components of the solar energy system are presented as algebraic or ordinary differential equation models, which the software interconnects depending on energy and mass flows.

2.2.1 TESS Libraries

The accompanying component libraries developed by TESS (Thermal Energy Systems Specialists) provide over 500 useful applications for building

energy modelling. Libraries include: electrical components (building integrated PV/thermal modules), ground coupling components (energy transfer between large thermal mass objects and air zones), and a large variety of standard and specialist HVAC components. All components in a TRNSYS model are wired together with respective inputs and outputs of required variables, analogous to the piping and ducting of the real system.

2.2.2 TRNSYS 3D

TRNSYS 3D is a plug-in application for Google Sketchup, allowing a user to design and input detailed 3D building geometry into the TRNSYS simulation software. The software is provided by TRANSSOLAR (TRANSSOLAR 2015). TRNSYS 3D allows for a versatile link between complex building geometry and the simulation process.

TRNSYS 3D facilitates several useful features such as:

- Create multiple thermal zones and surfaces with custom thermophysical properties from the chosen construction materials.
- Matching adjacent thermal zones and boundary conditions in multizone buildings
- Import Sketchup model into TRNBUILD for automatic input of geometry orientations and area data.
- Create shading zones
- 3D visualisations of TRNSYS simulation results

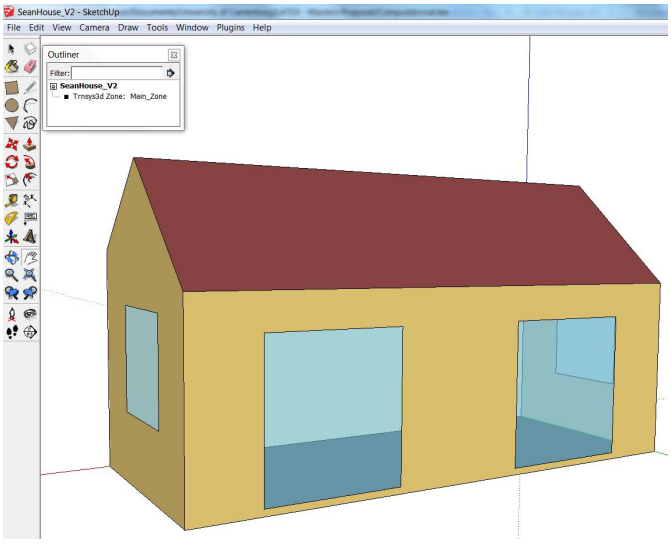

Figure 2.2: A simple single-zone building modelled in Google Sketchup with TRNSYS-3D to define thermal zones and building structure.

2.2.3 TRNBUILD

Three dimensional building data in Sketchup/TRNSYS3D can be imported into TRNBUILD. TRNBUILD allows the user to specify inputs and outputs for the building model to allow the connection of TRNSYS components.

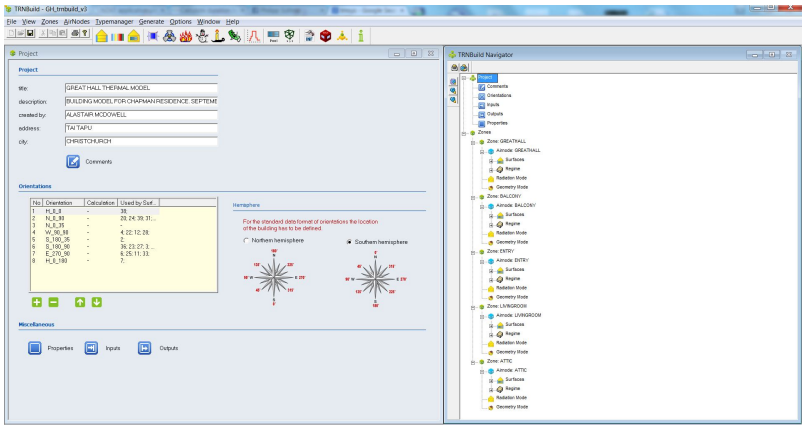

Figure 2.3: TRNBUILD user interface

2.2.4 TRNSYS system as a whole

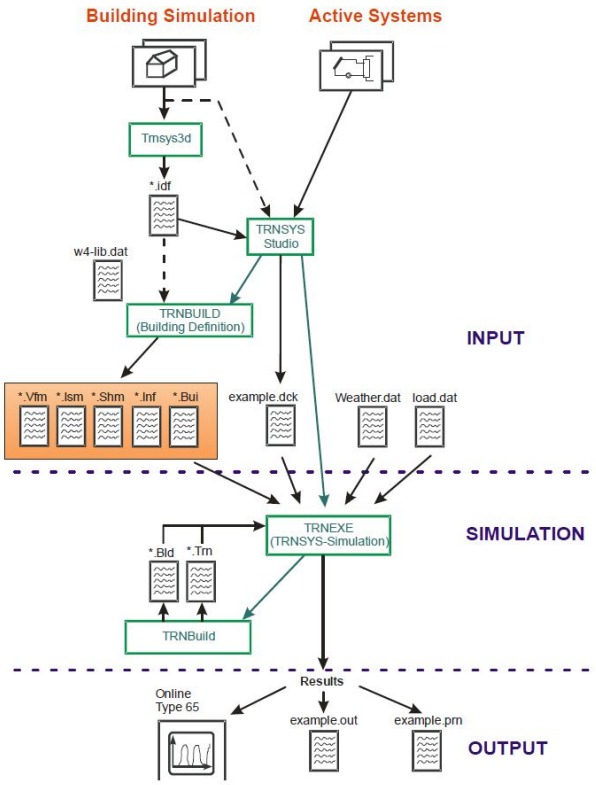

Figure 2.4: How TRNSYS works as a whole system

2.3 Case Study: Chapman Castle

To evaluate the overall benefit that BIPV/T systems can deliver when implemented in a building, it is necessary to model the whole combined system. In open-air loop BIPV/T systems, the collector performance is a function of the inlet fluid conditions. In scenarios where the inlet fluid is air drawn from either inside the building or from outside, it is essential to be able to predict for all time the internal air zone temperatures in order to provide these inputs to the model component. At the output end of the model, the output air is delivered into another zone, or bypassed through an HVAC device which will affect in the internal temperature of that zone.

Meteorological inputs such as solar radiation, ambient temperature, wind speed and direction are applied to the building model as forcing functions.

By integrating the BIPVT model into a complete thermal building model, simulations can provide useful information about the year-round dynamic behaviour of the building and long-term energy performance. This information can be used during the planning stage of a building to improve the design, or post-construction to optimise the general operation of a building.

In this section, complete building models are developed for two case studies using TRNSYS modelling software. Firstly, the existing Chapman Castle is used to provide a benchmark for validation of the TRNSYS approach. The results show how the model can adequately produce realistic predictions for the performance of the BIPVT sytem and temperatures within the Great Hall and adjacent zones. The validation then justifies long-term simulations which provide information on year-round performance, helping to fine-tune the operation of the Castle systems. The second case study is the new transportable building concept developed by Sean Cooney, which is modelled using TRNSYS software to assist in the design process. Year-round simulations give relative thermal performance measures on the use of different building materials and the effect of changing zone geometry.

2.3.1 Early 1D Steady State Model

Early work on this project focussed on studying a simple one dimensional model of the building integrated photovoltaic thermal (BIPV/T) system coupled with underfloor thermal storage in a single-zone house model as a complete system.

Temperatures of the various components in the BIPV/T system were calculated at each time step of the simulation by solving a system of linearised equations defining heat balances across each lumped capacity node. This solution yielded the output air temperature of the BIPV/T ducts, which was ventilated through the underfloor concrete floor to warm the thermal mass of the building. A simple control strategy was used to only circulate BIPV/T air as required when the core temperature fell below the desired temperature, and the BIPV/T air was sufficiently warm to achieve a core temperature rise.

This model was developed in MATLAB with an accompanying guided-user-interface (GUI) allowing users to input custom design parameters for structural properties, building dimensions, area of PV panels, quantity of thermal mass, and select one of several local cities for typical annual weather conditions. Weather and solar input data was sourced from SolarView, a NIWA database. A yearly simulation gave output information that included total

energy savings due to the BIPV/T system and monthly averaged electrical and thermal efficiencies of the BIPV/T system.

Results from this early simple model have proved useful to validate more complex TRNSYS models with ballpark approximations. However, in order to achieve truly realistic results, more detailed mathematical formulations are required to capture the vast complexities of the thermal dynamics present in a real building. Using the TRNSYS software, with a comprehensive library of components and robust model development structure, more time may be spent validating, calibrating the model to capture real data, and extend the models as required to improve accuracy.

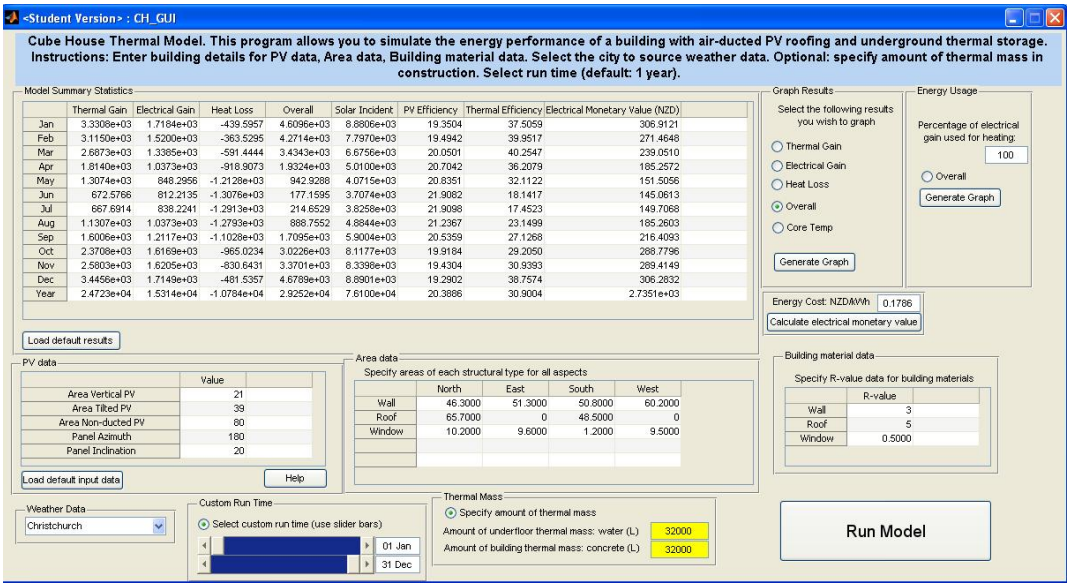

Figure 2.5: Example input and output for a simulation run using the MATLAB GUI for a sustainable building design

2.3.2 TRNSYS model description

The Chapman Castle is used as the first case study to validate the use of the TRNSYS modelling software. The software helps to create a thermal model of the Great Hall and the BIPV/T system.

Key simplifications must be made between the architectural design and the thermal modelling design in TRNSYS. Google Sketchup with TRNSYS-3D is used to model the Chapman Residence. The first modelling consideration is that each thermal zone must be convex rather than concave to allow for

accurate radiation modelling in each zone. The thermal zones in the Chapman castle are divided up accordingly to fulfil this criteria. This approach ensures that all surfaces are in line of sight of all other surfaces. Secondly, all surfaces of alike construction, such as windows and doors, are grouped into equivalent overall surface areas on each orientation. Thus, instead of drawing four small windows on one wall, one window of equivalent surface is area is drawn.

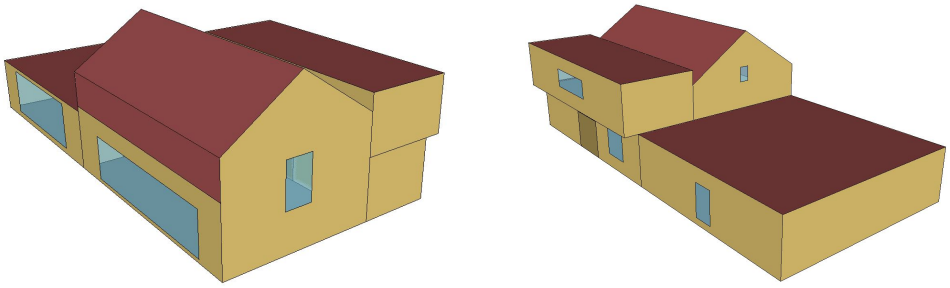

(a) North and east aspects

(b) South and west aspects

Figure 2.6: Chapman Residence modelled in Google Sketchup with TRNSYS-3D

2.3.3 Thermal zones

The Chapman residence was modelled as four thermal zones: Great Hall, Kitchen, Entry and Balcony. The major focus is around modelling the BIPVT system in conjunction with the Great Hall, and thus only the immediate thermal zones surrounding the Great Hall are modelled. Thermal zone adjacencies are carefully modelled. A virtual surface is drawn for the airflow connection between the Great Hall and the Balcony zones. Further details including a visualisation of the system layout are given in Chapter 4. Doors between zones are aligned. Adjacent walls are linked.

2.3.4 Construction materials

Each construction material type used in the Chapman residence is programmed into TRNBUILD as a series of layers of custom building materials. These materials are denoted in TRNSYS as massive, massless, or active layers. Massive layers have significant thermal capacity and a specified conduc-

Window type	U-value	G-value
Double glazed	1.4	0.62
Triple glazed	0.7	0.50

Table 2.1: Window specifications

tivity and density. Massless layers have only a specified thermal resistance (R-value) assigned since their mass is negligible, and is used for insulation materials. Active layers allow modelling of underfloor pipes within a wall or floor group.

Windows

Both double and triple glazed windows are used in the Chapman residence. Custom window types are specified in TRNBUILD. Key window characteristics for various window types are the U-value $[W/m^2.K]$, overall heat loss coefficient, and G-value, the solar heat gain coefficient (SGHC). All windows are made with low-E, low-iron glass and argon filled.

Doors

Doors between the Great Hall and Entry and Kitchen are made with 75mm thick hard-wood with estimated R-value of 2.5.

Walls

The majority of walls are constructed with a 150mm thick concrete slab and 100mm thick R2.8 bib-building insulation blanket. Adjacent walls between zones are made from concrete with no insulation. Interior and exterior wall surfaces are lined with aesthetic stone cladding, and are not included in the model.

Floors

In the Great Hall, two layers of concrete are used: an upper 30MPa concrete floor slab and 400mm deep 15MPa low-shrinkage concrete. Below these two layers is 200mm H-grade polystyrene insulation. Various types of concrete are used in the Great Hall with varying thermal properties:

Strength $[MPa]$	**Thermal capacity** $[kJ/kg.K]$	**Thermal conductivity** $[W/m.K]$	**Density** $[kg/m^3]$
5	1.4	1.5	2275
15	1.5	1.65	2350
30	1.6	1.8	2400

Table 2.2: Concrete physical properties for three types

In the Great Hall, Entry and Kitchen, underfloor heating systems are installed. These are modelled in TRNBUILD using active layers in the floor construction. Pipe work is installed within the concrete layers, above the insulation. Underfloor heating specifications are shown in Table 2.3, including flow per loop. However, during all validation studies there was zero flow through this underfloor system as the heating was not required. Figure 2.7 shows a schematic of the underfloor heating system.

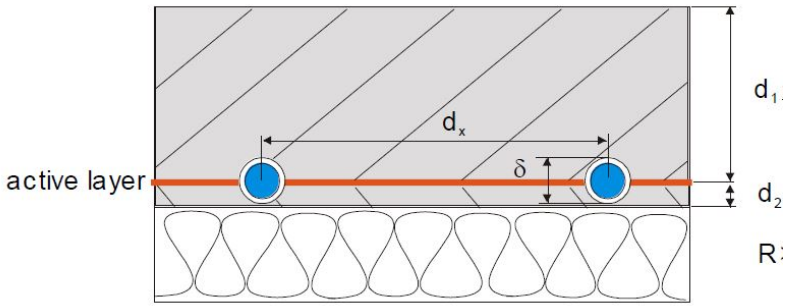

Figure 2.7: Great Hall floor with an active piping system within the concrete layer and R2.8 insulation base.

Zone	**Floor area** $[m^2]$	**Pipe length** $[m]$	**Flow/loop** $[L/min]$	**Heat load density** $[W/m^2]$
Great Hall	77	392	4.5	80
Entry	27	122	2.8	70
Kitchen	109	640	2.5	60

Table 2.3: Under-floor heating specifications

The TRNSYS Type 653 component *Simplified Radiant Floor* represents a simplified heat exchanger effectiveness model with isothermal lumped thermal capacity and is used to represent the underfloor heating system within

the concrete slab. The isothermal assumption is valid if temperature gradients within the slab are low, and the internal thermal resistance is high relative to external heat loss rates (SEL). Firstly, the minimum capacitance of the fluid or slab must be known to estimate the amount of energy transferred between the fluid and the slab. The capacitance is defined as the product of mass and specific heat capacity. The full energy balance on the heated slab is therefore:

$$m_{slab}Cp_{slab}\frac{dT_{slab}}{dt} = -UA_{top}\left(T_{slab} - T_{top}\right) - UA_{bottom}\left(T_{slab} - T_{bottom}\right) + \varepsilon C_{min}\left(T_{fluid,in} - T_{slab}\right) \quad (2.3.1)$$

The convective heat transfer coefficient (CHTC) for the top surface (UA_{top}) is determined through connections to a thin concrete floor slab in the TRNSYS multizone building model. The lower CHTC is set to near zero to ensure direct contact between the TRNBUILD surface and the TRNSYS floor model. This technique allows a high thermal mass component to be modelled in TRNSYS, as TRNBUILD is unable to include high thermal mass components due to strict stability requirements.

Ceilings

Ceilings are designed with extra insulation to account for higher thermal losses through the roof. In the Great Hall, in addition to the R2.8 insulation blanket, R2.2 acoustic tiles are used. Also, on the northern Great Hall ceiling surfaces, the BIPVT system interacts with the Great Hall by coupling the BIPVT component in TRNSYS with the Great Hall thermal zone temperature. In the entry, acoustic tiles are coupled with the concrete slab floor for the balcony. The Kitchen zone ceiling is a concrete slab, with a bedroom above. The bedroom temperature is prescribed for a modelling simplification.

2.3.5 TRNSYS Components

BIPV/T System

A glazed building-integrated PV-thermal model is available in TRNSYS and is calibrated to represent the Great Hall BIPV/T roof. Two orientations

(vertical and tilted) of roofing make up the Great Hall roof and thus two components are linked together. The PV efficiency is calculated using standard correlations for cell temperature and incident radiation, as described in more detail later in this chapter.

Air-Water Heat Pump

An air-to-water heat pump model is used in conjunction with the BIPV/T roof and Balcony thermal zone. The heat pump blower powers the flow rate from the top of the 11 parallel BIPV/T air channels. The outlet air temperature is fed back into the Balcony zone as defined in TRNBUILD as a ventilation input.

2.3.6 TRNBUILD Settings

Infiltration

Infiltration rates of 0.4 air changes per hour are specified for the Great Hall, Living Room and Entry zones. The Balcony zone has no doors open to the outside therefore has a lower infiltration rate of 0.2 from the Great Hall.

Ventilation

The ventilation settings in TRNBUILD are used to connect the flow of warm air from the ouput of the BIPV/T system into the Balcony air zone. The air flow conditions of this ventilation process are defined by the mass flow rate and air temperature measured by the hot-wire anemometer probe.

2.3.7 TRNSYS Simulation model

All of the building information is collated and input into the required TRNSYS component models. The connections for the various components are wired together, linking flows of air, water, and energy throughout the system. A simplified view of the TRNSYS model, excluding extra processing components is shown in Figure 2.8. A special TRNSYS component, Type 56, is used to model the multizone building

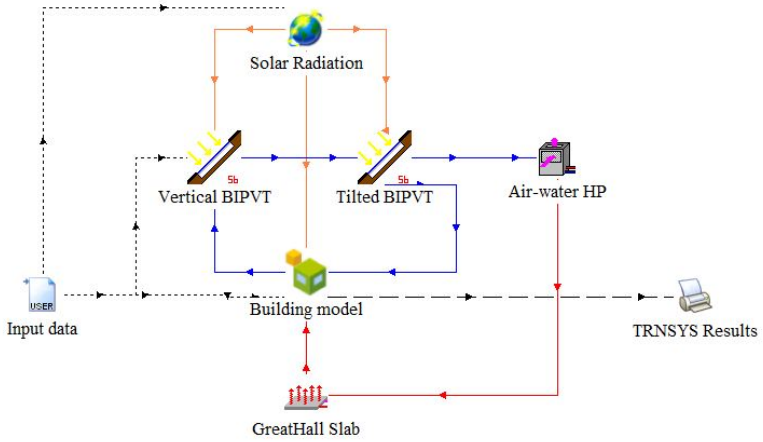

Figure 2.8: Simplified view of TRNSYS model for Chapman Castle.

2.4 Radiation Processing

Solar radiation is one of the major forcing functions of a building's thermal behaviour. The combined effect of the sun's position in the sky and intensity must be accounted for accurately in order to produce realistic models. A single solar quantity is measured: the total horizontal solar irradiance. A significant amount of post-processing of this quantity is required to first decompose the total horizontal irradiance into its beam (direct) and diffuse (scattered) components, and then accounting for the time of day, transformed into total irradiance for each surface orientation required by a particular structure.

An Apogee's CS300 Silicon Pyranometer is used to measure the solar irradiance. The silicon photovoltaic detector mounted in a cosine-corrected head provides an accurate measurement for total horizontal sun plus sky radiation in the spectral range of 300 to $1100nm$. The output is $0.2mV$ per Wm^{-2} allowing for a linear conversion from voltage to irradiance.

The total amount of solar radiation incident on a surface of arbitrary orientation can be calculated from the amount of solar radiation on a horizontal surface. The total horizontal solar radiation G_H must first be de-composed into the beam G_B and diffuse G_D components of radiation, which are treated differently when calculating the amount of radiation on a sloped surface.

The total amount of radiation on a tilted plane of slope angle β and azimuth angle γ is calculated here using a standard isotropic sky radiation model:

$$G_T = G_B R_B + G_D \left(\frac{1+\cos\beta}{2}\right) + G_H \left(\frac{1-\cos\beta}{2}\right) \tag{2.4.1}$$

where R_B is the geometric factor relating to the position of the sun in the sky. To calculate the geometric factor, several other solar angles must first be calculated. The derivation of the geometric factor and other solar angles can be found in Appendix D.

To calculate the amount of incident solar radiation that is absorbed by the PV surface, each of the three spectral components of the incident radiation: beam, diffuse and ground-reflected must be multiplied by the appropriate transmittance-absorptance products ($\tau\alpha$). This product relates to how much radiation is transmitted and absorbed by the PV cover system and PV surface due to the multiple reflections between the layers. The transmittance-absorptance product depends on the solar angle of incidence, thus there exists a different ($\tau\alpha$) for each type of radiation. Using Equation (2.4.1), the absorbed solar radiation S can be calculated:

$$S = G_B R_B (\tau\alpha)_B + G_D (\tau\alpha)_D \left(\frac{1+\cos\beta}{2}\right) + \rho_G G_H (\tau\alpha)_G \left(\frac{1-\cos\beta}{2}\right) \tag{2.4.2}$$

where the subscripts B, D, and G relate to the beam, diffuse and ground-reflected components of incident radiation. ρ_G is the ground reflectance.

An equivalent average ($\tau\alpha$) can be calculated to rewrite S as a product of $(\tau\alpha)_{av}$ and G_T:

$$S = G_T (\tau\alpha)_{av} \tag{2.4.3}$$

Equation (2.4.2) is utilised in Chapter 3 and 4 to derive the thermal efficiency of the BIPV/T collector based on an energy balance over the PV surface.

2.4.1 Beam and diffuse components of horizontal radiation

As the beam and diffuse components of horizontal radiation are treated differently for calculating the incident radiation on a sloped surface, a technique developed by Duffie & Beckman (2013) for estimating the respective fractions of beam and diffuse radiation for a given pyranometer output is followed.

For a large sample of measurements, the diffuse fraction is correlated with the clearness index to provide an estimate of how much radiation is diffuse at any given time depending on the clearness of the skies.

Firstly, a large database of radiation data for a specific location is required. This data is sourced from the TRNSYS weather data file TMY-2, describing a typical year of data for Christchurch. Using hourly radiation data, the diffuse fraction f_d is calculated as the ratio of diffuse radiation to total radiation on the horizontal:

$$f_d = \frac{G_D}{G_H} \tag{2.4.4}$$

Next, an hourly clearness index k_T is defined as the ratio of total horizontal radiation G_H, to the total extra-terrestrial radiation G_0:

$$k_T = \frac{G_H}{G_0} \tag{2.4.5}$$

The extra terrestrial radiation is calculated based on the time and location latitude ϕ according to Spencer (1971):

$$G_0 = G_{sc}\left(1 + 0.033\cos\frac{360d}{365}\right)\cos\theta_Z \tag{2.4.6}$$

where G_{sc} is the solar constant, $1367W/m^2$, d is the day of the year, θ_Z is the solar zenith angle calculated in Equation (D.0.6).

The diffuse fraction is scattered against the clearness index. A piecewise linear function is fitted to the data using a heaviside step-function approach. This function is defined as a function of $x \equiv k_t$:

$$f_{D,corr}(x) = f_1(x)\mathcal{H}_1(x) + f_2(x)\mathcal{H}_2(x) + f_3(x)\mathcal{H}_3(x) \tag{2.4.7}$$

where:

$$f_1(x) = 1 - \frac{1 - F_{d_1}}{K_{T_1}}x, \qquad 0 \leq x \leq K_{T1} \tag{2.4.8}$$

$$f_2(x) = F_{d_1} + \frac{F_{d_2} - F_{d_1}}{K_{T_2} - K_{T_1}}(x - k_{T_1}), \qquad K_{T1} < x \leq K_{T2} \tag{2.4.9}$$

$$f_3(x) = F_{d_2}, \qquad K_{T2} < x \leq 1 \tag{2.4.10}$$

$$\mathcal{H}_1(x) = 1 - \mathcal{H}(x - K_{T_1}) \tag{2.4.11}$$
$$\mathcal{H}_2(x) = \mathcal{H}(x - K_{T_1}) - \mathcal{H}(x - K_{T_2}) \tag{2.4.12}$$
$$\mathcal{H}_3(x) = \mathcal{H}(x - K_{T_2}) \tag{2.4.13}$$

The values of K_{T_1} and K_{T_2} are found iteratively, and the unknowns are F_{d_1} and F_{d_2}. The function of Equation (2.4.7) is fitted to the data by first assuming initial values of K_{T_1} and K_{T_2}, and finding F_{d_2} and F_{d_1} by linear least squares. This process is repeated for a range of values K_{T_1} and K_{T_2} to find the optimum.

To give an idea of the spread of the data, boundary curves enclosing 75% of the data are derived by defining new curves $f_{i,lower} = f_i(x, F_{d_1} + \delta_1, F_{d_2} + \delta_2)$ and $f_{i,upper} = f_i(x, F_{d_1} - \delta_1, F_{d_2} - \delta_2)$ for $i = 1...3$, and iteratively adjusting δ_1, δ_2 in order to enclose 75% of the data.

The resulting fitted correlation is shown in Figure 2.9. The best fit coefficients are: $k_{T_1} = 0.38$, $k_{T_2} = 0.68$, $F_{d_1} = 0.94$, $F_{d_2} = 0.20$, $\delta_1 = 0.07$, $\delta_2 = 0.10$.

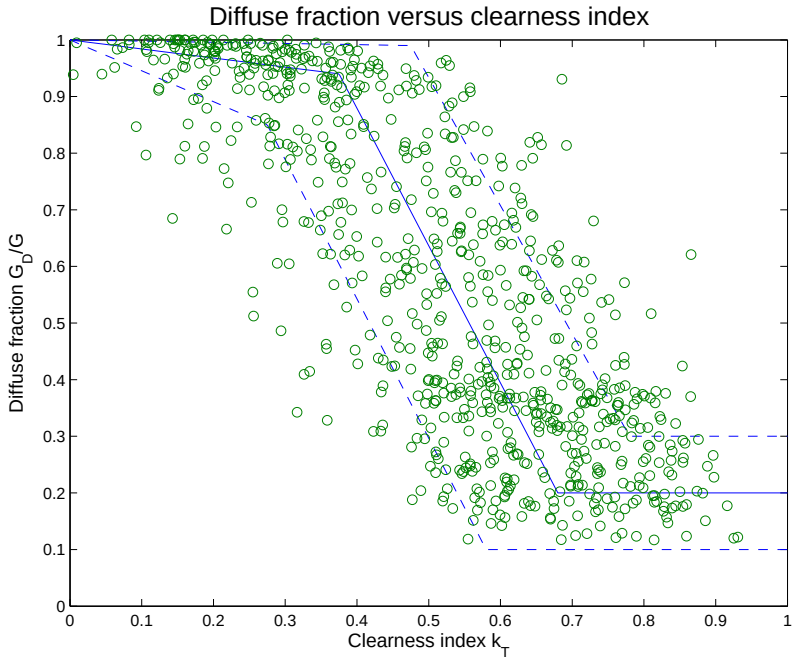

Figure 2.9: A sample of yearly diffuse fraction scattered against the clearness index for a typical year in Christchurch using new correlation (Equation (2.4.7)) and boundary curves enclosing 75% of the data

Using this correlation, the clearness index at any point in time is used to

determine the diffuse fraction, which by re-arranging Equation (2.4.4), the beam (G_B) and diffuse (G_D) components can now be calculated:

$$G_D = f_d G_H \tag{2.4.14}$$

$$G_B = (1 - f_d) G_H \tag{2.4.15}$$

The large amount of scatter about the correlation curve is to be expected and is seen in other literature (Duffie & Beckman 2013). The reason for this spread is that an hourly clearness index value of for example $k_T = 0.5$ could be produced by consistent thin cloud cover, or a combination of an hour of clear skies and half of thick cloud. The first case of thin cloud would give a high diffuse fraction, whereas the second case would give a low diffuse fraction. However, over the long term the correlation adequately represents the mean diffuse fraction. Ogunsola et al. (2014) found that a 10% gaussian uncertainty in solar radiation values has no significant effect on the mean average percentage error (section 2.10) of estimated cooling loads in building thermal simulations. Thus uncertainty in solar radiation prediction is not a significant concern to future simulations.

To verify that this correlation does in fact average out over longer periods to predict accurate quantities of beam and diffuse radiation, total monthly beam radiation calculated using the correlation is compared to the known quantity of beam radiation for the same year of radiation data. As Figure 2.10 shows, over month long periods, the beam radiation predicted using the correlation is very similar to the beam radiation measured directly.

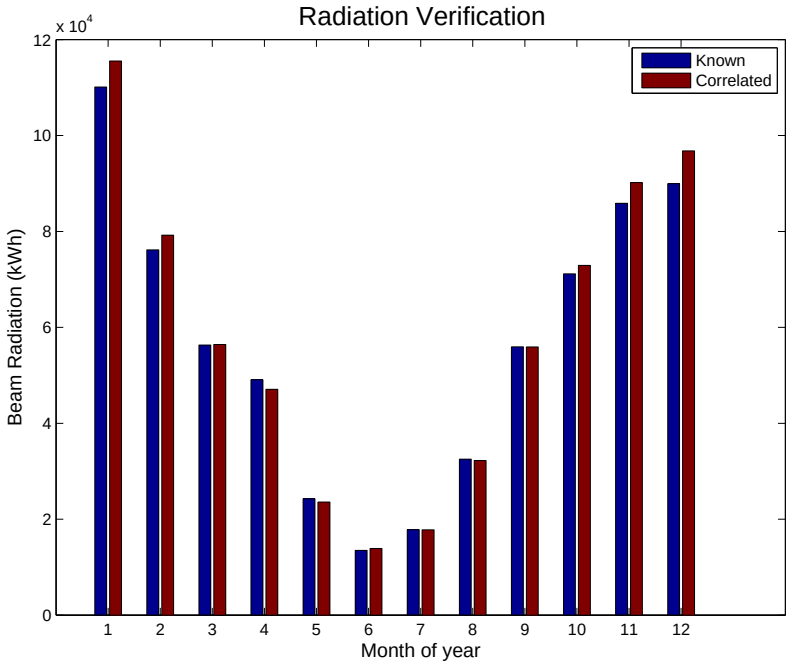

Figure 2.10: Comparison between known beam radiation from the TRNSYS weather data file, and the predicted beam radiation calculated using the correlation based on the same weather data file. Mean absolute percentage error is 2.8%.

2.5 BIPV/T Simulation Model

Early work in this project focussed on developing a simple one-dimensional steady state model in MATLAB for the BIPV/T system to estimate long-term useful energy gain.

The mathematical methodology involved simplifying the BIPV/T thermal system as a lumped capacitance model. It was assumed that for each element in the system - PV cell, PV substrate, backing insulation - the spatial and temporal derivatives of temperature throughout the node were negligible during steady state conditions. This assumption greatly simplified the mathematical analysis.

A series of heat balances across the temperature nodes in the system were derived, and all temperatures in the system were solved by matrix inversion for each hourly time-step in the form:

$$\mathbf{A\ T = b} \tag{2.5.1}$$

where A is a matrix representing all material thermal properties for the related BIPV/T components, T is a vector of temperatures for each lumped capacity element, b is a vector of forcing functions, including solar radiation and ambient conditions.

Another key simplification of this early method was that as the radiative heat transfer coefficients (HTC) are non-linear functions of temperatures, the system was linearised by calculating these HTCs from values of temperature from the previous time step.

This model produced good ball-park figures for the approximate amount of thermal heat gain that the BIPV/T system could produce in various conditions.

The use of TRNSYS software brings the opportunity to make use of an in-built BIPV/T component model developed by Thermal Energy System Specialists (TESS-Inc). This model uses a very similar method to that described by Equation (2.5.1) above. One improvement of the TESS model over the model above is that the radiation HTCs and other non-linear coefficients are calculated using current values by following an iterative method. The TESS model is used for all future simulations of the BIPV/T system and is shown to provide good results.

2.6 BIPV/T Mathematical model

The mathematical model for the BIPV/T system, as implemented in TRNSYS using the Thermal Energy System Simulation Inc. (TESS) component, uses a the lumped capacitance model assumption for simplifying the BIPV/T system down into a series of discrete isothermal nodes.

A series of heat balance equations are written for the five temperature nodes making up the PV module and backing insulation either side of the air duct, and the air stream itself. These five equations are solved to write the useful energy gain as a function of just the air temperature. A final energy balance on a differential section of moving fluid allows a first-order ODE to be written for the air temperature, which is solved to find the output and mean air temperature in the duct.

All temperatures may be written as a function of the mean air temperature. However, the solar radiation and several heat transfer coefficients are functions of the unknown variables, thus this new system of equations must be solved iteratively to within an allowable tolerance range.

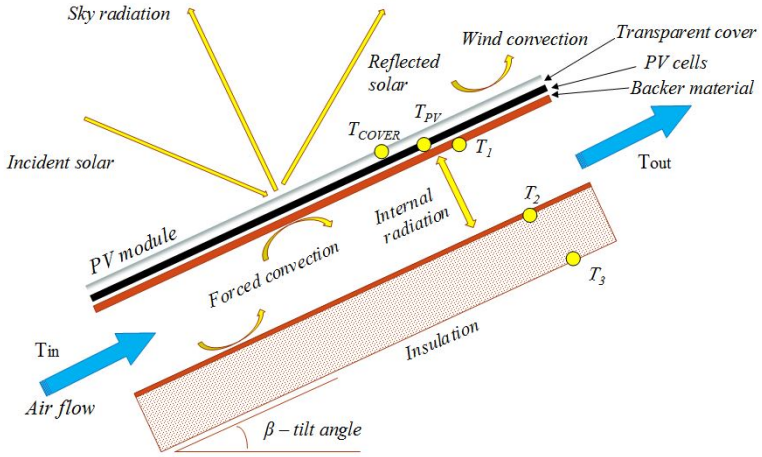

Figure 2.11: Schematic of BIPV/T system heat transfer flows

2.6.1 Cover energy balance

The first energy balance for the cover surface due to conduction from PV cells, and convective and radiative losses to the atmosphere gives the equation:

$$\frac{(T_{PV} - T_{cover})}{R_{cover}} = h_{conv,top}(T_{cover} - T_{amb}) + h_{rad,top}(T_{cover} - T_{sky}) \quad (2.6.1)$$

where:

$$h_{rad,top} = \epsilon_{cover}\sigma(T_{cover} + T_{sky})(T_{cover}^2 + T_{sky}^2) \quad (2.6.2)$$

$$R_{cover} = \frac{L_{cover}}{k_{cover}} \quad (2.6.3)$$

$$h_{conv,top} = f(V_W, \theta_W) \quad (2.6.4)$$

The parameter $h_{rad,top}$ in Equation (2.6.2) is the radiative heat transfer coefficient between the cover and the sky, R_{cover} in Equation (2.6.3) is the resistance of the cover with thickness L_{cover}, conductivity k_{cover}, and $h_{conv,top}$ in Equation (2.6.4) is the exterior convective heat transfer coefficient for the top surface and is calculated as a function of wind speed and direction.

Wind heat loss transfer coefficient

The authors Emmel et al. (2007) found that building energy demands can vary by up to 20-40% depending on the CHTC chosen for certain building surfaces. Their research used a CFD approach to predict the CHTC as a function of wind velocity and direction. This method also takes into account the surface-air temperature differential. The wind speed used is the free-stream wind speed at 10 metres above the ground surface. Wind direction has been defined as positive east of north and negative west of north. Figure 2.12 shows a schematic of the geometry:

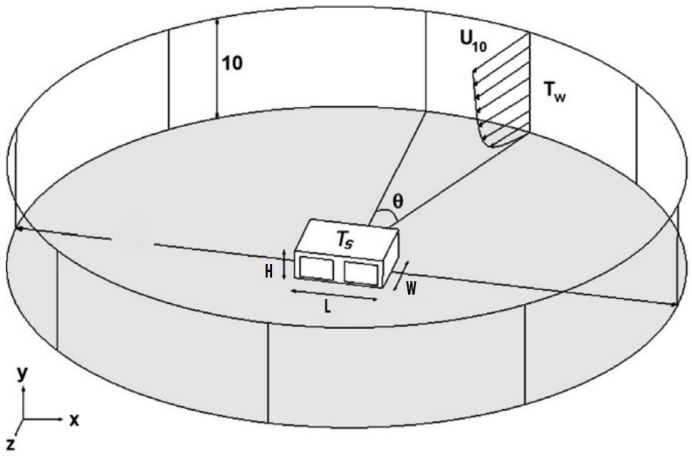

Figure 2.12: Domain geometry for wind external convective heat transfer calculations

The results of the research by Emmel et al. (2007) are summarised in Table 2.4, which shows the expression for the external CHTC for walls and roof surfaces for a range of wind directions.

	Surface-to-wind angle (°)	$h_c(W/m^2K)$
Walls	0	$5.15V^{0.81}$
	± 45	$3.34V^{0.84}$
	± 90	$4.78V^{0.71}$
	± 135	$4.05V^{0.77}$
	± 180	$3.54V^{0.76}$
Roof	± 0	$5.11V^{0.78}$
	± 45	$4.60V^{0.79}$
	± 90	$3.67V^{0.85}$

Table 2.4: External convective heat transfer coefficients as a function of wind speed and direction

Sky temperature

The sky temperature T_{sky} can be calculated using the following correlation between the ambient temperature and the dew point temperature T_{dew} at time t in hours:

$$T_{sky} = T_{amb}(0.711 + 0.0056T_{dew} + 0.000073T_{dew} + 0.013\cos 15t)^{0.25} \quad (2.6.5)$$

2.6.2 PV energy balance

The second energy balance for the PV cells first computes the net absorbed solar radiation S, that is the absorbed solar radiation minus any power production, in terms of conduction to the cover and upper air channel surfaces:

$$S = \frac{(T_{PV} - T_{cover})}{R_{cover}} + \frac{T_{PV} - T_1}{R_1} \quad (2.6.6)$$

where R_1 is the PV substrate resistance.

The absorbed radiation S can also be written in an equivalent form by adapting Equation (2.4.3) to account for various incidence angles:

$$S = (\tau\alpha)_n \,\mathrm{IAM}\, G_T(1 - \eta_{PV}(T_{PV}, G_T)) \quad (2.6.7)$$

where $(\tau\alpha)_n$ is the transmittance-absorptance product at normal incidence, IAM is the incidence angle modifier for other incidence angles, and η_{PV} is the PV efficiency, which is a function of the PV cell temperature and the total incident radiation.

2.6.3 Air duct energy balance

The third energy balance describes the energy flows between the upper air channel surface, the PV cells and air stream, and radiation between the upper and lower duct surfaces:

$$\frac{(T_{PV} - T_1)}{R_1} = h_{air}(T_1 - T_{air}) + h_{rad,1-2}(T_1 - T_2) \tag{2.6.8}$$

The radiative heat transfer coefficient between the upper and lower channel surfaces, $h_{rad,1-2}$, is defined:

$$h_{rad,1-2} = \frac{\sigma(T_1^2 + T_2^2)(T_1 + T_2)}{\frac{1}{\epsilon_1} + \frac{1}{\epsilon_2} - 1} \tag{2.6.9}$$

where $\sigma = 5.67 * 10^{-8}$ is the Stefan Boltzman constant and e_1, e_2 are the upper and lower channel surface emissivities.

2.6.4 Air stream energy balance

The fourth equation is for the air flow control volume, with flows from the upper and lower duct surfaces:

$$q"_u = h_{air}(T_1 - T_{air}) - h_{air}(T_{air} - T_2) \tag{2.6.10}$$

where $h_{air} = \frac{Nuk_{air}}{D_h}$ is the fluid convection coefficient, Nu is the Nusselt number, k_{air} is the conductivity of air, and D_h is the hydraulic diameter of the duct.

2.6.5 Lower duct energy balance

The fifth energy balance describes the lower duct surface, heat transfers from the air stream via convection, radiation from the upper channel surface, and conduction to the back surface temperature, defined as the Great Hall ceiling temperature in TRNSYS studio:

$$h_{air}(T_{air} - T_2) + h_{rad,1-2}(T_1 - T_2) = \frac{(T_2 - T_3)}{R_2} \tag{2.6.11}$$

where R_2 is the thermal resistance of the lower insulation layer.

2.6.6 Overall solution

The five energy balances of Equations (2.6.1)-(2.6.11) can be solved to form an equation for the useful energy gain $q"_u$, across a differential section of the duct dx, as a function of the air temperature T_{air} in the form:

$$q"_u = aT_{air} + b \tag{2.6.12}$$

where a and b are a collection of the model parameters, defined in Appendix E.

The final energy balance that closes the system, links the variables $q"_u$ and T_{air} by taking an energy balance across a differential section of the duct in the cross-sectional direction (into the page):

$$\dot{m}C_p\frac{dT_{air}}{dx} - Wq"_u = 0 \tag{2.6.13}$$

Figure 2.13 shows the differential energy balance described by Equation (2.6.13):

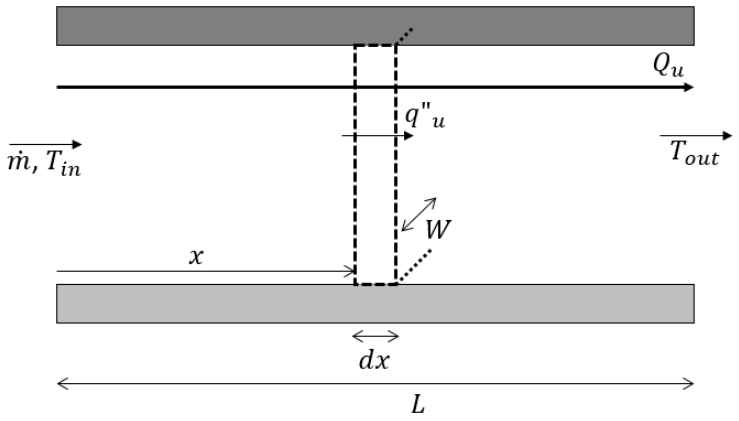

Figure 2.13: Schematic of differential energy balance over the air stream control volume

Combining Equations (2.6.12) and (2.6.13) yields:

$$\frac{dT_{air}}{dx} = \left(\frac{W}{\dot{m}C_p}\right)aT_{air} + \left(\frac{W}{\dot{m}C_p}\right)b \tag{2.6.14}$$

where W is the channel width.

Integrating Equation (2.6.14) gives an expression for the air temperature as a function of distance along the channel:

$$T_{air}(x) = \left(T_{air,in} + \frac{b}{a}\right) \exp\left(\frac{W}{\dot{m}C_p} ax\right) - \frac{b}{a} \tag{2.6.15}$$

Solving for the end of the channel, where $x = L$, the outlet fluid temperature can be found:

$$T_{air,out} = \left(T_{air,in} + \frac{b}{a}\right) \exp\left(\frac{Aa}{\dot{m}C_p}\right) - \frac{b}{a} \tag{2.6.16}$$

where $A = WL$ is the duct cross sectional area.

The total useful energy gain in the BIPV/T system, which is a sum of all the differential energy gains $q"_u$ is defined:

$$Q_u = \dot{m}C_p(T_{air,out} - T_{air,in}) \tag{2.6.17}$$

Substituting Equation (2.6.16) into (2.6.17) yields the final formula:

$$Q_u = \dot{m}C_P \left(\left(T_{air,in} + \frac{b}{a}\right) \exp\left(\frac{Aa}{\dot{m}C_p}\right) - \frac{b}{a} - T_{air,in}\right) \tag{2.6.18}$$

Equation (2.6.18) is coded up in FORTRAN and carried out in the TRNSYS simulation models which are used for computationally modelling the BIPV/T system thermal performance.

2.7 BIPV/T Energy Balance

For all studies into optimising the performance of the BIPV/T system, the overall energy balance of thermal gains, electrical gains, and fan energy consumption must be considered. The overall energy balance is:

$$Q_{gain} = Q_{thermal} + Q_{electrical} - Q_{fan} \tag{2.7.1}$$

2.7.1 Thermal gain

Useful thermal energy gain depends on the mass flow rate of air through the ducts, $\dot{m}$, specific heat capacity of the air C_P, and the temperature rise between the inlet and outlet, T_{in}, T_{out}.

$$Q_{thermal} = \dot{m} C_P (T_{out} - T_{in}) \tag{2.7.2}$$

2.7.2 Electrical gain

Electrical gain depends on the operating voltage and current for the PV modules, which are controlled to operate at the maximum power point. This energy is calculated in practice by applying linear efficiency correlations for the cell temperature dependence, β_{ref}, a standard PV specification. The PV cell has an electrical efficiency η_{ref} at the cell temperature $T_{cell} = T_{ref}$.

$$Q_{electrical} = V_{mpp} I_{mpp} = G\{\eta_{ref} \left[1 + \alpha_P (T_{cell} - T_{ref})\right]\} \tag{2.7.3}$$

2.7.3 Pressure losses

The amount of fan work required to move an air stream through an air duct at a required flow rate is dependant on the total pressure losses across the duct. Losses in dynamic pressure are due to friction at the duct walls, bends, obstructions or changes in duct cross section.

The friction factor is a function of the Reynold's number of the flow (a function of the air velocity V) and the relative roughness of the duct $\varepsilon = k/D_h$, where k is the absolute roughness of the duct which is taken to be $0.3 * 10^{-3}$. The 1983 Haaland simplification of the Colebrook equation for a turbulent flow is:

$$\frac{1}{f^{1/2}} \approx -2 \log_{10} \left[\left(\frac{\varepsilon}{3.7} \right)^{1.11} + \frac{6.9}{Re} \right] \tag{2.7.4}$$

with length L and hydraulic diameter $D_h = 2Wh/(W+h)$, where W is duct width and h is channel height.

The total pressure drop across a duct is proportional to the dynamic pressure, by a factor of the frictional loss and all other loss coefficients due to duct geometry, K_L. Loss coefficients account for a sharp opening ($K_L = 0.5$), intake

air mesh ($K_L = 2$), 45° bend at exit ($K_L = 0.4$), with sudden expansion to attic size of height H ($K_L = (1 - h^2/H^2)^2$).

$$\Delta P = \left(f \frac{L}{D_h} + \Sigma K_L \right) \rho \frac{V^2}{2} \tag{2.7.5}$$

The fan work required to overcome the frictional losses is proportional to the overall pressure loss and the volume flow rate. The overall fan-motor efficiency is based on the manufacturer's specifications.

$$Q_{fan} = \frac{\dot{V} \Delta P}{\eta_{fan} \eta_{motor}} \tag{2.7.6}$$

where $\dot{V}$ is the volume flow rate, η_{fan}, η_{motor} is the fan and motor efficiencies respectively.

2.8 Computational Fluid Dynamics Analysis

Computational Fluid Dynamics (CFD) is a commonly used numerical technique to analyse complex systems involving fluid flow and heat transfer. A CFD analysis of the Chapman BIPV/T system will provide useful information about the flow patterns to be expected inside the BIPV/T ducts. The hypothesis to be tested is whether the overall HTC between the heated PV panels and air stream is increased compared to the theoretical value due to the elbow bend in the duct at the transition from the vertical to tilted slope. This unique flow characteristic can only be calculated using a finite volume method to solving the fundamental equations that determine the flow patterns.

Candanedo et al. (2010) used computational fluid dynamics (CFD) models to derive the convective heat transfer coefficients in an asymmetrically heated channel. The results of this paper determined a HTC of $5.8 W/m^2.K$ for a vertical PVT duct, dimensions $0.1m$ deep, $1m$ high, $1m$ wide, with a air velocity of $0.5m/s$, and an inlet geometry similar to the design studied in this thesis. This result is validated experimentally, and is used as the reference value for the PV surface heat transfer coefficient.

2.8.1 CFD Model Development

The CFD software used is ANSYS CFX 15. The analysis process involves five steps. The fluid flow geometry is defined in an in-built CAD software *Design Modeller*. This geometry is passed into a meshing tool, where a specific mesh is designed to capture the dynamics of the problem. Commonly, structured inflation layers are used on the walls to capture the high gradients there. Unstructured hexahedron or tetrahedron mesh is used to represent the internal flow domain. The boundary conditions for the geometry are then assigned and an appropriate turbulence model is chosen. The simulation is performed until the range of the variables thermal energy, momentum, turbulence, achieve convergence to the specified tolerance level.

2.8.2 Governing equations

At the fundamental level, the equations of continuity, momemtum and energy are solved in the CFD code in order to find a viable solution. The equations solved are as follows. The continuity equation:

$$\frac{\partial}{\partial x}(\rho u) + \frac{\partial}{\partial y}(\rho v) = 0 \tag{2.8.1}$$

Conservation of momentum in the x-direction:

$$\frac{\partial}{\partial x}(\rho u u) + \frac{\partial}{\partial y}(\rho u v) = -\frac{\partial P}{\partial x} + \frac{\partial}{\partial x}\left(\mu \frac{\partial u}{\partial x}\right) + \frac{\partial}{\partial y}\left(\mu \frac{\partial u}{\partial y}\right) \tag{2.8.2}$$

Conservation of momentum in the y-direction:

$$\frac{\partial}{\partial x}(\rho u v) + \frac{\partial}{\partial y}(\rho v v) = -\frac{\partial P}{\partial y} - \rho g \beta (T - T_{ref}) + \frac{\partial}{\partial x}\left(\mu \frac{\partial v}{\partial x}\right) + \frac{\partial}{\partial y}\left(\mu \frac{\partial v}{\partial y}\right) \tag{2.8.3}$$

Conservation of energy:

$$\frac{\partial}{\partial x}(\rho u T) + \frac{\partial}{\partial y}(\rho v T) = \frac{\partial}{\partial x}\left(\frac{K}{c_P}\frac{\partial T}{\partial x}\right) + \frac{\partial}{\partial y}\left(\frac{K}{c_P}\frac{\partial T}{\partial y}\right) \tag{2.8.4}$$

During the CFD simulation, an iterative solution process is conducted until the residuals between two solutions reaches a specified tolerance for all included equation models. At this point the solution has reached convergence.

2.8.3 Geometry

The duct system is drafted using the ANSYS in-built CAD package DesignModeler. Since the flow through the duct can be assumed symmetrical across the $1.0m$ wide duct, a differential extrusion depth of $0.01m$ can be used to reduce computational expense and run-time of the simulation. Realistic dimensions for the rest of the duct are: a channel height of $0.2m$, vertical section length $1.16m$, tilted section length $6.09m$. The opening vent is $0.2m$ high in the vertical direction on the northern (left) side of the duct.

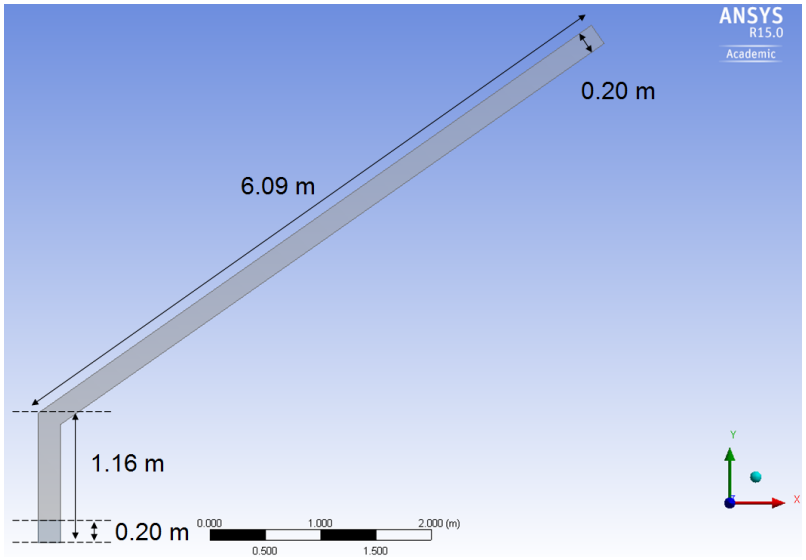

Figure 2.14: Geometry of the BIPV/T system as modeled in ANSYS

2.8.4 Mesh

The most important aspect of the meshing process for duct flow is to adequately capture the boundary layer effects. To achieve these effects, inflation layers are applied onto the fluid-wall interfaces to capture the rapidly changing gradients at these surfaces. Several layers of mesh at gradually increasing thickness's are applied for a total thickness equal to the thickness of the boundary layer.

The boundary layer thickness δ is defined:

$$\delta = \frac{0.382x}{Re_x^{1/5}} \tag{2.8.5}$$

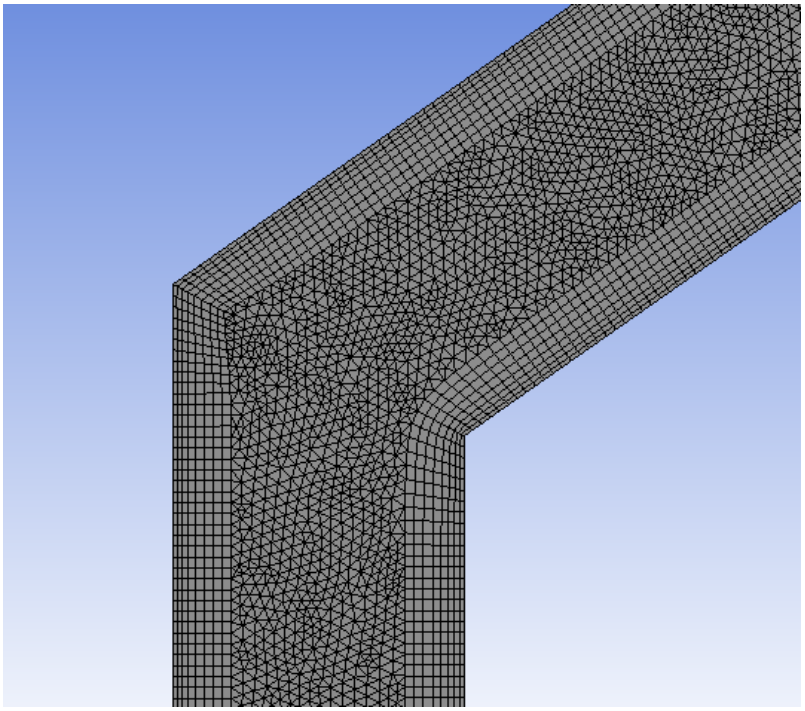

Figure 2.15: Representative mesh design for CFD analysis

where Re_x is the Reynolds number using characteristic length x. For this mesh, the boundary layer thickness is $4.7cm$.

The remaining mesh throughout the centre of the duct is filled with unstructured tetrahedral mesh elements. The total number of meshing nodes used is $100,000$ for a coarse mesh and up to a maximum of $500,000$ nodes for the fine mesh.

2.8.5 Boundary Conditions

Appropriate boundary conditions must be assigned for all surfaces in the CFD-Setup application. Importantly, the inlet-outlet boundary condition pairing are chosen to ensure stability.

- Inlet: opening, relative pressure $P = 0Pa$.
- Outlet: prescribed velocity components $V = 0.5m/s$
- North walls: prescribed temperature $T = T_{PV}(x)$; non-slip wall $U = 0$, $V = 0$.

- South walls: adiabatic; non-slip wall $U = 0$, $V = 0$.
- East and west walls: symmetry, adiabatic.

2.8.6 Turbulence Model

The RNG $k - \epsilon$ model is an improvement over the standard $k - \epsilon$ model as it is less dissipative in recirculating and separated flows. The flow in this section of ducting is expected to involve flow separation and recirculating flows at the inlet opening. The RNG $k - \epsilon$ is a two-equation model for the turbulent kinetic energy k and the turbulent dissipation ϵ. The model uses a mathematical approach which attempts to account for the different scales of motion through changes to the production term (Yakhot et al. 1992). The main equations for the RNG $k - \epsilon$ turbulence model are:

$$\frac{\partial}{\partial t}(\rho k) + \frac{\partial}{\partial x_i}(\rho k u_i) = \frac{\partial}{\partial x_j}\left(\left(\mu + \frac{\mu_t}{\sigma_{tk}}\right)\left[\frac{\partial k}{\partial x_j}\right]\right) + P_k - \rho\epsilon \tag{2.8.6}$$

$$\frac{\partial}{\partial t}(\rho\epsilon) + \frac{\partial}{\partial x_i}(\rho\epsilon u_i) = C_{1\epsilon}\frac{\epsilon}{k}P_k + C^*_{2\epsilon}\rho\frac{\epsilon^2}{k} + \frac{\partial}{\partial x_j}\left(\left(\mu + \frac{\mu_t}{\sigma_\epsilon}\right)\left[\frac{\partial \epsilon}{\partial x_j}\right]\right) \tag{2.8.7}$$

where u_i is a velocity component, $\mu_t = \rho C_\rho \frac{k^2}{\epsilon}$ is eddy viscosity, P_k is the production of kinetic energy, $C^*_{2\epsilon} = C_{2\epsilon} + \frac{C_\mu \eta^3 \left(1 - \frac{\eta}{\eta_0}\right)}{1+\beta\eta^3}$ and $\eta = (2S_{ij}S_{ij})^{\frac{1}{2}}\frac{k}{\epsilon}$, and C_μ, σ_{tk}, σ_ϵ, $C_{1\epsilon}$, $C_{2\epsilon}$, β, η_0 are adjustable constants used to tune the model, set to the defaults prescribed by ANSYS.

2.8.7 Solution Parameters

The absolute convergence criteria for residuals are $1e - 6$, which is shown to be adequate tolerance for convergence to a steady-state. The maximum number of iterations is 100.

2.8.8 Results

The first step in analysing the results of the CFD simulation is to *verify* and *validate* the solution.

Verification ensures that the equations are being solved correctly. Verification involves checking that the mesh is suitable and converges to an exact solution as the grid size is refined.

Validation involves comparing the output air temperatures against experimental values under similar conditions.

Mesh refinement

To verify that the continuum partial differential equations are being solved correctly by the mesh, a grid refinement study is performed. The mesh is coarsened and refined to produce three meshes - coarse, medium and fine which are significantly different from each other.

$$h = \left[\frac{V}{N}\right]^{\frac{1}{3}} \quad r = \frac{x_{coarse}}{x_{fine}} > 1.3$$

where h is the average mesh length, V is the domain volume, N is the number of nodes in the mesh, r is the refinement ratio.

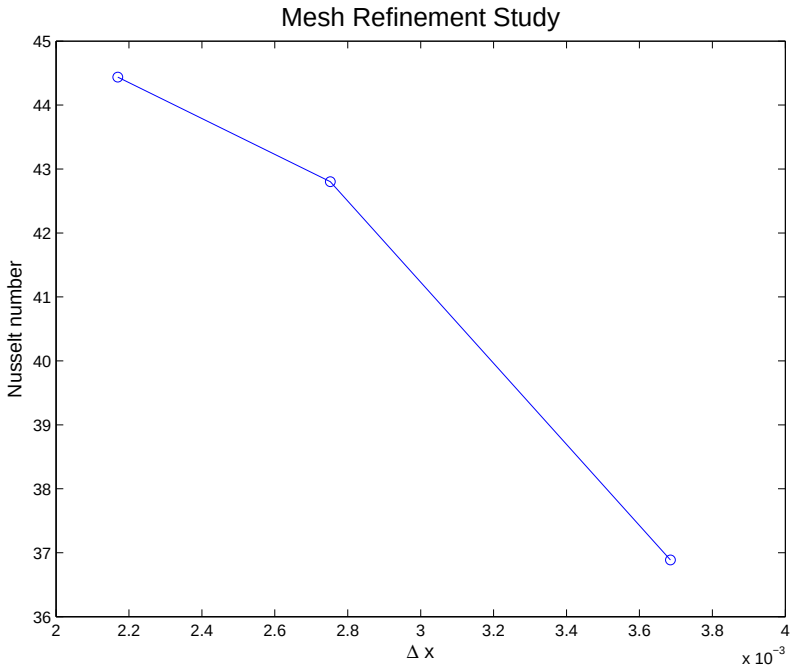

Figure 2.16: Mesh refinement showing the convergence of the Nusselt number as the grid size reduces

Richardson extrapolation

Richardson extrapolation is used to calculate the value for any variable of interest for an infinitely fine mesh, given the mesh is in the region of monotonic convergence where higher order terms become negligible. In our case, the extrapolated HTC based on coefficients calculated at a fine (1) and coarse mesh (2) is defined:

$$h_{extrap} = \frac{x_2^2 h_1 - x_1^2 h_2}{x_2^2 - x_1^2} \tag{2.8.8}$$

The extrapolated average HTC for the vertical PV surface is $5.17 W/m^2K$ and for the tilted surface is $4.49 W/m^2K$. These values are of the same order as those found by Candanedo et al. (2010) who calculated a HTC of $5.8 W/m^2K$ in a similar CFD study. Candanedo's slightly higher value can be explained by the more narrow channel used in his case study of $0.1m$.

2.9 Coupling TRNSYS with MATLAB for automated simulations

When the simulation engine in TRNSYS is coupled with the post-processing functions available in MATLAB, a powerful tool is created Jones (2010). By setting up the TRNSYS simulation to read input variables from text files and output results to text files, MATLAB can be used as a pre-processing and post-processing tool. All information defined in a TRNSYS studio simulation relating connection of components, parameter values and simulation settings are all written to a TRNSYS *deck* input file. MATLAB can be used to edit this input file by replacing certain parameter values with a range of new values over a series of automatic simulations.

This procedure enables the user to investigate the effect on simulation results following the change of a specific parameter over a set range. For example, the yearly electrical energy gain from a PV array mounted on a building can be plotted against the tilt angle of the PV modules to identify the optimal value of the tilt angle.

The MATLAB code used to perform these functions is shown in Appendix B.

2.10 Error estimation

The mean absolute percentage error (MAPE) is the measure used to calculate the error between simulated and measured data, or between data and an estimated trend (Ogunsola et al. 2014).

$$MAPE = \frac{100\%}{n} \sum_{i=1}^{n} \left| \frac{Q_{act} - Q_{pred}}{Q_{act}} \right| \tag{2.10.1}$$

where n is the total number of data points, Q_{act} is the actual/measured data value, Q_{pred} is the predicted/simulated data value.

2.11 Conclusion

In this section the modelling methodologies used in this thesis have been presented, which uses TRNSYS as a modelling and simulation tool. The development of the TRNSYS model for the Castle is outlined, describing how the details of the building are modelled using the TRNSYS software suite.

The method for processing raw radiation data is given, showing the decomposition process into the beam and diffuse components. This decomposition is necessary for calculating the amount of radiation incident on the variety of surface inclinations and orientations that occur on buildings and BIPV/T systems.

The mathematical details and solution process for the BIPV/T model are shown. The overall energy balance including electrical, thermal and fan work is described, which defines the objective function for optimisation of the BIPV/T system.

The basis for a numerical model of the Chapman Castle's unique BIPV/T geometry is described.

A method of coupling MATLAB with TRNSYS for automation of parametric runs is given and used extensively in the later optimisation sections.

Chapter 3

Experimental BIPVT Study

3.1 Introduction

Experimental analysis is a useful tool to help understand the heat and fluid transfer dynamics of a system operating under a range of controlled conditions. The aim of this section is to study the BIPV/T system experimentally using a testing apparatus designed to replicate the thermal and electrical behaviour of a BIPV/T system integrated with the thermal mass of a building. An experimental BIPV/T rig is constructed and fitted with various measurement devices to record thermal performance. A range of tests are undertaken to understand the limits of performance for a typical installation under standard outdoor operating conditions.

3.2 Experimental BIPV/T System

A small-scale replica of the Chapman Hall BIPVT system has been constructed for the purpose of experimental testing. The experimental rig will allow qualitative testing over a range of parameters that affect BIPVT thermal performance, thus increasing understanding of how to operate the large-scale system for optimal thermal and electrical gains. Figure 3.1 shows a diagram of the planned design for the experimental testing rig.

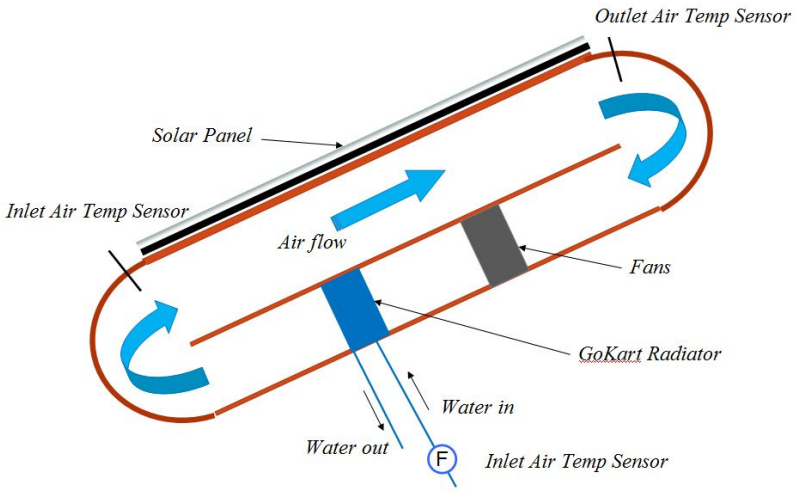

Figure 3.1: Solar rig schematic

3.2.1 Construction method

One photovoltaic panel with area $1.65m^2$ is mounted on a double layered wooden frame. The top channel allows air to circulate beneath the underside of the PV panel thus cooling the panel and heating the air. The air is driven in the lower channel by four square axial SUNON $138CFM$ fans, and cooled by a water fed radiator. Input water flow from a standard garden hose is controlled by a pump unit to a constant flow rate.

Performance of a general solar collector is determined by calculating the thermal efficiency over several hours of operation in steady weather conditions and full sun. Various operational parameters may also be varied to evaluate their effect on the system's thermal efficiency.

Temperature of input and output water is measured with thermo-couple probes inserted into the PVC tubing. Water flow rate is measured with a high-precision water flow sensor, accurate for flows $0.3 - 6.0L/min$. The standard flow rate used for experiments is $2.5L/min$.

Air temperature and flow rate is inherently very difficult to measure directly, as the temperature and flow velocity profiles vary greatly across the cross sectional area. An important design consideration is that the system is closed, with all air leakages and thermal losses minimised using expanding foam sealant and R5 insulation. Therefore, by measuring the input and output water temperatures and flow rates, the amount of thermal gain can

be accurately measured during steady-state operation.

Due to the width of the radiator, the lower channel is tapered in the centre to vent the air through a slightly narrower channel, as shown in Figure 3.2.

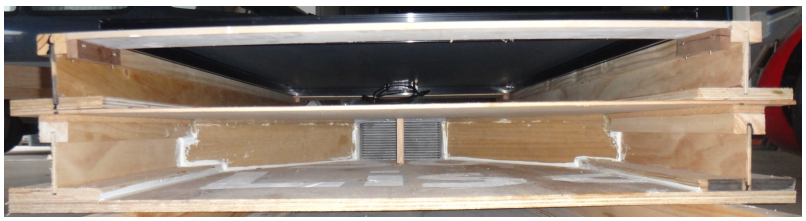

Figure 3.2: Experimental rig in construction process. Shown are the two layers with tapered air venting towards radiator on bottom layer (fans not shown), ducted PV panel in top layer

In the lower channel, air first passes through the radiator, cooling the also straightening the flow, ensuring a smooth laminar flow for entry to the fans.

Four fans will be mounted in parallel in order to increase the air flow rate. However, according to Jones (2014), twice the fans never mean twice the air flow. If fans are placed too close together, other interference effects come into play and reduce the overall flow. Flow is only doubled in an ideal situation with low system resistance. Thus, the four fans are equally spaced over the full width of the duct.

3.2.2 PV modules

The PV unit used is a 240W polycrystalline A-grade solar panel. Specifications are shown in table 3.1. Various sizes between 95W and 240W are used across the entire northern wall and roof space of the Chapman Castle due to space constraints. However, the 240W model is the most common panel specification for the BIPV/T system.

3.2.3 Instrumentation

A range of instrumentation are used to collect a full set of data necessary to calculate thermal efficiency of the collector.

Meteorological inputs include ambient air temperature, global solar irradiance, wind speed and direction. System variables include the input and

Specification	Symbol	Value	Unit
Max-power	P_{mp}	240	W
Max-power voltage	V_{mp}	30.0	V
Max-power current	I_{mp}	8.01	A
Open-circuit voltage	V_{oc}	36.8	V
Short-circuit current	I_{sc}	8.6	A
Cell efficiency	η_{cell}	16.8	%
Module efficiency	η_{module}	14.9	%
Power temp. coeff.	α_P	-0.4336	$\%/°C$
Nominal operating cell temp.	NOCT	45	$°C$
PV aperture area	A_{PV}	1.65	m^2
Tilt angle	β	20	°
Azimuth angle	γ	180	°
Channel depth	d	0.1	m
Channel length	L	1.6	m
Maximum air flow rate	V_a	0.19	m^3/s
Maximum water flow rate	$\dot{V}_w$	2.5	L/min

Table 3.1: BIPV/T specifications

output air temperatures for the BIPV/T system, input and output water temperatures through the radiator unit, water and air flow rates.

All sensors are connected to a data logger written in Delphi on a monitoring laptop to record results at discrete time steps.

The range of instrumentation devices required were purchased from online retailers to a strict set of specifications.

Air flow rate: Hot wire thermal anemometer. The standard ASTM D3464 - 96(2007) is followed in order to measure the average velocity in a duct using a thermal anemometer. For long term data collection, the anemometer is inserted perpendicularly into the flow channel at a position 10cm from the top of the duct in the centre. Hotwire anemometers use the cooling effect of air passing over a heated element. They monitor the power required to maintain the temperature of the element, and this is proportional to the air flow (TechRentals NZ 2015). See Figure A.3.

Solar irradiance: Solar pyranometer. The Apogee CS300 pyranometer features a silicon-cell photodiode with excellent cosine response and measures total solar radiation to within 5%. The device is mounted at the Chapman

Castle. See Figure A.4.

Water flow rate: A 6mm plug small hall water flow sensor is used to measure the water flow rate through the radiator unit. The sensor is calibrated to be accurate for low flow rates of $0.3 - 3.0L/min$. The typical flow rate used in tests is $2.5L/min$. The water flow speed is moderated by a electronic pump unit See Figure A.2.

Water temperature: long temperature probes are inserted into the inlet and outlet water hoses that are connected to the either end of the GoKart radiator which accurately measure water temperature.

3.3 Completed Testing Rig

Figure 3.3 shows the physical layout of the completed aparatus.

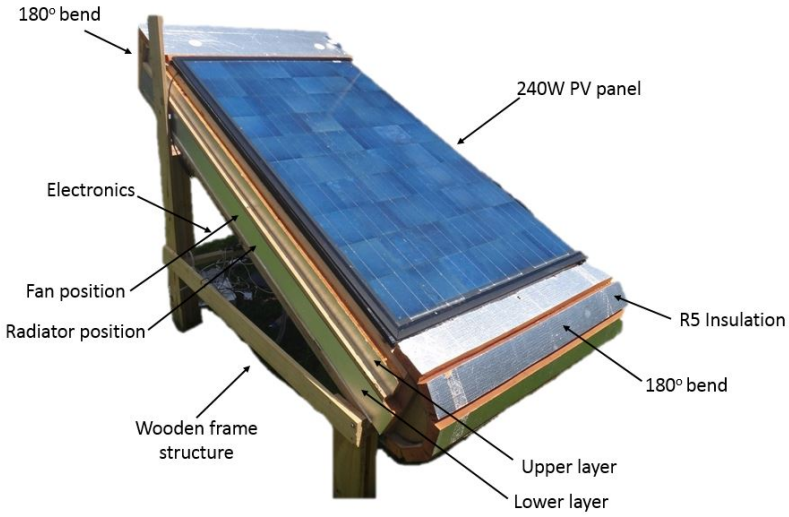

Figure 3.3: Solar rig physical lay out

Figure 3.4: Experimental solar rig during a testing session

Figure 3.4 shows the experimental rig during an initial testing session at the Chapman Castle.

3.4 BIPV/T Performance Characterisation

This section describes the testing procedure for a BIPV/T system and how the test data is presented in a meaningful way. Specifically, the solar collector operating data is used to show how efficient the system is at converting incident solar radiant energy into useful thermal energy.

Characterising the performance of the BIPV/T system with a simplified model is useful for predicting thermal performance of the collector for long-term simulation, and performance comparison against other thermal collectors. More complex models are available which include details of construction materials, as described in section 2.6, but for this experimental study, a simple two-parameter model is adequate. The two parameters in this model relate to how the collector absorbs heat, and how it loses heat (Duffie & Beckman 2013).

3.4.1 Thermal performance equations

The useful thermal energy gain Q_u is defined:

$$Q_u = \dot{m} C_P (T_{in} - T_{out}) \tag{3.4.1}$$

Q_u is calculated from the air flow rate $\dot{m}$, the inlet air temperature T_{in} and outlet air temperature T_{out}. These parameters are measured using the instrumentation as shown in Figure 3.1. The specific heat capacity of air is known to be $C_P = 1.005 kJ/kg.K$ at 20°C.

However, although Q_u is useful for comparing the qualitative impact of parameters like flow rate on the thermal energy, for short tests Q_u can vary wildly during a day due to variations in the incident solar energy. It is also not suitable for comparisons between different sized PV panels.

Hence, an instantaneous thermal efficiency is defined as the ratio of useful thermal energy Q_u to the incident solar energy on a tilted surface G_T:

$$\eta = \frac{Q_u}{A_{PV} G_T} \tag{3.4.2}$$

where G_T is derived in Equation (2.4.1) and A_{PV} is the PV surface area.

Equation (3.4.2) allows a comparison between any size of PV panels and to solar radiation intensities over time, with known measurements of the air flow rate and inlet/outlet air temperatures.

To analyse the thermal performance of the BIPV/T system for any given conditions without requiring measured data, a one-dimensional steady state model for the collector is developed.

Useful thermal energy gain can also be calculated by considering an energy balance for the PV surface. In steady state conditions, the energy balance is arranged to show that the thermal output is the difference between absorbed solar gain and overall thermal loss using the Hottel-Whillier-Bliss method (Duffie & Beckman 2013):

$$Q_u = A_{PV}[S - U_L(T_{PV} - T_{amb})] \tag{3.4.3}$$

where S is the absorbed solar radiation defined in Equation (2.4.2), U_L is the overall heat loss coefficient, T_{PV} is the PV cell temperature and T_{amb} is the ambient temperature.

Since the PV cell temperature is inherently difficult to measure, Equation (3.4.3) is reformulated in terms of the inlet air temperature, by introducing a new parameter called the heat removal factor F_R (Duffie & Beckman 2013). This factor takes into account the air flow rate and specific heat of air, and is defined:

$$F_R = \frac{\dot{m}C_P}{A_{PV}U_L}\left[1 - e^{-\frac{A_{PV}U_L F'}{\dot{m}C_P}}\right] \tag{3.4.4}$$

where F' is defined:

$$F' = \left[1 + \frac{U_L}{h_{fluid} + \left(\frac{1}{h_{fluid}} + \frac{1}{h_{rad}}\right)^{-1}}\right]^{-1} \tag{3.4.5}$$

Absorbed solar radiation S is also replaced by the $G_T(\tau\alpha)_{av}$ as defined in Equation (2.4.3).

The new form of the thermal energy gain equation is:

$$Q_u = A_{PV}F_R[G_T(\tau\alpha)_{av} - U_L(T_{in} - T_{amb})] \tag{3.4.6}$$

Combining Equations (3.4.2) and (3.4.6) gives a model for the thermal efficiency of the system in terms of the inlet air temperature T_{in}, incident solar radiation G_T, and ambient temperature T_{amb}:

$$\eta = F_R(\tau\alpha)_{av} - F_R U_L\left(\frac{T_{in} - T_{amb}}{G_T}\right) \tag{3.4.7}$$

Thus, the definition of instantaneous thermal efficiency forms the basis for the two parameter model in $F_R(\tau\alpha)_{av}$ (solar absorptance) and $F_R U_L$ (thermal loss).

The use for Equation (3.4.7) is that the BIPV/T thermal efficiency and thus thermal gain can now be calculated purely as a function of the inlet air temperature, ambient air temperature and incident solar radiation. This approach greatly simplifies the calculation of instantaneous thermal gain of the system for any given operating point.

3.4.2 General test method

ASHRAE 93-2003 defines the standard method for the testing of thermal collectors and outlines how experimental data is presented in a useful way. Experimental data is collected for the BIPV/T system during a clear day where the clearness index is low and thus there is a high proportion of beam radiation. Tests are to be performed when the angle of incidence of beam radiation is approximately normal to the plane of the collector. Measurement devices record solar radiation and ambient temperature, as well as inlet, outlet air temperatures in the duct and air flow rate through the duct.

The experimental data will contain some variation about this two-parameter linear characterisation due to angular and temperature dependencies on the variables. The parameter U_L is a function of temperature and wind speed, F_R is a weak function of temperature, and the relative proportions of beam and diffuse radiation during the test may vary (Duffie & Beckman 2013). Thus, the scattered data must be fitted by least-squares regression with the intercept and slope coefficients of this fit representing the two parameters of the model.

The data is plotted as thermal efficiency η, against $(T_{in} - T_{amb})/G_T$. The resulting linear correlation will have an intercept of $F_R(\tau\alpha)_{av}$ and slope of $F_R U_L$, as derived from Equation (3.4.7).

3.5 Results

Several tests are performed on the solar rig apparatus to determine its thermal performance. Firstly, a basic thermal performance test to analyse the relative thermal and electrical efficiencies during a standard day of operation. The thermal efficiency is characterised using the standard procedure. Secondly, the effect of varying air flow rates is investigated to determine whether an optimal air flow rate exists.

3.5.1 Validation

A validation study is performed by comparing the thermal efficiency calculated from air and from water measurements. The air flow rate and air temperature rise across the PV panel are measured to calculate useful thermal energy Q_u from Equation (3.4.1). The water flow rate across the radiator,

and temperature difference of the water between the inlet and outlet is also measured to calculate Q_u, assuming a specific heat capacity of water to be $C_P = 4.184kJ/kg.K$. Figure 3.5 shows that the thermal efficiencies calculated from air and water match closely. During this test, the air flow rate is decreased in steps, which results in slight drops in thermal gain and therefore a decrease in efficiency. As a result, the difference in time constant can be seen between the two mediums due to the higher specific heat capacity of water compared to air. The thermal efficiency measured by air drops off rapidly, and the thermal efficiency measured by water takes longer to reach the steady state efficiency. The close correlation between these two independent measurements gives confidence to the accuracy of the data produced by the experimental apparatus.

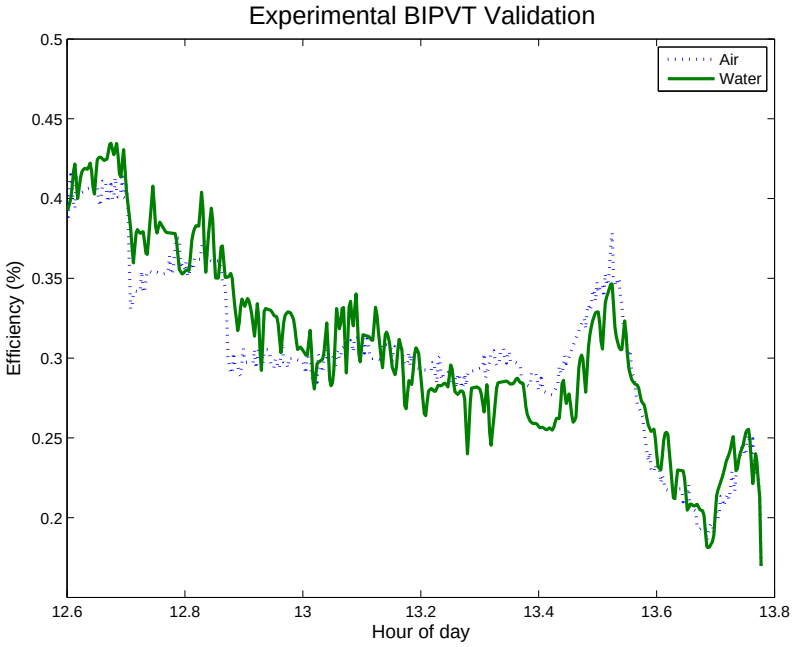

Figure 3.5: Validation by comparison of thermal efficiency measured by air and water temperatures and flow rates.

3.5.2 Basic thermal performance test

The solar rig was operated at steady flow conditions during a clear sunny day, between 9.30am and 3:00pm. Air and water flow rates were kept constant at their maximum respective rates as quoted in Table 3.1. The PV tilt angle used was 20° and the collector faces true north. Throughout the test the

ambient temperature is slowly increasing from 12°C to a maximum of 17°C. The solar radiation shown in Figure 3.7 is the irradiance on the tilted plane of the PV surface, which reaches a maximum of $500W/m^2$ during the test.

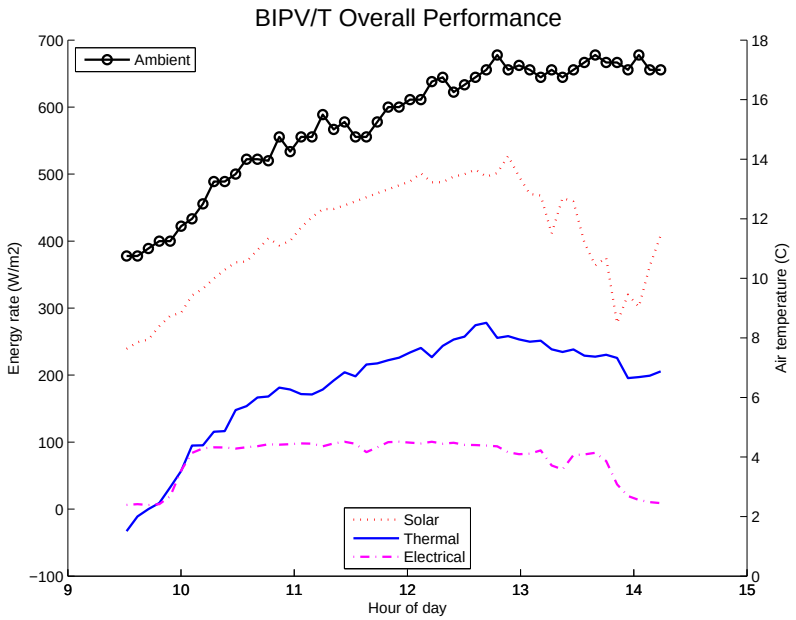

Figure 3.6: Overall thermal performance

Figure 3.7 shows the quantity of useful thermal and electrical energy per unit area of collector. Once the PV panel begins to receive solar radiation, the electrical efficiency ramps up and is maintained at approximately 20% until the panel goes into the shade. The thermal efficiency averages at 32%.

3.5.3 Thermal Efficiency Characterisation

The thermal performance of this BIPVT system is now characterised for winter performance by plotting the thermal efficiency against $(T_{in} - T_{amb})/G_T$. Each data point is averaged over 1 minute, with a data recording interval of 10 seconds.

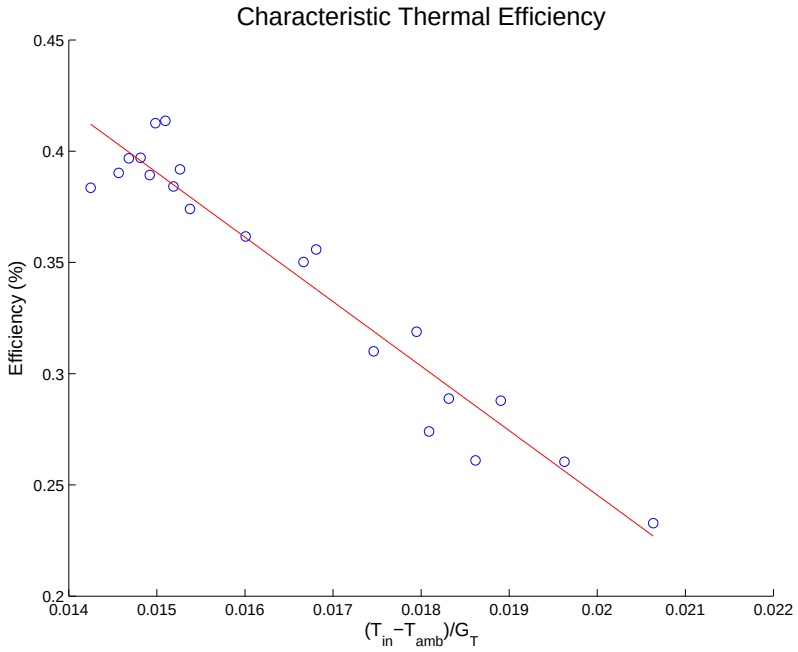

Figure 3.7: Characteristic thermal performance curve

Figure 3.7 shows the thermal efficiency η for the BIPV/T system for a range in $\Delta T/G$.

Qualitatively, it can be seen that the collector is more efficient at either lower inlet air temperatures above the ambient, or for higher solar radiation levels.

A least-squares fit for the data produces an R^2 correlation coefficient of 0.93. A linear least-squares fit relationship is found from the data to determine the two parameters of the model. The $F_R U_L = -slope = 28.98 W/m^2 C$ and $F_R(\tau\alpha)_{av} = 0.83$. This function is only valid for values of $\Delta T/G$ between $0.014 - 0.021 m^2.K/W$, the typical range of winter operating conditions. Further tests during summer conditions are required to verify this relationship for a larger range of values for $\Delta T/G$. This test data can be used to compare the performance of this particular BIPV/T system with other similar units.

3.5.4 Air Flow Test

The hypothesis to be tested in this section is that with progressively faster air flow rates through the BIPVT channel, the amount of thermal energy collected will increase but with diminishing gains, and past some flow rate the

extra work required to operate the fans will lead to lower overall efficiencies. Thus, the aim is to find out whether an optimal flow rate exists within the range of fan speeds available for this particular system. This optimal flow rate could then be recommended for other systems as to provide the maximum overall efficiency.

As described in more detail in section 2.7, the overall efficiency is the ratio of overall energy gains, a combination of the thermal, electrical and fan work, to the incident solar radiation:

$$\eta_{overall} = \frac{Q_{thermal} + Q_{electrical} - Q_{fan}}{A_{PV} G_T} \tag{3.5.1}$$

Test method

The air flow rate can be controlled using the specially designed Delphi GUI. The fan voltage is varied between $24 - 48V$, which results in a range of air flow speeds between $1 - 1.7m/s$, measured using a Kestrel air flow meter. The air flow rate is set to $48V$ and progressively decreased in steps of $8V$ after a time period of 10 minutes. Ambient air temperature and solar radiation were reasonably steady during this test.

Results and discussion

Figure 3.8a shows the averaged thermal, electrical and fan energy rates for a range of four air flow speeds. It can be seen that the electrical efficiency increases by 1.2% across the range of flow speeds, with slight diminishing returns. The rate of useful thermal energy clearly shows this increasing trend with diminishing returns, with an increase of 10% thermal efficiency between the range of flow speeds.

As expected, as the flow speed increases, the fan work increases by the cube of the flow speed. Combining this effect with the plateauing rate of increase in the thermal energy gain, the overall gains show a decreasing trend beyond a certain flow rate. This behaviour is shown more clearly in Figure 3.8(b) where the overall efficiency is plotted against air flow speed. It can be seen that for this particular system, the optimal flow rate is in the vicinity of $1.5m/s$. Therefore the optimum flow rate per unit collector area is $0.11kg/sm^2$. This result is similar to the value of $0.12kg/sm^2$ found by Tiwari et al. (2006),

but much greater than the findings of Hegazy (1999) who quotes $0.02 - 0.03 kg/sm^2$.

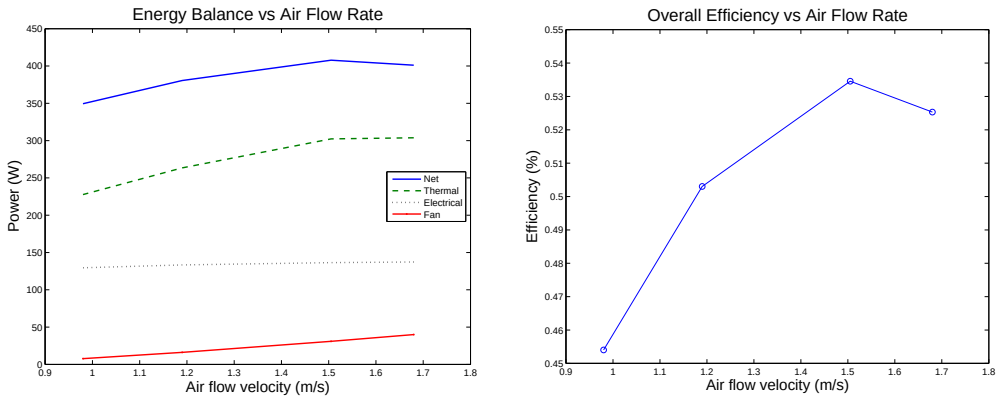

(a) Energy balance for experimental BIPV/T system for a range of air flow rates

(b) Overall efficiency of experimental BIPV/T system for a range of air flow rates.

Figure 3.8: Air flow rate experimental results

Figure 3.8 shows that significant gains are to be made by selecting the optimal air flow rate, and beyond this flow rate, these gains will reduce due to diminishing returns on useful thermal energy.

This experimental BIPV/T system proves that a significant increase in the overall efficiency of a solar PV panel can be made by introducing ducted air flow and harnessing this heat generation within a building.

Figure 3.8(b) takes the results from Figure 3.8(a) and applies Equation (3.5.1) to calculate the overall efficiency of the system, which is the ratio of thermal, electrical and fan energy to incident solar radiation.

Figure 3.8(b) shows that this system is capable of attaining an overall efficiency of 53% at the optimum air flow rate of $1.5 m/s$. This result lines up with other research; one study tested a single-PV panel BIPV/T system and determined an overall efficiency of 50% was possible (Solanki et al. 2009).

This result explains the motivation to combine both thermal and electrical generation with the BIPV/T system, which may be used for a variety of applications in a building context. Due to the low electrical efficiency of solar panels, much of the incident radiation is lost as heat. However, using BIPV/T technology, this wasted heat can be harnessed through a collecting air stream and stored in the thermal mass of a building.

3.6 Conclusions

An experimental testing unit replicating a BIPV/T system has been designed, constructed, tested and analysed. Results have illustrated the relative amounts of energy and efficiencies that can be expected for a BIPV/T system for a range of operating conditions. The overall efficiency has been optimised for the most important control variable, air flow rate.

Overall, the quantity of thermal energy collected by this simple PVT collector shows that the concept is viable, and when integrated into a building, has the potential to meet a good proportion of thermal heat requirements in a building by significantly boosting the overall efficiency of the PV array. Current solar panel technology is not sufficiently advanced to capture a great enough proportion of the incident solar radiation, which is typically less than 20%. A large fraction is also lost through reflection and wasted as heat.

This experimental work shows that using BIPV/T technology, the system is capable of converting up to 53% of solar incident radiation into a combination of electrical and thermal energy, with only a small quantity of electrical energy required to power the fans to circulate air.

This experimental testing rig has the potential to explore the effect on thermal and electrical performance of many other design parameters. These include tilt angle, azimuth angle, channel depth, effect of shading, solar incidence angle modifiers, and enhancement features such as internal fins.

Chapter 4

Building and BIPVT Thermal Modelling

4.1 Overview

The Chapman Castle is a unique renewable energies building used as the major case study for this research. This building features a building-integrated photovoltaic/thermal (BIPV/T) system linked with the Great Hall and thermal storage systems. In this chapter, the TRNSYS thermal model of the Chapman Castle, as described in Section 2.3 of Chapter 2, is validated against real measured data. Individual components of the overall system - building and BIPV/T system - are first validated separately, followed by a full system validation. Long-term simulations are then performed to estimate the monthly distribution of thermal and electrical gains.

4.2 Model Validation

Validation of the model is a vital process in ensuring that the TRNSYS model is accurate for a wide range of real conditions. With a basic working model representing the Chapman Castle, the results are compared with real data to assess the validity of the results.

4.2.1 Data collection

A range of measurement equipment is set up at the Castle to record all the necessary data that is fed back into the model as inputs. Two main sets of real data are collected over a one-week period: (1) meteorological data - solar radiation, ambient temperatures, wind speed and wind direction, (2) building related data - room temperatures and relative humidity for each zone.

Meteorological input signals are connected to the power-line carrier network for the Castle, allowing this data to be appended to existing data logging systems in the Castle. Building zone air temperature and humidity units are located at various points in the rooms, and data is downloaded manually from in-built data-logging systems. Details for the measurement units used are shown in appendix A.

4.2.2 NIWA data comparison

To verify that the solar radiation values recorded at the Chapman Residence are accurate, they are compared with data sourced from the NIWA CliFLO database, measured at Christchurch airport. Figure 4.1 shows that the measured values align very closely with the NIWA data. Thus, the solar pyranometer used is suitable for the experimental and monitoring tests.

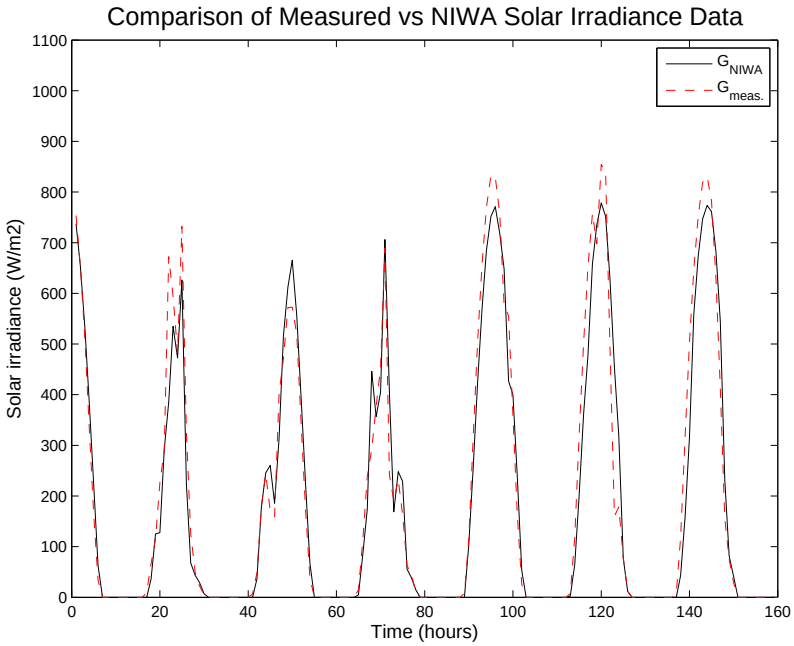

Figure 4.1: Verification of solar radiation data measured at Chapman residence compared with NIWA data for Christchurch

4.2.3 Wind heat loss modelling

External convective heat transfer coefficients (CHTC) for buildings are a function of two variables: wind speed and wind direction. See section 2.6.1 for the derivation for the wind heat loss transfer coefficients.

For TRNSYS simulation, wind speed and directional data are used from NIWA's CliFLO weather database for Christchurch. A TRNSYS input file for h_c was written calculating the appropriate value for each data point.

4.2.4 Initial Building Validation Results

At the completion of a period of monitoring, a complete set of experimental data is compiled and fed into the TRNSYS simulation as inputs. The output air zone temperatures for the Great Hall and Balcony are compared against real measurements for the same time period. Residual plots show the discrepancy between the measured and predicted data. The acceptable error range is $0.5K$ and is denoted by dashed lines on the residual plots.

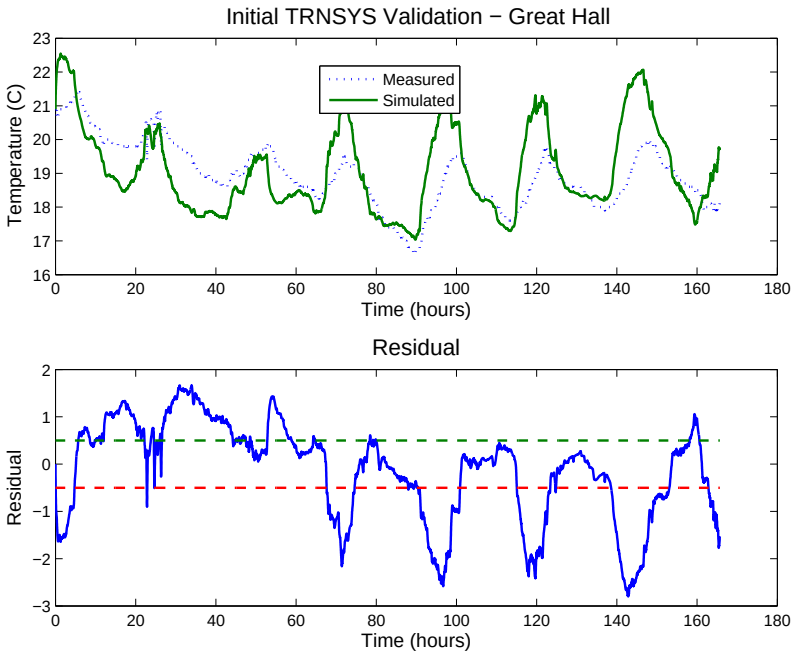

Figure 4.2: Residual plot for initial validation

The prediction error for this validation study has a mean of $-0.13K$, and standard deviation of 1.03. Therefore 95% of the data is within $-2.19K$ and $1.93K$ of the true measured value. However, the required tolerance for a good validation is for the error to be within a $0.5°C$ tolerance. Therefore a sensitivity analysis is performed to determine which model parameters are contributing most significantly to this error.

4.3 Sensitivity Analysis

Sensitivity analysis (SA) is an important stage in the thermal modelling procedure for building energy simulations. SA identifies which variables must be known accurately in the model, as inaccuracy in their measurement could lead to large errors in the simulation predictions.

Discrepancy in simulation results can be derived from three main sources (Mara et al. 2001):

TRNSYS - Incorrect model assumptions, inappropriate model components

Experimental measurements - Sensor position, instrumentation fault

Parameter values - Under or over estimation of parameter values

Sensitivity analysis will check that parameter values are correct, and if necessary may lead to an investigation to improve experimental measurements.

4.3.1 Methodology

The SA method involves perturbing each of the most influential inputs about their base-line values, to determine which produce the most variance in simulation results. A simple method to perturb each variable is used, where each time-dependant vector is perturbed by a small amplitude, typically 1%, of the base case vector to ensure the system behaves linearly. Some construction material parameters are also very sensitive to the change of one of their physical parameters, thus only small changes must be made to maintain uniformity across all parameters. The perturbed value $X^*(t)$ is defined:

$$X^*(t) = \left(1 + \frac{a}{100}\right) X_0(t) \tag{4.3.1}$$

where a is the amplitude of the perturbation and X_0 is the base value.

The most important variables to investigate with this analysis have been identified as:

- Window area (A_w)
- Conqueror panel parameters: conductivity, capacity, density (k_c, C_c, ρ_c)
- Concrete slab parameters: capacity, density (C_{cs}, ρ_{cs})
- Insulation thermal resistance (R_I)
- Infiltration rate (INF)
- Radiation inputs: diffuse, direct (G_D, G_D)
- Ambient: air temperature, relative humidity (T_{AMB}, $RHUM$)
- Wind: speed, direction (W_S, W_D)

4.3.2 Sensitivity Analysis Results

The effect of each perturbed variable is determined by calculating an overall influence coefficient (IC) for each variable. Lomas & Eppel (1992) describe

several SA techniques used for building thermal simulation programs, including differential SA, monte-carlo analysis, and stochastic SA. Differential sensitivity analysis is shown to be the best method.

The IC coefficient shows the relative magnitude of change that this variable has on the new simulation result relative to other parameters. The influence coefficient is defined as:

$$IC = \frac{\text{change in output}}{\text{change in input}} = \frac{\Delta OP}{\Delta IP} \tag{4.3.2}$$

where ΔOP is the change in simulation output that occurs with each change in the input, ΔIP (Fabriek 2013).

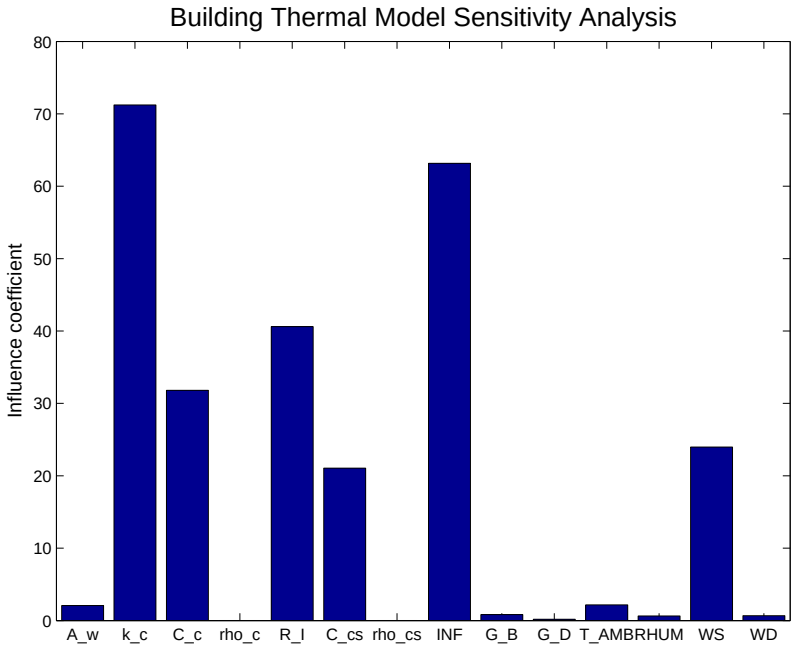

Figure 4.3: Sensitivity analysis results for building model

Figure 4.3 shows the influence of the selected variables on the simulation output for the air zone temperature in the Great Hall. The base parameters chosen are the parameters from the initial validation study of Figure 4.2.

The most influential parameters on the air zone temperature are the material properties of the concrete used in the structure, the insulation resistance, and the infiltration rate. This result shows that the building's thermal mass plays an important role in determining the building's temperature. The values for

the material properties of the various types of concrete are taken from the manufacturer's detailed specifications, so are assumed accurate.

Wind speed is also an important parameter. Previously, wind speed was measured using hourly data sourced from NIWA weather stations. However, Figure 4.3 shows that it is important to take more frequent measurements directly from the Castle to take into account local wind effects. The wind speed and direction sensor mounted on the roof of the castle are specified in Appendix A.

The influence of the infiltration rate in Figure 4.3 is particularly strong, and the estimation of this parameter is also one of the most uncertain among those studied. Intuitively, the infiltration rate is variable with time, based on the pressure difference between the building and outside. Therefore, for a more accurate model, it is important to measure the infiltration rate for this building over a range of conditions.

4.4 Building air infiltration

Air infiltration is the rate at which air from outside is unintentionally exchanged with the inside air; a measure of the building's leakiness. Energy loss due to infiltration, is one of the major loads of a building's space heating bill, alongside conductive losses. The air infiltration rate is defined as the volume flow rate of air moving between a building zone and the outside, per unit volume of the room. Thus the units for infiltration are $m^3/h/m^3 = 1/h$, or number of air exchanges per hour (ACH/h).

During a sample of building infiltration rates in standard residential houses in Dunedin, the average air change rate was found to be 0.82 ACH/h, with the majority of rates between 0.6 and 1.0 ACH/h. Modern energy-efficient buildings are usually well-sealed and experience lower infiltration rates. However, for extremely well-sealed buildings, it is vital that ventilation systems maintain a healthy CO_2 level in the building.

Air infiltration rates are a function of the air pressure and air density differences across the building's envelope. These local atmospheric factors are driven by wind speed and direction. Obtaining an accurate formula for the time dependant nature of the infiltration rate in each building zones has been shown to greatly reduce the error in building energy simulations (Han et al. 2015). Malik (1978) found clear evidence during extensive field studies that

wind speed and direction, and inside-outside temperature difference had a impact on the building air exchange rate.

Thus, the goal of this section is to derive a formula for the infiltration rate as a function of wind speed, which is measured directly at the Chapman residence. This measurement is important due to the local wind effects present at the particularly exposed location on the top of knoll. Over the course of several infiltration rate tests in a range of atmospheric conditions, a relationship is determined.

4.4.1 Infiltration rate measurement method

The most common measurement technique for evaluating the air infiltration rate in buildings is a form of tracer-gas decay method. A single building zone is brought to a uniform concentration in a tracer gas, and the gas is measured over time as it decays. Assuming a constant infiltration rate of I, the tracer concentration is defined:

$$\Delta C(t) = \Delta C_0 e^{-It} \tag{4.4.1}$$

where $\Delta C(t) = C_{absolute}(t) - C_{ambient}$, and ΔC_0 is the initial difference, t is time in hours since start of the test.

4.4.2 Experimental set-up

Experiments were conducted at the Chapman Residence to identify the infiltration rate for the Great Hall zone. Extra openings such as the chimney, floor vents, and BIPV/T flaps were all closed, and door edges to other building zones were sealed. Thus, the only air leaking from the zone would be between the Great Hall and the ambient air.

A BOC carbon dioxide (CO_2) cannister fitted with a regulator was used to dispense a uniform concentration of CO_2 throughout the entire zone. Large rotating fans in the room ensured the room air was well mixed throughout the test.

Three CO_2 data logger units were placed at various heights and locations throughout the room, at floor, head height and roof level. These data loggers were set up to record CO_2 concentration levels (ppm) every 5 seconds. Once the CO_2 reached a steady concentration of 1500 ppm throughout the room,

the room was evacuated for three hours until CO_2 levels returned close to the original concentration level.

4.4.3 Results

The tests were undertaken with various atmospheric conditions between $2 - 40km/h$ wind speed from the north, and ambient temperatures of between $25 - 28°C$. The downloaded CO_2 logger data is processed in MATLAB. To determine the exponential coefficient, a linear relationship is fitted to the log of the concentration values using the $polyfit$ function in MATLAB. Thus, the infiltration rate is the negative of the slope of the linear fit.

$$\log \Delta C(t) = \log \Delta C_0 - It \tag{4.4.2}$$

The CO_2 concentration data is analysed and the entire experimental process exhibits several distinct stages. The ambient CO_2 concentration level is disturbed upon the injection of the tracer gas into the zone. Once injection concludes, the concentration peaks there is an initial transient period that occurs before the gas is fully mixed, as shown in Figure 4.4(a). Later, the decay rate begins to follow the form of exponential decay. This later section of data is selected for fitting to an exponential relationship.

The resulting fitted curve, shown in Figure 4.4(b) shows a close match to the scattered data. This process is repeated for each CO_2 sensor located in different areas in the Great Hall. The average infiltration rate between the three sensor data sets is calculated to be 0.41 ACH/h. The average wind speed during this test is approximately $9km/h$.

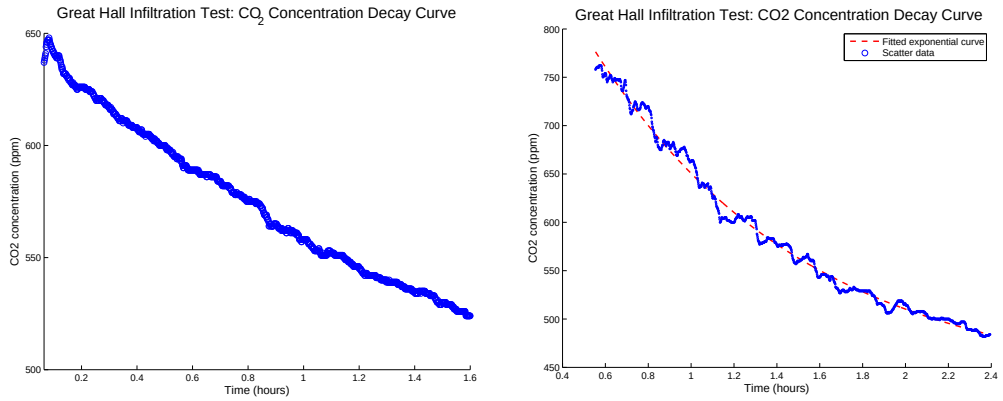

Figure 4.4: (a) Great Hall Infiltration test results (b) Fitted exponential decay curve to infiltration data

Further tests are taken across a range of wind speeds and Figure 4.5 shows a strong correlation between wind speed and infiltration, with an R^2 value of 0.98. Due to time limitations, only four experiments could be carried out, but the quality of the results provide good confidence to the linear trend.

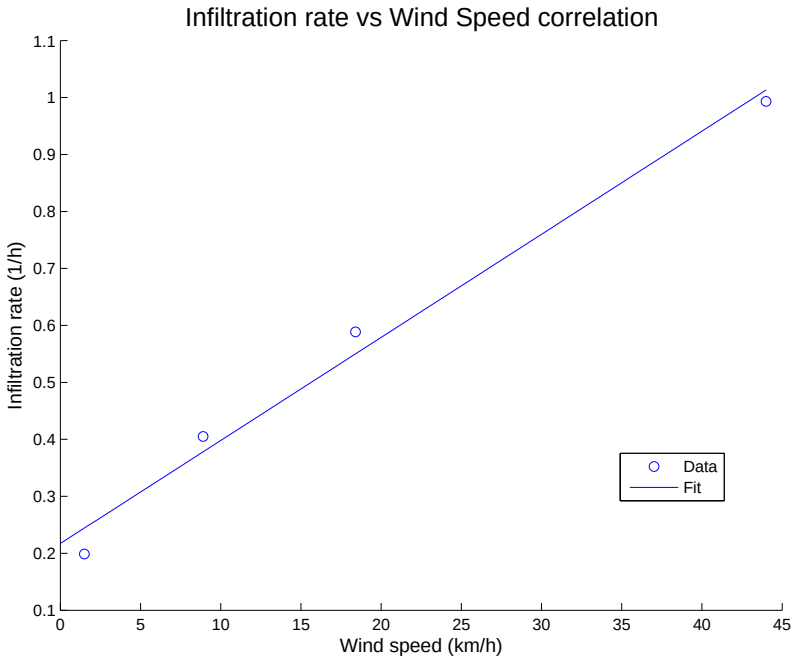

Figure 4.5: Overall infiltration results showing the relationship between infiltration rate and wind speed

The linear relationship between infiltration rate and wind speed is defined as:

$$I = 0.018V + 0.22 \tag{4.4.3}$$

where I is the infiltration rate in $1/h$ and V is the wind speed in km/h.

Equation (4.4.3) is now used in future TRNSYS simulations to dynamically change the infiltration rate of the building based on the wind speed reported from the weather file.

4.5 Model Calibration

One of the most complex features of the Great Hall design is the air flow connection of the Balcony zone above the Great Hall. The hourly air change rate (ACH) between these two zones is difficult to determine experimentally. The method chosen to determine this important factor was a calibration experiment in TRNSYS. A number of TRNSYS simulations were run through MATLAB while each time changing the parameter that defines the ACH between the Great Hall and Balcony zones. After each simulation, an overall temperature residual between experimental and predicted room temperatures was calculated. As can be seen in Figure 4.6, an air change rate of 1.1 produces the minimum residual between experimental measurements and TRNSYS results.

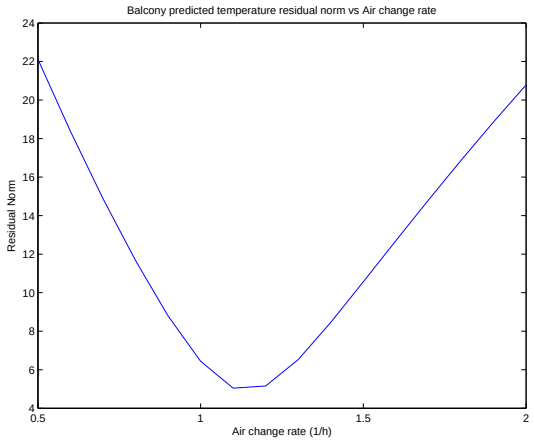

Figure 4.6: Residual plot for Balcony temperature changing the air change rate between Balcony and Great Hall

4.6 New Validation Results

A new set of data for one week is collected for the Great Hall. During this period the BIPV/T system is not operated with the heat pumps or fans, and the room was mostly unoccupied to minimise disturbances. This procedure was to ensure that the core TRNSYS model of the building structure is accurate enough to predict the basic thermal dynamics of the Great Hall and Balcony zones, before attempting to model the whole combined system.

The new validation results show a much closer fit between measured and simulated zone air temperatures for the Great Hall (Figure 4.7).

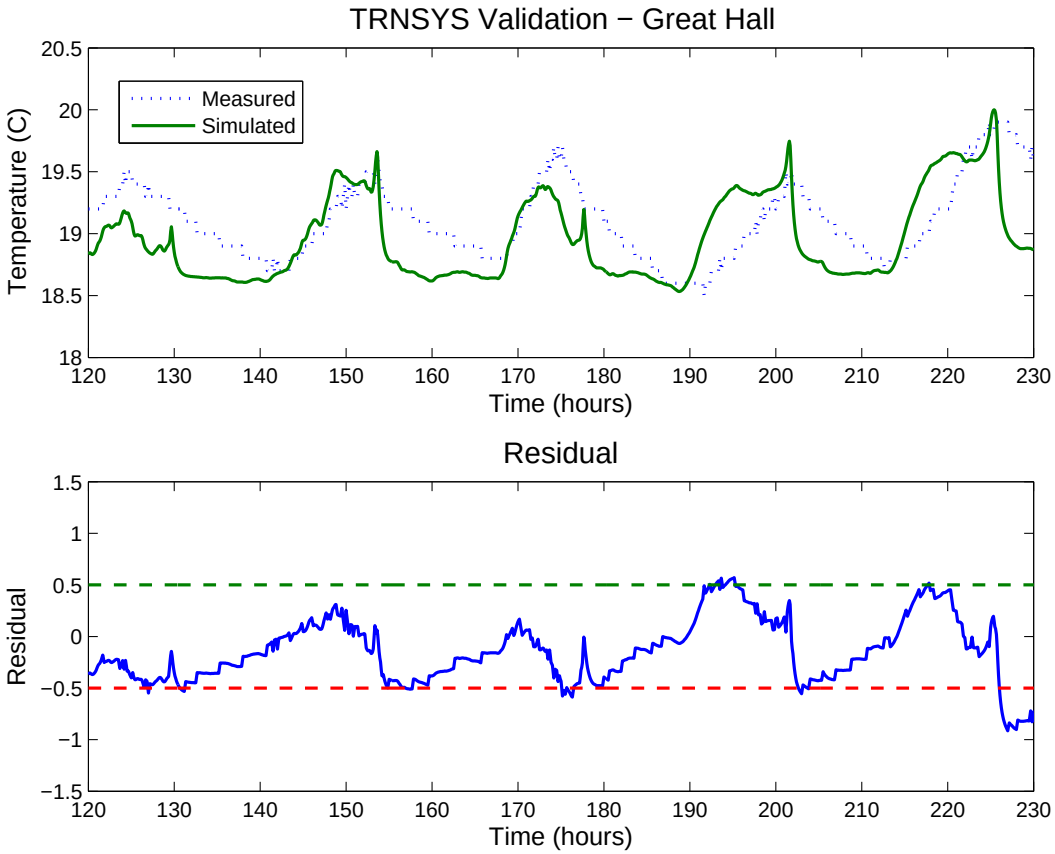

Figure 4.7: Chapman Hall validation study. (a) Model results (b) Residual error

Overall, there is good correlation between the simulated and measured data. The residual plot in Figure 4.7 shows that the predicted zone temperatures

lie almost completely within the acceptable error range of $\pm 0.5°C$. The prediction error for this validation study has a mean of $-0.11K$, and standard deviation of 0.29. Therefore 95% of the data is within $-0.68K$ and $0.46K$ of the true measured value.

The modelled air temperatures experience several sharp drop offs late in the day. The reason for this dynamic is likely due to the angle of incidence of the sun, and the solar view factors for the building windows. A sudden decrease in the amount of solar radiation being absorbed inside the building causes a rapid decrease in the air zone temperature, whereas in reality the thermal mass of the building moderates the air temperatures and the temperature decay is more gradual. This dynamic demonstrates one of the limitations in the TRNSYS software in its ability to model high thermal mass buildings. For walls with high thermal mass, the overall thickness and the ratio of conductivity to density is restricted to fulfil stability criteria while creating the wall transfer functions in TRNBUILD. Improved models will be investigated in future work.

Despite this interesting phenomenon, the accuracy of the model is sufficient to capture the thermal behaviour of the Great Hall for further simulations. Thus the current TRNSYS model for the Great Hall will be adequate to be used for whole system modelling combined with the BIPV/T system, which will be modelled in detail in the next section.

4.7 Chapman Castle BIPV/T Study

The most important renewable energy feature of the Chapman Castle is the $22.6kW$ building-integrated photo-voltaic thermal (BIPV/T) collector system.

The north facing rooves and walls are constructed using PV cells with custom flashing units that allow the panels to connect together in a water-tight fashion such that the PV cells also form the structural unit for the building.

The western half of the north facing PV surfaces forms the ceiling for the Great Hall, the main entertaining area in the castle. These PV panels have in-built air ducts running length-wise directly beneath them to allow an airflow to pass. At the bottom of each duct are motorised flaps which control whether the input air flow to the BIPV/T comes from the Great Hall air or the outside air. At the top of the ducts, another set of motorised flaps direct the output air from beneath the PV panels to either back outside or to the

top of the Great Hall via the upper Balcony area. This mechanism is shown in Figures 4.8 and 4.9.

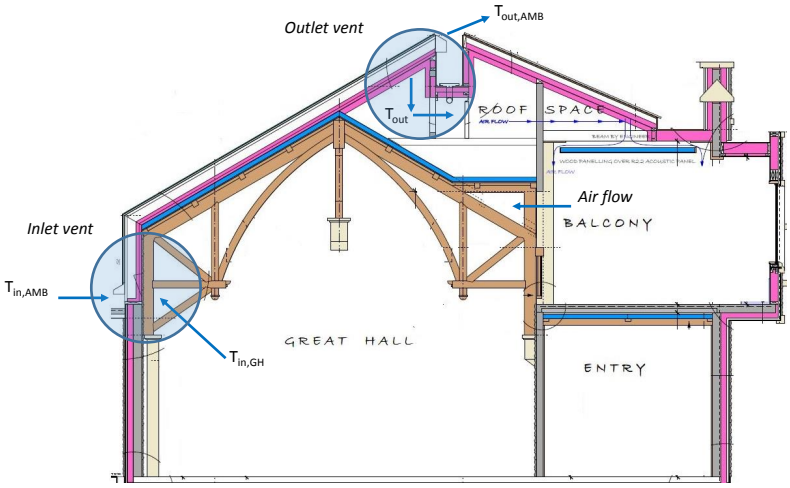

Figure 4.8: Chapman BIPV/T system with inlet and outlet flaps, linking Great Hall and Balcony zones.

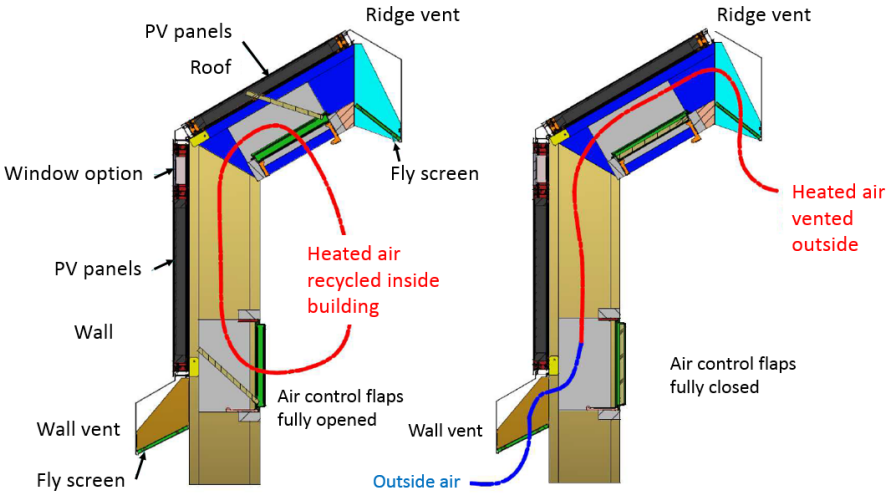

Figure 4.9: BIPV/T system with vents closed for recirculation mode (left) and vents open for PV cool mode (right)

4.8 Data Collection

To validate the BIPV/T component in TRNSYS, the simulation results are compared with real data.

4.8.1 Measurement systems

In addition to the meteorological measurement devices set up to validate the building model, air temperature and air flow speed sensors are required to validate the BIPV/T model. These measurements are used to calculate the rate of useful thermal energy generated through the BIPV/T system, which is defined:

$$\dot{Q}_{thermal} = \dot{m} C_P (T_{out} - T_{in}) \tag{4.8.1}$$

where $\dot{m}$ is air mass flow rate, T is air temperature.

Temperature

K-type thermo-couple temperature sensors are used to measure the input and output air temperatures at the bottom and top of the air duct beneath the PV surface.

Air flow

A TES hot wire thermal anemometer (Figure A.3) is used to measure the air flow speed through the air duct.

4.8.2 Flow distribution between air ducts

The Chapman BIPV/T system comprises 11 air ducts running parallel to each other. The output air from all 11 ducts flows into an attic space spanning approximately 15 metres long, two metres wide, two metres high. The air flow for all 11 ducts is drawn up from the top by a series of six powerful fans mounted along the centre of the back of this attic space.

The air flow rate is only monitored over long periods for one air duct, due to the cost of the hot-wire probe. To adjust for the overall heat gain for all

11 ducts, it is necessary to measure the relative air flow rates in each duct at several constant fan speeds. Irregularities in the attic design mean that the flow distribution across each duct is also irregular and must be determined experimentally.

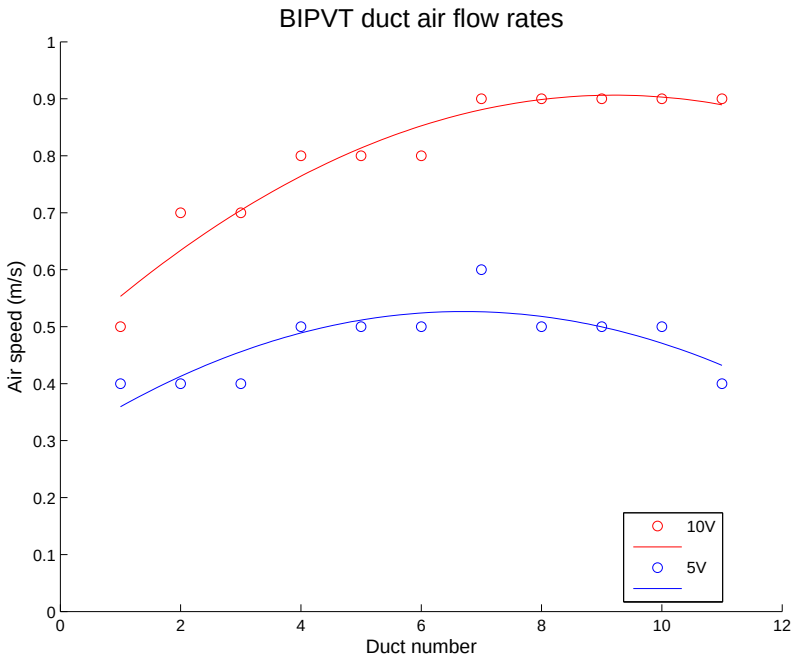

Figure 4.10: Air flow rate distribution across 11 parallel ducts in Chapman BIPV/T system

A multiplication factor can now be applied to the heat gain in one duct to estimate the overall heat gain for the entire system.

4.9 Thermal Performance Curve

Following the same method as described in section 3.4, the general thermal performance of the Chapman BIPV/T system is analysed by plotting the thermal efficiency, η, against the inlet-ambient temperature difference per quantity of solar radiation, $(T_{in} - T_{amb})/G_T$. This analysis shows how efficient the thermal collector is over a range of operating conditions, and provides the two characterising parameters for the thermal collector: $F_R(\tau\alpha)_{av}$ - how well the collector absorbs solar irradiance, and $F_R U_L$ - describing how the collector loses heat.

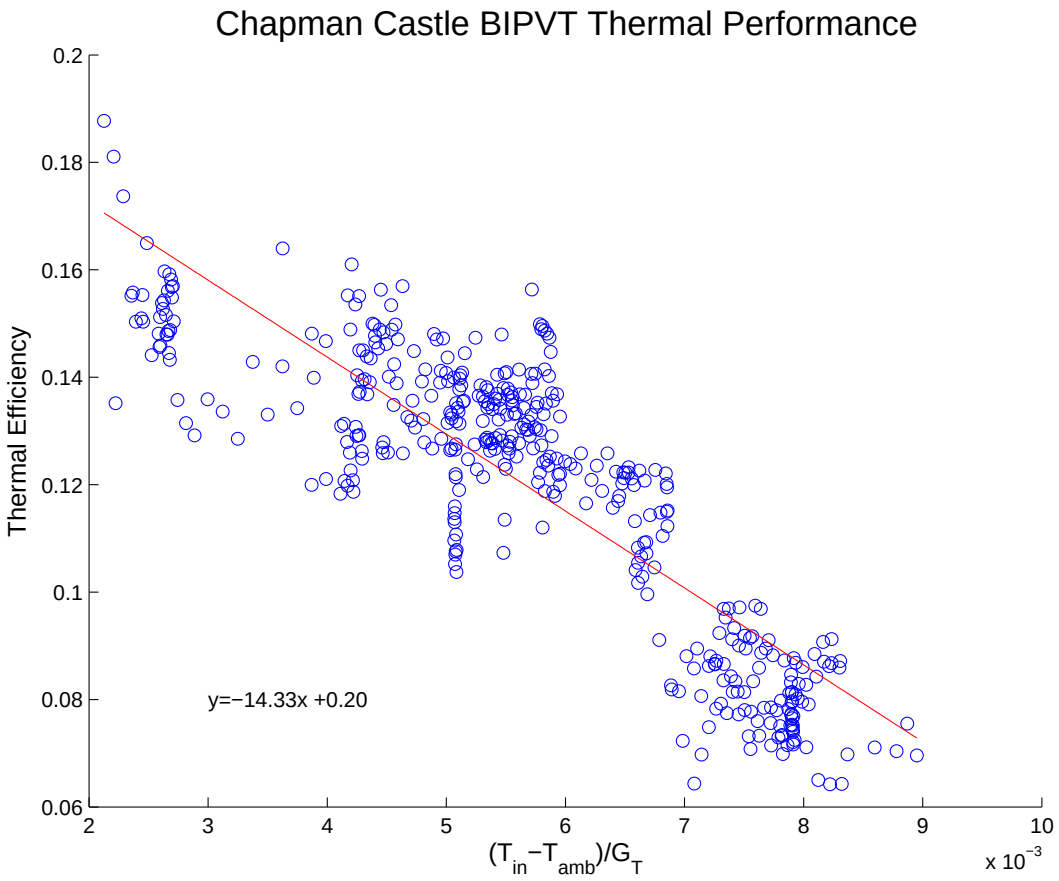

Figure 4.11: Experimental efficiency for BIPV/T system measured between 12pm - 4pm at two fan speeds, $V = 0.80m/s$ from 12-2pm, $V = 0.45m/s$ from 2-4pm in order to produce a range of input and output values.

A least-squares fit for the data produces an R^2 correlation coefficient of 0.75. Coefficients from the fitted linear trend give the parameters of the efficiency model. The two characteristic parameters are computed to be $F_R U_L = -slope = 14.18 W/m^2 C$ and $F_R(\tau\alpha)_{av} = intercept = 0.20$.

Using the following equation, the efficiency of the BIPV/T system may be calculated for any given operating point described by three inputs: input air temperature T_{in}, ambient air temperature T_{amb}, and incident solar radiation: G_T.

$$\eta = F_R(\tau\alpha)_{av} - F_R U_L \left(\frac{T_{in} - T_{amb}}{G_T} \right) \tag{4.9.1}$$

This approach is a useful way for the owner of the BIPV/T system to calculate the efficiency and therefore thermal gain of the BIPV/T system in a simple manner without the use of simulation programs.

4.10 Computational Fluid Dynamics

Computational fluid dynamics (CFD) is a powerful tool for analysing systems involving fluid and heat transfer involving complex geometries and turbulence, which cannot be solved analytically. A CFD study is performed for the Chapman BIPV/T duct system to analyse in detail the heat transfer that occurs between the heated PV lower surface and the air stream, involving relatively complex geometry and input conditions. The base work for the CFD model is covered in detail in section 2.8, and the results of this work are presented in this section. ANSYS-CFX software is used.

4.10.1 Results

The results for the converged CFD simulations are analysed using the ANSYS CFD-POST software. Velocity and turbulence profiles highlight areas of high turbulence due to the inlet and duct geometry, which is related to regions of greater heat transfer. A full-length temperature profile shows the development of the heated air stream length-wise along the duct. The heat transfer coefficient along the PV-surface is used to adjust the TRNSYS model accounting for the unique geometry, to achieve more accurate simulation results.

Velocity and turbulence profiles

The results for the CFD simulation are visualised in the ANSYS post-processing tool, CFD-POST. A velocity contour plot and streamlines trace and map the intensity of the air flow from the inlet, through the duct bends, and along the main tilted duct to the outlet.

The turbulence intensity can also be visualised by plotting the turbulent kinetic energy throughout the duct. It can be seen that the most turbulence occurs at the $30° - 90°$ bend where the fluid on the northern side is forced into the PV surface and turns a sharp angle. This part contributes to the very high wall HTC at this area as shown in Figure 4.14. In addition, a major

a major turbulent eddy is formed where the flow separates on the southern side.

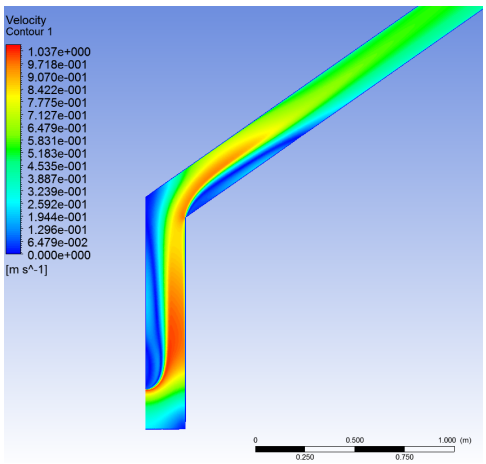

(a) Velocity field for the BIPV/T system simulated in ANSYS-CFX

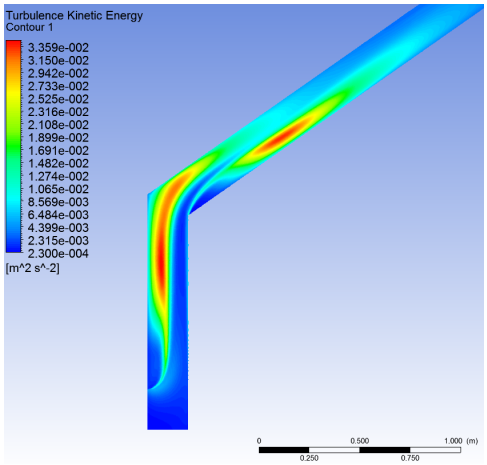

(b) Turbulent kinetic energy (k) field for the BIPV/T system - simulated in ANSYS-CFX

4.10.2 Temperature Profile

The temperature profile is visualised along the ducts and provides insight into the heat transfer dynamics between the air stream and the PV surface. The development of a thermal boundary layer can be seen along the length of the PV surface, and also the bottom surface of the duct due to radiation between the upper and lower duct surfaces. The overall temperature rise between the inlet and outlet is $15°C$, which is a standard temperature difference during peak operation at the Castle.

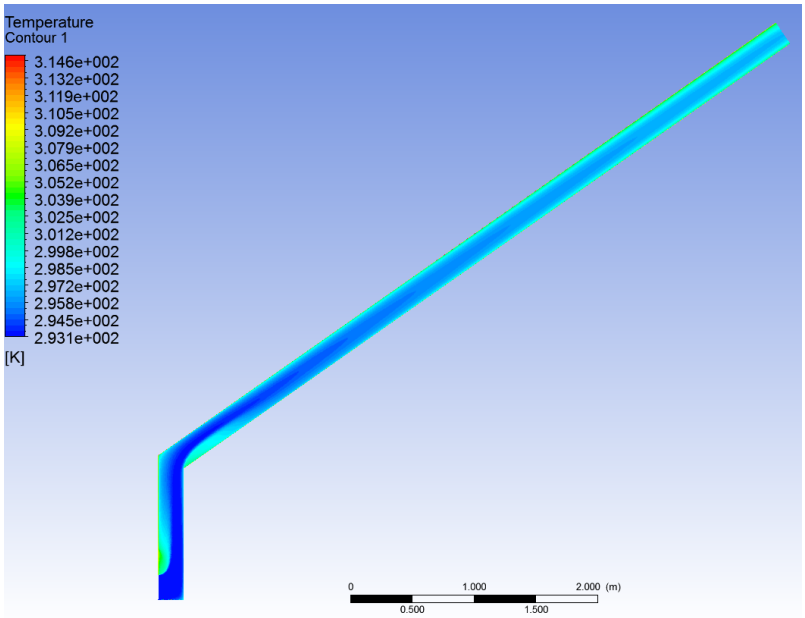

Figure 4.13: Temperature field through the BIPV/T duct system - simulated in ANSYS-CFX

PV surface heat transfer coefficient (HTC)

When a fluid flows past a surface, and there is a temperature difference between the fluid and surface, a thermal boundary layer develops, a region where heat transfer occurs due to conduction and convection. Outside of the thermal boundary layer, the fluid maintains its free stream temperature. The non-dimensional Nusselt number is a ratio between advective and diffusive convective heat transfer coefficients, and conductive heat transfer, which occurs normal to a boundary surface. The Nusselt number can be used to calculate the theoretical HTC between a surface and fluid due to forced convection. The theoretical value for heat transfer in the BIPV/T system will be compared with the numerical value calculated in ANSYS based on the simulation results. The Nusselt number Nu is defined as:

$$Nu = \frac{hx}{k} \tag{4.10.1}$$

where h is the HTC, x is the characteristic length, which for duct flow is the hydraulic diameter D_h - the characteristic length for duct flow, calculated as the cross sectional area divided by the perimeter and k is the conductivity of the fluid.

The Nusselt number can be calculated empirically as a function of the Reynolds number and the Prandtl number using a Dittus Boelter heat transfer correlation, depending on the flow state of the fluid - whether it is stagnant ($Re = 0$), laminar ($Re < 2300$) or turbulent ($Re > 2300$). The Reynolds number for duct flow is:

$$Re = \frac{VD_h}{\nu} \tag{4.10.2}$$

The Reynolds number for the flow of interest with air having kinematic viscosity of $1.51 * 10^{-5} m^2/s$ flowing at an average velocity $V = 0.5 m/s$ through a duct with hydraulic diameter $D_h = 0.33m$, the Reynolds number is $11,000$ which exceeds the limit for transition to turbulent flow, $Re > 2300$. The Dittus-Boelter heat transfer correlation for a turbulent flow is used:

$$Nu = 0.023 Re^{0.8} Pr^{0.4} \tag{4.10.3}$$

where Pr is the Prandtl number, which for air at $20°C$ is 0.71.

The Nusselt number, in the context of a BIPV/T system, is used to calculate the HTC between the hot PV surface and the air stream, and can be found by re-arranging Equation (4.10.3):

$$h_{air} = \frac{Nuk_{air}}{D_h} \tag{4.10.4}$$

In CFD-POST, the HTC along the surface of the BIPV/T system is calculated numerically. A line plotted along the length of the vertical and tilted planes samples the wall HTCs along the PV surface. The HTC along the surface is shown in Figure 4.14:

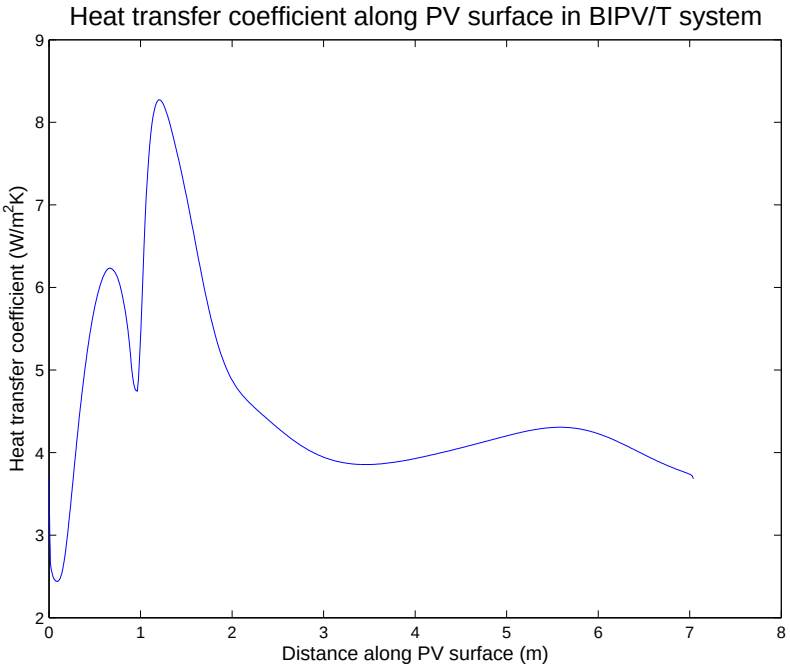

Figure 4.14: HTC along the length of the PV surfaces of the BIPV/T system. $0.00 - 0.96m$ is on the vertical PV surface, $0.96 - 7.00m$ is on the titled 30° surface.

Comparison of CFD against theory

The theoretical value for the HTC between air and wall surface in a duct can be compared against the CFD solution to evaluate the effect of the irregular geometry in the real system.

The theoretical heat transfer number is calculated using Equations (4.10.3) and (4.10.4). Assuming a characteristic length of $D_H = 0.33m$, air conductivity of $0.0257W/mK$, Reynold's number of $11,000$, the Nusselt number for this flow is 34.2 and the HTC is $2.64W/m^2K$.

CFD results claim a HTC of $5.17W/m^2K$ for the vertical surface and $4.49W/m^2K$ for the tilted surface. The average HTC across the whole length, considering the respective lengths of tilted and vertical surfaces, is $4.59W/m^2K$. Thus the HTC is enhanced by 96% in the vertical channel, and 70% in the tilted channel, compared to the theoretical HTC for a standard straight duct BIPV/T system. The extra turbulence produced by the bends is shown to increase the HTC significantly.

Note that the higher HTC value used in simulation does not necessarily improve the overall performance, as the duct bends contribute to higher fan work required to overcome pressure losses, which has been taken into account in the model. Pressure losses due to duct geometry, and therefore fan work, is calculated in section 2.7.3.

This result is accounted for in the TRNSYS simulation model by reducing the channel height in each of the TRNSYS components such that the HTC is equal to the CFD value. As seen in the mathematical derivation of section 2.6, Equation (2.6.10) shows that the channel height affects the HTC between the channel surfaces and the air stream. By rearranging Equation (4.10.4), an expression for the hydraulic diameter is defined:

$$D_{h,CFD} = Nu\frac{k}{h_{CFD}} \tag{4.10.5}$$

where $D_{h,CFD}$ is the new hydraulic diameter based on the new HTC, h_{CFD}.

Rearranging the formula for hydraulic diameter of a rectangular duct $D_h = 2WH/(H+W)$, the new effective channel height $H_{CH,CFD}$ is calculated:

$$H_{CH,CFD} = \frac{D_{h,CFD}W}{2W - D_{h,CFD}} \tag{4.10.6}$$

The new channel heights are computed from Equation (4.10.6), resulting in the values $H_{CH,CFD} = 0.09m$ and $H_{CH,CFD} = 0.11m$ for the vertical and tilted sections respectively. These values are reduced from measured values of $0.2m$.

TRNSYS simulations are now performed with the default values for channel height, and the CFD-adjusted channel heights, and the norm of the residuals between predicted and measured output temperatures are compared over a 50-day period.

The new CFD-adjust channel temperatures improves the residual error between simulated and measured data by 1.9% compared to the case where the theoretical value for the HTCs are used.

This result shows that using a CFD-derived adjustment to the TRNSYS simulation does improve the resulting simulated fit to experimental data, but by only a small margin. However, this analysis has improved the understanding of the system, and it can be concluded that the sensitivity of the validation result to the PV surface HTC is not as significant as expected and will not significantly alter the optimal design.

4.11 TRNSYS BIPV/T model

The BIPV/T system is modelled in TRNSYS using the type 567 component supplied by the TESS electrical library. The solution process is described in section 2.6. Required inputs include: inlet air temperature and flowrate, ambient temperature, incident total and diffuse radiation, solar incidence angle, top heat loss coefficient.

4.11.1 Sensitivity Analysis

The first step towards producing an accurate model of an existing BIPV/T system is to create a simple model with a set of known experimental data and approximate values for the system parameters. A sensitivity analysis can then be carried out on the TRNSYS BIPV/T model to determine the most important parameters for modelling a BIPV/T system. Parameters which cannot be measured directly or with certainty can be optimised to a value that best matches the model outputs to the measured data.

A series of simulations are run in MATLAB, where one parameter from the total set is perturbed, and all other parameters are held constant at their base values. The process is repeated for all variables. An influence coefficient is calculated for each parameter based on the change of the objective value compared to the original base-case value, as was done in Equation (4.3.2). For this sensitivity analysis, the objective value is the output air temperature, which determines the useful energy gain. The chosen parameters are:

- PV emissivity e
- Glass cover conductivity k_{cvr}
- Glass cover thickness th_{cvr}
- Resistance of substrate R_{sub}
- Back resistance R_b
- Channel height h_{CH}

The results for the sensitivity analysis are given in Figure 4.15.

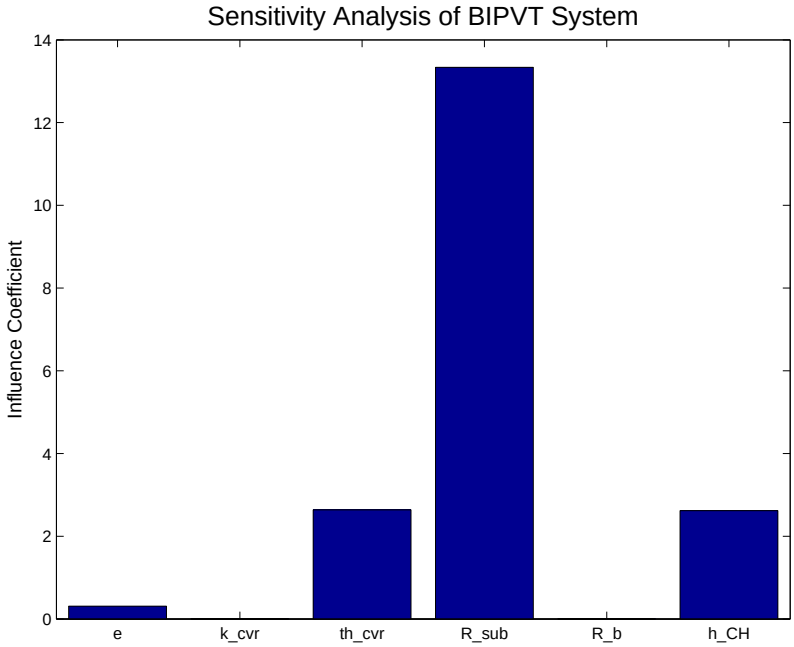

Figure 4.15: BIPV/T sensitivity analysis results

Channel height only has a small influence on output temperatures as expected from the CFD study in section 2.8.

The backing resistance R_b has negligible impact on the output temperature, because the well insulated channel prevents any heat transmittance to the zone.

The glass cover conductivity also has no effect because the glass is so thin that it does not restrict heat flow to the air stream.

The influence coefficient for the resistance of the PV module (R_{sub}) has the most significant effect on the simulation result. However, thermal properties of PV module components are difficult to measure accurately and these values are not supplied with standard PV cell specification data sheets.

Therefore, the technique selected to find a more accurate value for this parameter is calibration with experimental data. Estep (2013) also uses a calibration technique with TRNSYS to find the value for the PV substrate resistance that best matches the useful thermal energy gain.

4.11.2 BIPVT Calibration

The thermal resistance of the PV substrate material used in the BIPVT system is difficult to measure with sufficient certainty. Hence, this parameter was further optimised.

A series of simulations were run, using MATLAB to automatically vary the value of R_{sub} between the range of 0.002-0.016 in small increments, calling TRNSYS to run the simulation with only a change in the value of R_{sub}. See section 2.9 for a description of the method used in MATLAB to automate simulations.

After each simulation, the overall simulation error between the predicted output air temperatures and true measured air temperatures was determined. By plotting this overall error against the value of the parameter, a more accurate value for the parameter is found that corresponds to the minimum residual.

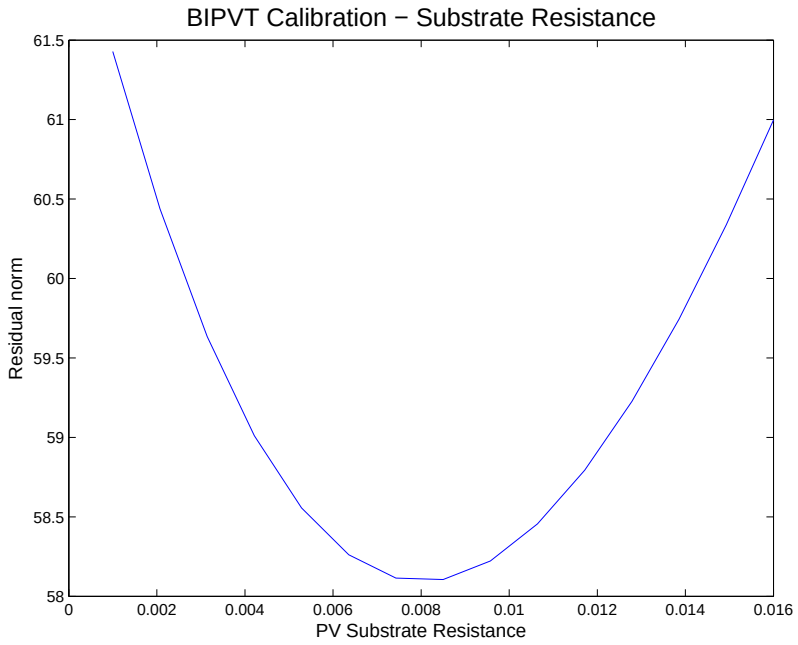

Figure 4.16: PV substrate resistance calibration

Figure 4.16 shows a clear minimum residual for $R_{sub} = 0.008$. This value is only 20% lower than the default value, but the norm function in Figure 4.16 has a high curvature so this improvement is significant in terms of the impact on the predicted air temperature.

4.11.3 TRNSYS Validation of BIPVT module

The calibrated values for the BIPVT module are corrected in the model and a simulation is run for the BIPVT system over one day during clear skies and strong radiation. During this day, the fans were operated at a constant voltage of $5V$, producing an average flow rate of $0.5m/s$ across all air ducts.

Figure 4.17 shows that over a week long period, the simulated values of output air temperature match well through both night and day-time periods. A correlation analysis between measured and simulated output temperatures gives a strong correlation with a R^2 value of 0.96.

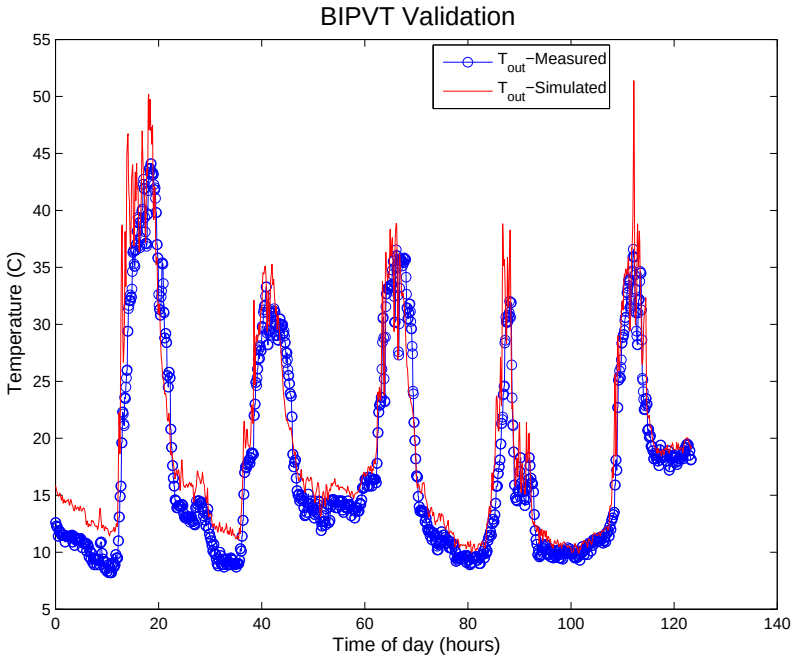

Figure 4.17: BIPVT validation results showing a strong correlation of $R^2 = 0.96$, between simulated and measured values of the output air temperature.

4.11.4 BIPVT Parameters

Table 4.11.4 summarises the parameters that best fit the Chapman Castle BIVPT system for use in TRNSYS simulation.

Parameter	Value	Unit
PV absorptance	0.9	Fraction
PV emissivity	0.829	Fraction
PV resistance	0.008	$h.m^2.K/kJ$
Channel emissivity	0.9	Fraction
Back resistance	1.39	$h.m^2.K/kJ$
Channel height	0.17-0.195	m

4.12 BIPV/T Optimisation

For optimal use of the BIPV/T system during normal operation, it is useful to know what operating conditions will provide the most effective means of heating the building. Effective in this case is to heat the building to the required temperature given the amount of available solar radiation on a given day.

The two decision variables for BIPV/T operation are air flow rate - what speed to operate the fans, and control strategy - under what meteorological conditions should the system be operated.

4.12.1 Optimal Flow Rate

The air flow rate through the BIPV/T system affects several variables: the friction pressure loss, temperature rise between inlet-outlet, useful thermal energy rate.

Friction losses

CFD analysis was carried out on the BIPV/T system based on the geometry used in Chapman Castle system, as described in section 2.8. For this particular analysis, the pressure drop between the inlet and outlet of the BIPV/T duct is measured for a range of four air flow rates between $0.25m/s$ and $1.5m/s$. A parabolic curve fits the data well, resulting in the following relationship:

$$\Delta P = 1.64V^2 - 0.046V \tag{4.12.1}$$

where ΔP is the pressure drop measured in Pa and V is the cross-section averaged air flow velocity measured in m/s. This relationship is validated by the theoretical calculation for pressure loss in a duct with a 90° entrance bend ($K_L = 1.1$), 30° bend ($K_L = 0.4$), and sharp exit to attic ($K_L = 1$).

The fan work required to move a total volume flow rate $\dot{V}$ against a certain pressure difference ΔP, with thermal conversion ratio $\eta_f = 0.85$, is defined:

$$Q_{fan} = \frac{\dot{V}\Delta P}{\eta_f} \tag{4.12.2}$$

Figure 4.18 shows that even at high flow rates, the pressure drop is low, and thus frictional losses are negligible. At a flow rate of $2m^3/s$, only $6W$ of fan work is required to overcome the frictional losses across all eleven ducts.

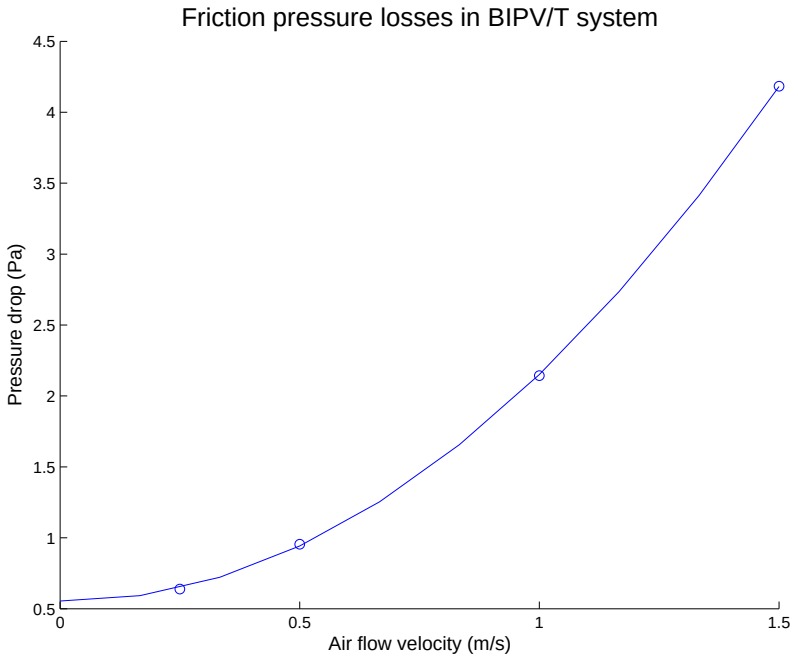

Figure 4.18: Pressure drop across BIPV/T ducting due to frictional losses

Temperature Rise

The temperature rise between the inlet and outlet is strongly correlated to the air flow rate. A very slow air flow rate will result in very hot air but at such a slow rate that the heat loss from the building will dominate due

to BIPV/T ventilation. In contrast, at high flow rates, large volumes of air are circulated, but there is not sufficient time for the air to be heated significantly, so that the the temperature rise is very small, and the system is not effective.

A large amount of measured data is collected across a four month period of BIPV/T operation. Figure 4.19 shows the temperature rise effected by the BIPV/T system for a range of air flow rates. The data illustrates an exponential decay in the maximum temperature rise possible as the air flow rate increases. The formula of Equation (2.6.16), which is derived from first principles, shows the presence of an exponential relationship, however this equation is non-separable for an explicit expression in ΔT. Thus, the relationship between temperature rise and flow rate is defined:

$$\Delta T = a \exp\left(-bV\right) \tag{4.12.3}$$

where the constants a and b are found from a grid search by minimising the least squares error subject to the constraint that the curve encloses all the data below it. This trend represents the maximum possible temperature rise across the BIPV/T system under optimal solar and ambient conditions. All data points below this maximum are a result of sub-optimal solar and ambient conditions.

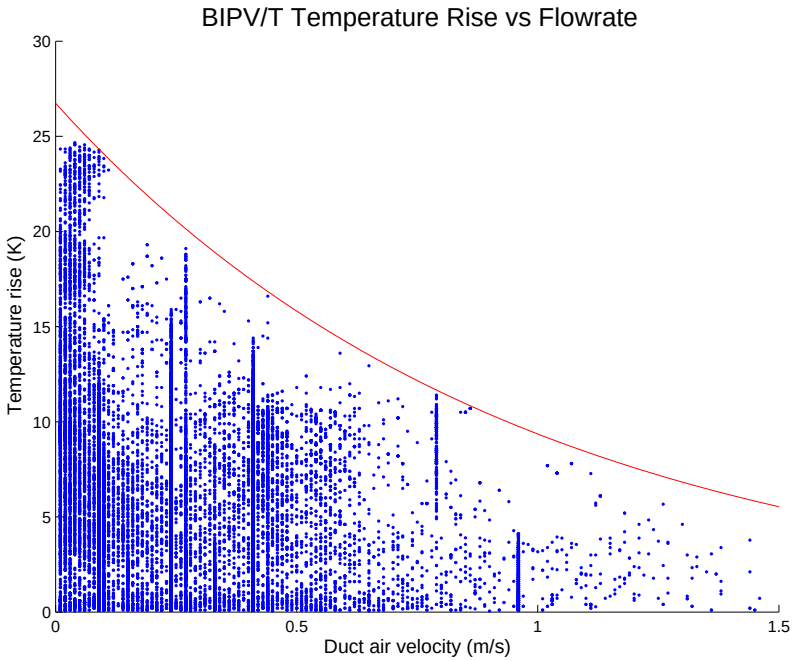

Figure 4.19: Temperature difference between inlet and outlet of BIPV/T system for a range of air flow rates

Electrical efficiency

The electrical efficiency of the PV array is dependent on the air flow rate. As shown in Figure 4.19, the outlet air temperature, and thus mean air temperature under the PV panels is greater at lower air flow rates. For this case, there is less heat transfer between the PV surface and air, leading to higher PV cell temperatures.

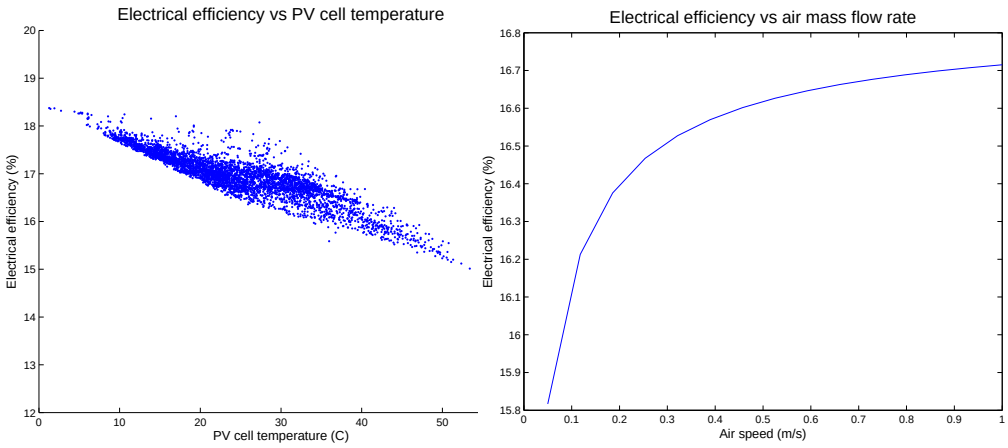

(a) (b)

Figure 4.20: Electrical efficiency as a function of (a) PV cell temperature (b) air flow rate

Figure (4.20a) shows how the electrical efficiency decreases linearly with an increase in PV cell temperature, based on a 50-day period of data. Electrical efficiency can vary from 14% for over-heated PV panels to up to 18.5% for cool PV panels, for this particular PV model.

The relationship between electrical efficiency and air flow rate can be seen in Figure 4.20b. The average electrical efficiency is calculated for a period with a variety of flow rates. This relationship is incorporated into the overall energy balance to determine the optimal mass flow rate.

Useful thermal energy

To find the optimal air flow rate that produces the most effective heat gain for the building, the useful energy gain, a factor of both temperature rise and flow rate is shown in Figure 4.21. The useful energy gain is defined:

$$Q_u = (\rho A C_P) V \Delta T \tag{4.12.4}$$

where ρ is air density, A is duct cross-sectional area, V is the air flow velocity, C_P is the specific heat of air, ΔT is the temperature rise across the duct.

Thus, the total overall form of the relationship between air velocity and thermal energy gain is written in the form:

$$Q_u = a\rho AC_P V \exp(-bV) \tag{4.12.5}$$

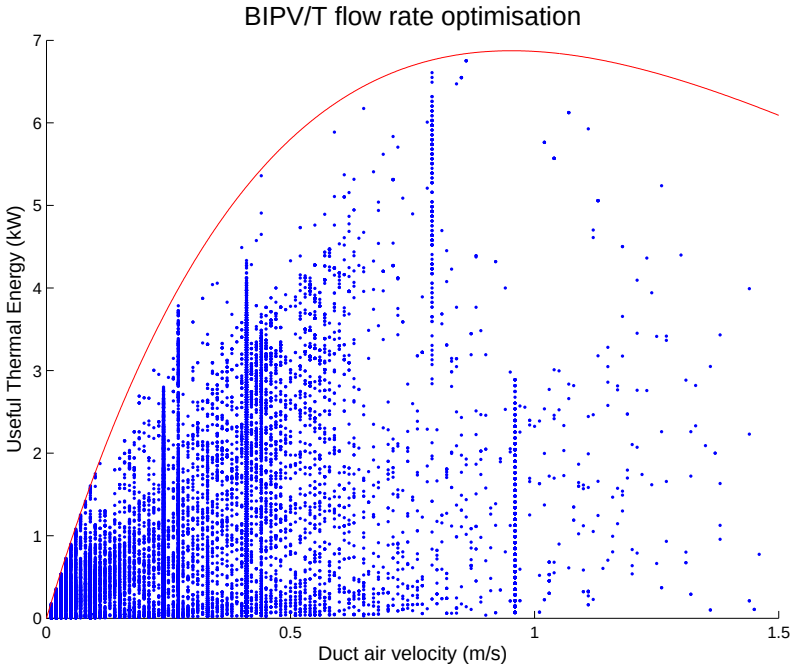

Figure 4.21: Useful thermal energy gain from BIPV/T system from measured data for a range of air flow rates

Figure 4.21 shows that there exists an optimal flow rate between the minimum and maximum possible flow rates. Using a similar method to Figure 4.19, the maximum useful energy gain formula of Equation (4.12.5) can be fitted to the data to yield the curve in Figure 4.21. The peak occurs with an average air speed of $0.95m/s$, or equivalently, an air flow rate per collector area of $0.031kg/s.m^2$. This optimum air speed will result in the maximum thermal energy output.

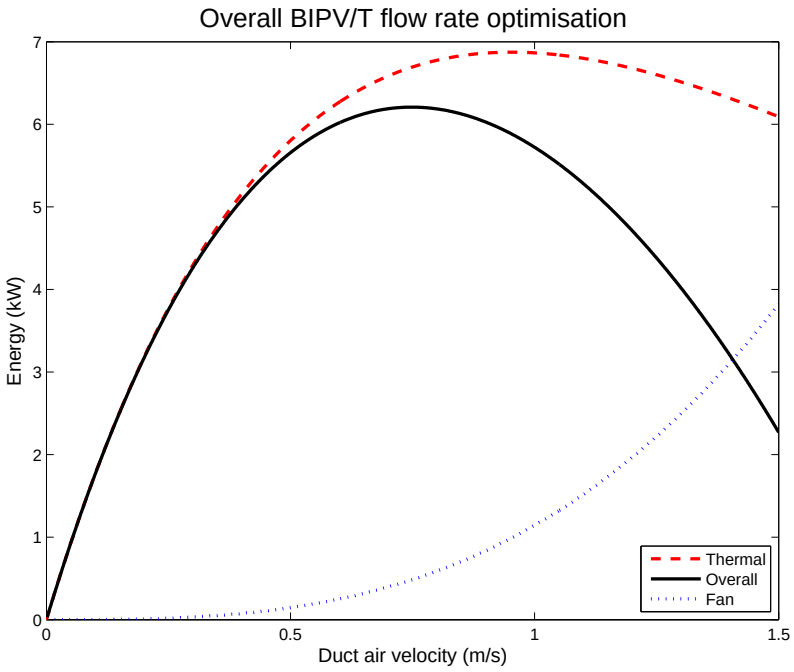

Figure 4.22: Total energy balance for BIPV/T system for flow rate optimisation

However, the increase in fan work at high flow speeds begins to be a significant factor, altering the optimum flow rate in the overall energy balance. Figure 4.22 shows the increasing amount of fan work for higher flow speeds means. The derivation of the overall energy balance, including consideration of the pressure losses along the duct, is explained fully in section 2.7.

Therefore for the most economical use of the BIPV/T system, the air speed relating to the maximum point on the overall energy balance curve should be used. This optimum flow rate is $0.75m/s$, or mass flow rate per collector area of $0.025kg/s.m^2$.

The current fans installed for the Chapman BIPV/T system are already close to this result, so are therefore well selected to achieve the goal of producing optimal thermal gain. Duct air speeds of up to $0.75m/s$ are at the upper limit of the fan's operation and thus the fans should always be set at their maximum air flow rate.

4.13 System Validation

In the previous sections, detailed modelling and validation studies for separate components of the Chapman Castle have been completed.

The building model was originally validated in Figure 4.7 of section 4.6 during summer months when the BIPV/T ventilation system was not operating due to the warm temperatures. This helped to simplify the initial validation study, isolating the building from the complex air ventilation system, allowing the construction materials and meteorological inputs to the building to be studied.

In addition, the BIPV/T component used in TRNSYS was validated against measured data for the output air temperatures. The results in Figure 4.7 of section 4.7 showed a good fit between the measured and simulated data.

In this final section, the two components - building model and BIPV/T model, will be combined and the overall system will be modelled and validated against real data. A 50 day period during autumn is used for this validation study when the BIPV/T system is operating frequently.

4.13.1 Method

During BIPV/T operation, an air-water heat pump located in the attic space at the BIPV/T outlet drives the air flow, and uses the heated BIPV/T output air to heat water that is diverted to the concrete floor slabs in other zones in the building. In this mode, the Great Hall essentially acts as a heat source for the rest of the building, as it is occupied less frequently, and is at times cooled below ambient temperature during this mode of operation, in order to heat other occupied zones where the heat is required.

The output air temperature that is ventilated through the Great Hall is therefore reduced by the quantity of heat transferred from the air stream to the water stream. The water stream flows through the plumbing network to where it is required, which is typically either for heating the bedroom or kitchen concrete slabs. The new output air temperature which is vented into the Balcony zone is:

$$T_{out,HP} = T_{out,BIPVT} - \frac{\dot{Q}_{HP}}{\dot{m}_{HP} C_{P,w}} \tag{4.13.1}$$

where $T_{out,HP}$ is the air temperature ventilated through the Great Hall zone, $T_{out,BIPVT}$ is the air temperature exiting the BIPV/T duct, $\dot{Q}_{HP}$ is the measured quantity of heat transferred from air to water, $\dot{m}_{HP}$ is the measured mass flow rate of water through the air-water heat pump, $C_{P,w}$ is the specific heat capacity of water.

TRNBUILD is used to set up the ventilation of air from the BIPV/T system back into the air zone. A new ventilation type is created with air flow rate proportional to the measured air duct speed, scaled up using the study of Figure 4.10 in section 4.8.2, and temperature equal to $T_{out,HP}$ calculated from Equation (4.13.1).

4.13.2 System Validation Results

Figure 4.23 shows the validation results for the 50 day (1200 hour) period during autumn. Due to the increasing complexity of this overall system model from unmodelled disturbances, larger error margins between simulated and measured data are to be expected. With more measured variables, the overall measurement uncertainty also increases. Despite these uncertainties, weekly trends are tracked and many of the daily peak temperatures are captured well. The period surrounding the peak daily temperatures is the most important time for accurate modelling as this period is when the the recirculation mode is active, and building temperature is used as the input to the BIPV/T system.

Figure 4.23(b) shows the correlation between simulated and measured peak daily temperatures with $R^2 = 0.61$ and mean absolute percentage error (MAPE) of 9.4%. The errors are normally distributed about a mean of 0.55, with standard deviation of 1.59. Therefore 95% of predicted air temperatures fall between $-2.6K$ and $3.7K$.

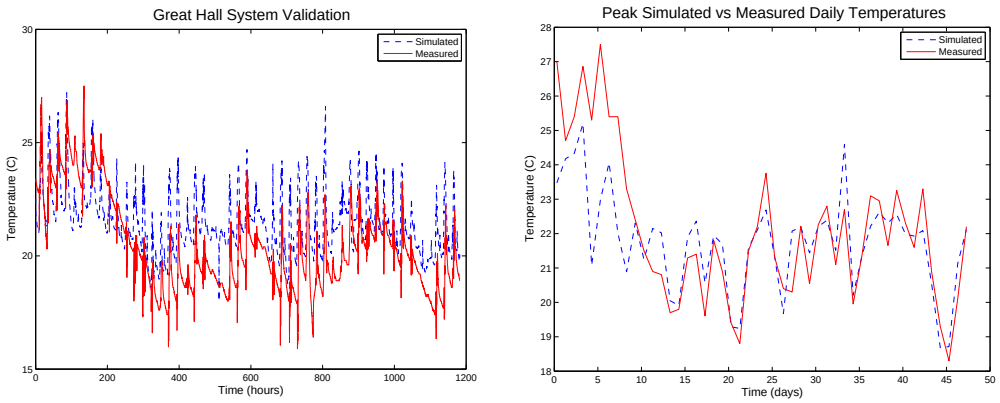

Figure 4.23: System Validation comparing simulated versus measured room temperatures over a 50-day period (a) Hourly room temperatures (b)Peak daily room temperatures

4.13.3 Thermal Gain Prediction

To provide confidence for house design a more practical metric for validating the model is the daily and weekly thermal gain from the BIPV/T system. These metrics are computed by determining a moving integral of the predicted thermal gain over a daily and weekly window respectively. The results are shown in Figure 4.24. The correlation coefficient of the modelled to measured data is $R^2 = 87\%$ for the daily moving integral in Figure 4.24(a) and $R^2 = 0.71$ for the weekly moving integral in Figure 4.24(b). Note that the mean percentage error for weekly prediction of thermal gain is 10.3%. These results show the model is more than sufficient for design.

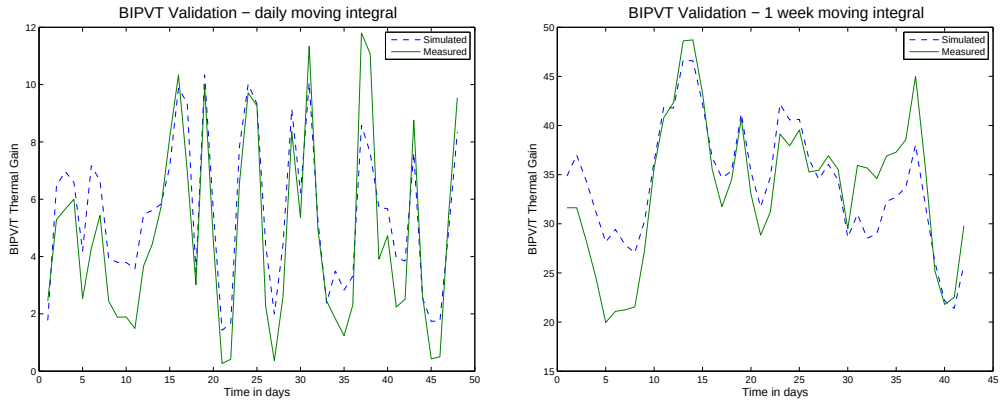

Figure 4.24: BIPVT Validation over a 50-day period (a) Daily average for thermal gain (b) One week moving average for thermal gain

4.14 Long term performance

With the completion of a full system validation of the Chapman Castle, long term simulations may be performed to estimate thermal dynamics of the Castle through a typical year, and importantly to estimate the potential thermal and electrical gains from the BIPV/T system. The respective summer-time and winter-time thermal behaviour of the building can now be investigated. Overall performance measures include yearly energy generation from a particular renewable energy feature, and corresponding monetary savings, which allow the calculation of pay-back periods for these installations.

4.14.1 Method

Several model simplications must be made for the long-term simulation. As no real data is available for the input air temperature or mass flow rate through the BIPV/T system, these parameters must be estimated based on real operation data.

For long-term simulations, the vent position protocol must be specified. The control strategy employed by the Great Hall control systems is to open the vents when the total solar energy power rate collected by the whole $22.6kW$ PV array exceeds $10kW$, and simultaneously the Great Hall core temperature is lower than the desired temperature of $20°C$. By these two criteria, it is ensured that the building is only heated when required, and when suf-

ficient solar resources are available. Therefore, using this control criteria in TRNSYS, the input air temperature for the BIPV/T system is set to either the Great Hall room temperature, or the ambient air temperature. See Figure 4.9 for a schematic showing the two venting modes. When the vents are open, the BIPV/T system operates, with mass flow rate equal to the optimal rate as determined in section 4.12.1.

4.14.2 BIPV/T Output

A long-term simulation is now performed, and total rates of thermal and electrical energy output are recorded. Figure 4.25 shows the total quantity of thermal and electrical gains for each month for a typical year in Christchurch. The quantities shown represents the maximum quantities available. During warmer summer months, although space heating is not required, the excess thermal energy may be used for hot water pre-heating through use of the heat pumps located in the BIPV/T outlet attic space. Figure 4.25 provides a useful guide for monthly budgeting of thermal and electrical resources and future forecasting. Electrical gains quoted are for the 11.7kW ducted PV array only. To estimate total electrical gains from the entire 22.6kW PV array, use a scaling factor of 1.9, accounting for the higher electrical efficiency of the ducted PV array.

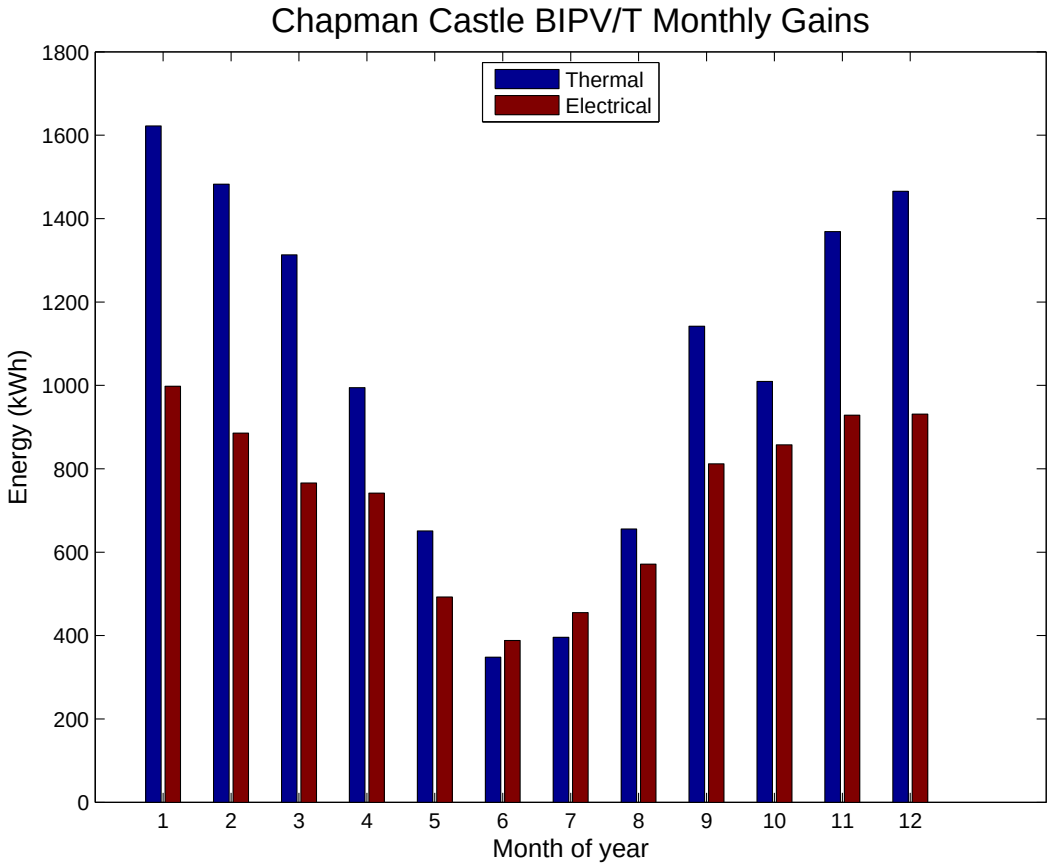

Figure 4.25: Chapman Castle thermal and electrical energy output from ducted PV panels

4.15 Conclusions

In this chapter, a detailed thermal analysis of the Chapman Castle was undertaken. Architectural plans for the building, along with a full set of specifications describing the structural materials and systems were used to create a simplified three-dimensional model of the Great Hall in TRNSYS using the add-on packages TRNSYS-3D with Google Sketchup. A sensitivity analysis for the initial model parameters revealed the key parameters to be modelled in further detail, leading most notably to the refinement of the prediction in the air infiltration rates by an experimentally derived wind speed dependency. New validation results for the building model show a satisfactory fit to measured data.

The BIPV/T system was also studied in detail, being the most important renewable energy feature of the Chapman Castle. Experimental testing and data collection allowed the performance of the BIPV/T system to be characterised. CFD study results shed light on the fluid dynamics of the flow in the irregular duct geometry and showed higher HTCs than predicted by theory. The channel height was adjusted using the CFD calculated HTCs for the two PV orientations, and the validation accuracy was improved by 1.9%.

The TRNSYS model for the BIPV/T system was described mathematically, and real data was used to validate the predicted output temperatures over a one week period.

A system validation was completed, combining the validated models for the building and BIPV/T system, incorporating an air-water heat pump in the ventilation system. A good match between measured and simulated data provides confidence in the model to perform long term simulations.

Long term simulations were completed with the validated model, and used to estimate the monthly thermal and electrical gains from the BIPV/T system.

Finally, an optimisation study based on experimental data was carried out. A relationship between the air flow and the maximum thermal energy gain, electrical efficiency and fan work was established and resulted in an optimal flow speed of $0.75m/s$. This flow speed is at the upper limit of the current fan's capabilities, therefore the fans should always be run at their maximum speed to maximise energy output.

Chapter 5

Transportable Building Study

5.1 Introduction

The second case study to be analysed is the new concept house designed by fellow masters student Sean Cooney in conjunction with Stonewood Homes.

The building's design has incorporated many of the proven energy efficient features of the Chapman Castle into a smaller scale proof of concept that may be replicated for mass production. The building is designed to be energy positive, well insulated, transportable, economically viable, and quick to construct on site.

Key features of the building include a BIPV/T system, high thermal mass, Versipanels (structural insulated panels), and transportability.

A TRNSYS model has been developed for this simple building based on architectural plans supplied by Sean Cooney, drawn up by drafters at Stonewood Homes. The final rendered concept is shown in Figure 5.1.

Figure 5.1: Rendered view of the experimental concept house design.

5.2 Design Specifications

The single-zone building consists of a bedroom and living room separated by a bathroom which extends two-thirds width.

A high thermal mass construction is employed in the building's base. A concrete rib-raft slab forms the foundation, with plastic water tanks integrated into the slab. Once filled with water, these tanks increase the thermal mass of the structure, but can be emptied during transportation to decrease the overall weight during transit. A concrete south wall provides additional thermal mass and passive solar collection during winter with low solar incidence angles. In addition to the concrete skeleton, all walls are constructed with 100mm structural insulated Versipanels, and the roof uses a Conqueror panel. Northern and southern roofs are tilted at 20°. Further details are given in Table 5.1.

Type	**Material**	**Thickness** $[mm]$	**R-Value** $[m^2.K/W]$	**U-Value** $[W/m^2.K]$
Wall (N)	VersiPanel	104mm	2.15	0.46
Wall (E,W)	VersiPanel	104mm	1.65	0.61
Wall (S)	VersiPanel	104mm	1.86	0.54
Roof	Conqueror PIR panel	125mm	5	0.2
Concrete floor slab	Concrete $11.18m^3$ Water tanks $6.08m^3$	520mm	3.24	0.31

Table 5.1: Construction material thermal properties

5.3 TRNSYS Building Model

In Google Sketchup TRNSYS3D, a shading surface was created above the northern tilted roof to account for the shading that the BIPVT system provides to the roof.

TRNSYS components used in the model include the Type-56 Multizone building model based on geometry from a Google Sketchup model using the TRNSYS-3D plugin, a high thermal mass floor slab, and a BIPV/T roof system.

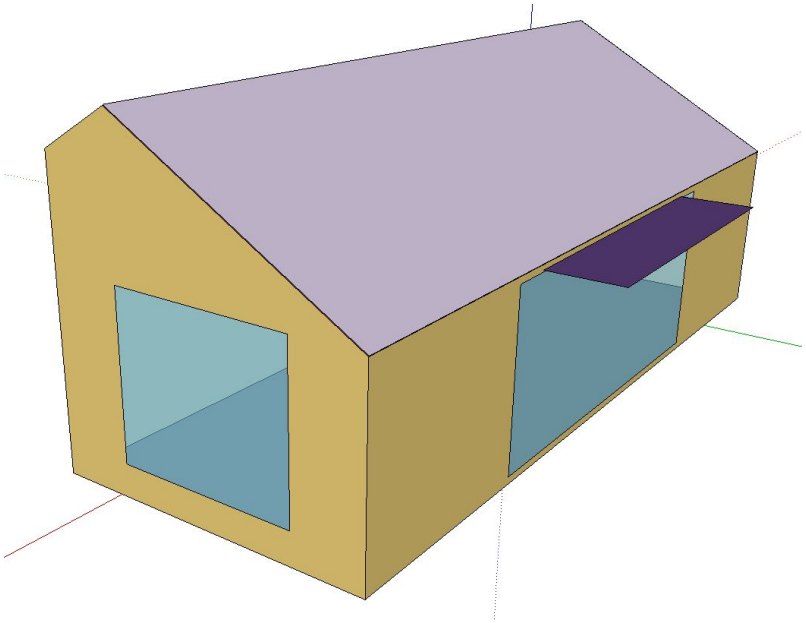

Figure 5.2: TRNSYS-3D model of the transportable building. Shading surfaces are shown in purple.

5.4 Control Strategies

To operate the BIPV/T system efficiently, several control strategies must be put in place. For example, the BIPV/T system should not be operated when the required energy input exceeds the amount of useful energy that the system can output. The motorised flaps in the venting system ensure that the BIPV/T system is only used for heating when the house is cool enough to warrant the heating. Differential controllers introduce a hysteresis effect to limit rapid switching between modes and suitable dead-bands are selected for each control strategy. The general control logic is illustrated in Figure 5.3.

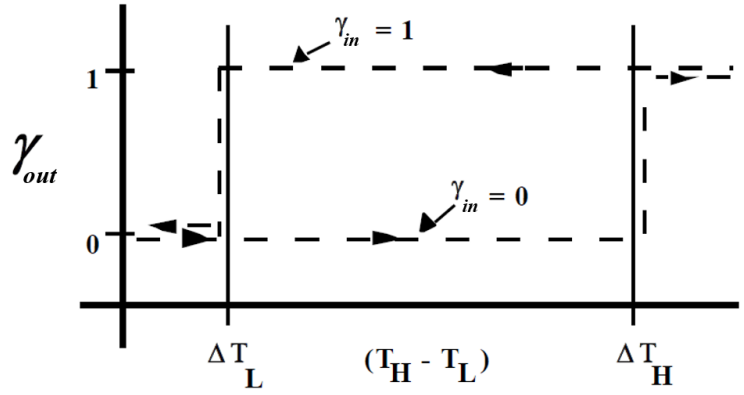

Figure 5.3: General control logic flow chart

To explain Figure 5.3, first note that the x-axis represents a temperature difference, for example, the temperature difference between the room (assigned to T_H), which varies with time, and the desired room temperature (assigned to T_L) which can be assumed constant. Assume that initially $T_H - T_L = \Delta T$ is less than the lower dead-band temperature difference, ΔT_L. This condition corresponds to a control signal $\gamma_{out} = 0$. As the room temperature increases, ΔT increases, and once ΔT exceeds the higher dead-band temperature difference, ΔT_H, the control signal changes from $\gamma_{out} = 0$ to $\gamma_{out} = 1$. The control signal remains at this state until ΔT decreases such that ΔT is less than ΔT_L, at which point the control signal changes from $\gamma_{out} = 1$ to $\gamma_{out} = 0$. This hysteresis effect prevents rapid switching of the control signal.

5.4.1 Operate BIPV/T fan

It has been found empirically that the BIPV/T system only produces economical output when the total electrical output from the integrated PV array exceeds 50% of its rated power. Electrical output P_{elect} is used as the measure as this quantity is readily available through existing data recording systems.

If this condition is met, the fan is turned on to start forcing air through the BIPV/T system. The set point is given by $P_{SET} = 0.5P_{PV,rated}$, and the high (subscript H) and low (subscript L) dead-band radiation values are $\Delta P_H = 50W$, $\Delta P_L = 0W$.

If the fans, which have the subscript F, were previously off, the input fan control state is $\gamma_{in,F} = 0$. Thus the output fan control is:

$$\gamma_{out,F} = \begin{cases} 1 & \text{if } P_{elect} - P_{SET} \geq \Delta P_H; \\ 0 & \text{if } P_{elect} - P_{SET} < \Delta P_H. \end{cases} \tag{5.4.1}$$

In addition, if the fan is currently on, the total incident horizontal radiation is compared to see if it has dropped below $250 W/m^2$. If this condition is met, the fan is turned off to stop forcing air through the BIPV/T system.

If the fans were previously on, $\gamma_{in,F} = 1$:

$$\gamma_{out,F} = \begin{cases} 1 & \text{if } P_{elect} - P_{SET} \geq \Delta P_L; \\ 0 & \text{if } P_{elect} - P_{SET} < \Delta P_L. \end{cases} \tag{5.4.2}$$

Figure 5.4 illustrates the control logic defined by Equations (5.4.1)-(5.4.2):

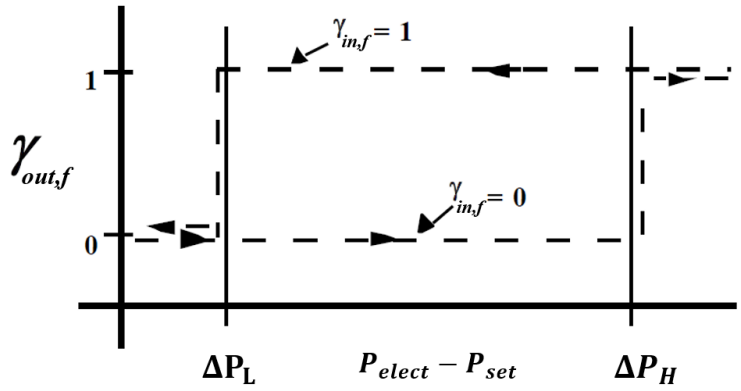

Figure 5.4: Control logic flow chart illustrating Equations (5.4.1)-(5.4.2)

5.4.2 Open/close vents

When the vents are open, corresponding to $\gamma_V = 1$, input air comes from the zone, and output BIPV/T air flows back into the zone. When the vents are closed, corresponding to $\gamma_V = 0$, input air comes from ambient air, and outlet air flows to the atmosphere. See Figures 4.8 and 4.9 for a diagram showing the two venting modes.

Two conditions must be met before the vents are opened to allow air to circulate through the BIPV/T system and building zone in order to raise the zone temperature.

- The fans must be switched on. This criteria ensures that the output BIPV/T air temperature is sufficiently high to have a heating effect, as the fans are only switched on when sufficient solar radiation is available.
- The zone air temperature must be less than the desired set point air temperature. This ensures the room is only heated when required.

Zone air temperature set point

The set point temperature, T_{set}, for the building is chosen to be 20°C. For the case where $\Delta T_L = 0°C$, the heating mode is activated when the zone air temperature drops below the set point temperature. The heating mode is then only switched off when the zone air temperature has reached the upper dead-band switch, $\Delta T_H = 2°C$.

When the heating is mode de-activated, the input temperature control state is $\gamma_{in,T} = 0$, thus the output control state is:

$$\gamma_{out,T} = \begin{cases} 1 & \text{if } (T_{ZONE} - T_{SET}) \geq \Delta T_H; \\ 0 & \text{if } (T_{ZONE} - T_{SET}) < \Delta T_H. \end{cases} \tag{5.4.3}$$

For heating mode activated, $\gamma_{in,T} = 1$:

$$\gamma_{out,T} = \begin{cases} 1 & \text{if } (T_{ZONE} - T_{SET}) < \Delta T_L; \\ 0 & \text{if } (T_{ZONE} - T_{SET}) \geq \Delta T_L. \end{cases} \tag{5.4.4}$$

Figure 5.5 illustrates the control logic defined by Equations (5.4.3)-(5.4.4):

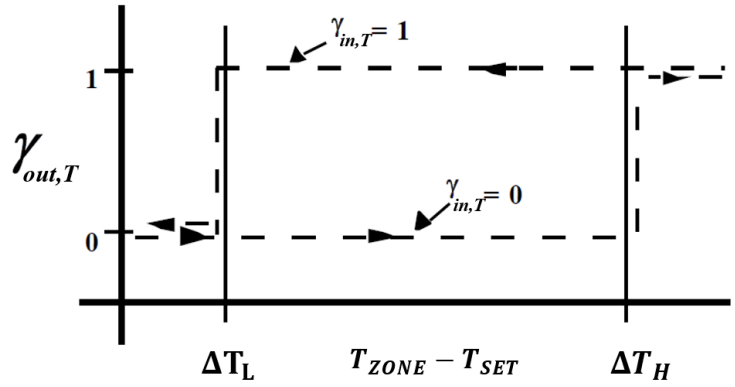

Figure 5.5: Control logic flow chart illustrating Equations (5.4.3)-(5.4.4)

5.4.3 Overall vent control

Finally, the vents are only opened if both of the above conditions are met. The individual dead-bands on each of the temperature and fan control states prevent rapid switching of the overall vent control state.

$$\gamma_{out,V} = \begin{cases} 1 & \text{if } \gamma_{out,T} = 1 \text{ and } \gamma_{out,F} = 1; \\ 0 & \text{if } \gamma_{out,T} = 0 \text{ or } \gamma_{out,F} = 0. \end{cases} \tag{5.4.5}$$

The overall vent logic is summarised by the flowchart of Figure 5.6 as defined by Equation (5.4.5):

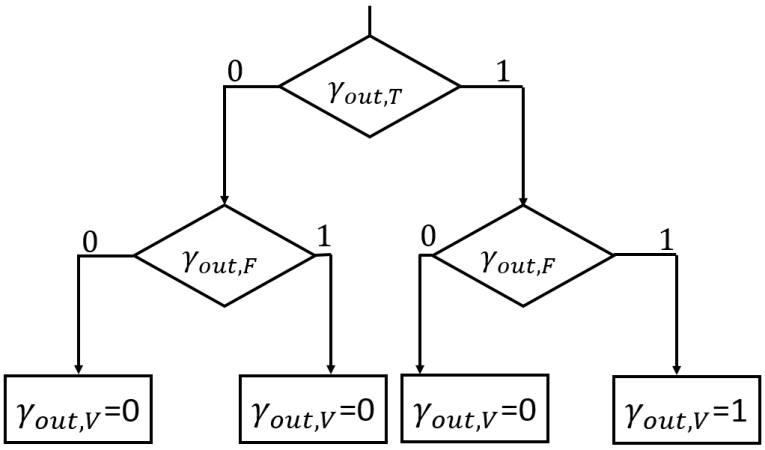

Figure 5.6: Control logic flow chart illustrating Equation (5.4.5)

5.4.4 Heating/Cooling

A simple auxiliary heating device is used to model the auxiliary heating that will exist in the building. This heater will be used to maintain a comfortable room temperature of at least 18°C at all times. A hysteresis controller is implemented which will turn the heater on when the room temperature drops below 18°C and it will turn off when the temperature rises above 22°C.

No active cooling ventilation devices have been included in the initial design, except for a cross-flow heat exchanger, which provides a very cost effective solution. Passive cooling will naturally be performed by the occupants by opening doors and windows during the warmer months to cool the building. This behaviour is reflected in simulations by increasing the air changes per hour of ambient infiltration when the internal zone temperature exceeds the cooling set point temperature of $25°C$.

5.5 Long Term Thermal Performance

Long term simulations are now performed with the control strategies described in Figures 5.3 through 5.6.

The basic thermal performance can be summarised in the daily average temperatures of the building air zone. Figure 5.7 shows comfortable air temperature trends through the year, reaching minimum daily averages of $16°C$

during the coldest months, and staying below $30°C$ during the peak of summer.

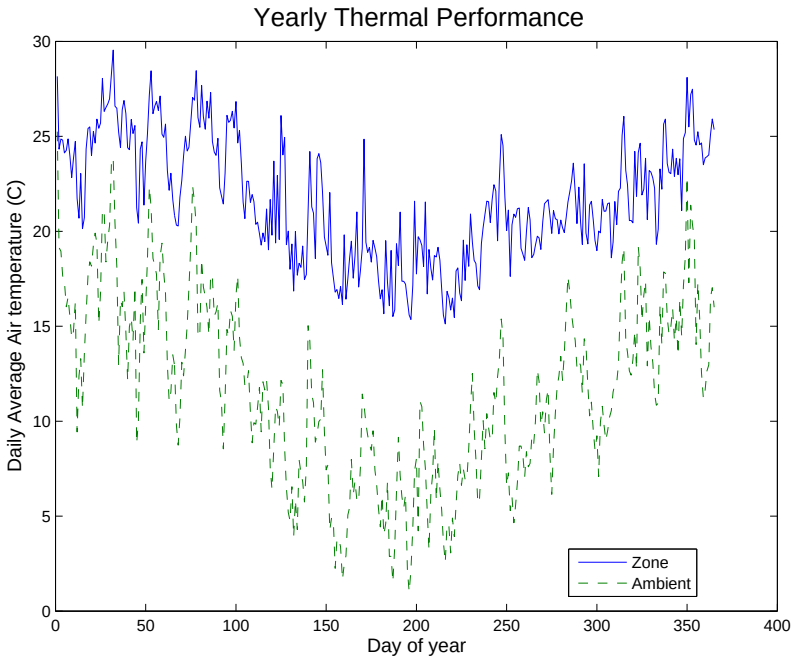

Figure 5.7: Daily average internal zone temperatures compared with ambient temperature

5.6 Building Design Optimisation

This long-term thermal performance simulation can be used to investigate several parameter studies of different aspects of the building design. Two aspects of the building construction are analysed in detail using a TRNSYS simulation. Firstly, the effect of thermal mass on the building's yearly zone temperatures and heating load is investigated, and secondly the optimal window allocation is calculated.

5.6.1 Effect of Building Thermal Mass

The effect of thermal mass can be analysed through the power of yearly simulations with various amounts of thermal mass allocated to the floor slab. Extensive research has proven that higher thermal mass in buildings results

in a moderation of building air temperatures, with cooler temperatures in summer and warmer temperatures during winter. This behaviour is due to the ability for the building to store heat when required, and avoid uncomfortable over-heating (Kalogirou et al. 2002).

To isolate the effect of thermal mass on building temperatures, the auxiliary heater is disabled. With no auxiliary heating, in summer, the building temperatures are on average higher and in winter the temperatures are on average lower.

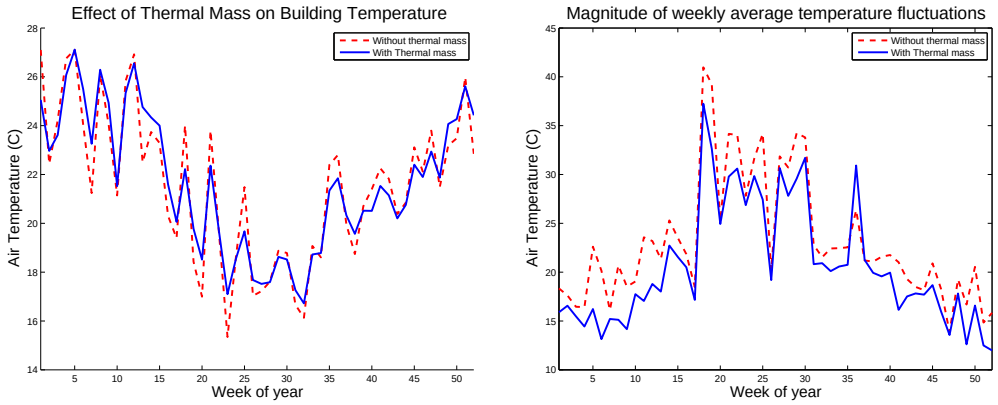

Figure 5.8: (a) Daily average zone temperatures. Auxiliary heater disabled (b) Magnitude of difference between daily maximum and minimum zone temperatures

Figure 5.8(a) shows weekly averaged zone temperatures for the building with a specified amount of thermal mass in the floor slab, and another building with very little thermal mass in the foundation. The building with thermal mass has far superior temperature modulation, with less severe fluctuations between maximum and minimum temperatures.

Figure 5.8(b) shows a plot of the difference between peaks over time for each case. The median fluctuation for the building with thermal mass is 10.2K with a 90^{th} percentile of 18.7K, compared to a median and 90^{th} percentile of 11.1K and 19.9K for the building without thermal mass.

With the $1kW$ auxiliary heater on, the building temperatures are still able to be maintained to a comfortable level. Without thermal mass however, the heating load for the building increases by 10.8% over one year.

Window type	**U-value** $[W/m^2.K]$	**G-value** [%/100]
Single glazed	5.74	0.870
Double glazed	2.95	0.777
Triple glazed	2.00	0.700

Table 5.2: Window specifications

5.6.2 Window Design Analysis

It is of interest to investigate how the total area of windows, placement of windows, and type of windows affects the total yearly heat gain due to solar radiation and heat loss due to transmittance of heat through the building materials.

Moving from single glazed windows to double and triple glazed windows, the solar heat gain coefficient decreases, but the thermal resistance increases. These two characteristics - solar heat gain and thermal heat loss - are both beneficial and detrimental in different seasons depending on the thermal requirements of the building. Yearly simulations carried out in TRNSYS assist in making the best window choice for the building.

The effect of having a relatively small area of window on the east and west walls and the majority on the northern wall is compared to the allocation of all windows on the northern wall.

Window characteristics

Single, double and triple glazed windows are compared in the concept house. Custom window types are specified in TRNBUILD. Key window characteristics for various window types are the U-value $[W/m^2.K]$, overall heat loss coefficient, and G-value, the solar heat gain coefficient (SGHC).

Yearly simulations for the concept house are performed for six separate cases: single, double and triple glazed with windows on N $[9m^2]$, W $[3.6m^2]$, E $[0.9m^2]$ walls, and single, double and triple glazed with windows on only N $[13.5m^2]$ walls. For each case, the solar radiation absorbed into the building due to the transmission through the windows, and the heat loss through the window surfaces was compared. The net gain is the summation of the solar radiation absorbed minus the heat loss. The results are shown in Figure 5.9:

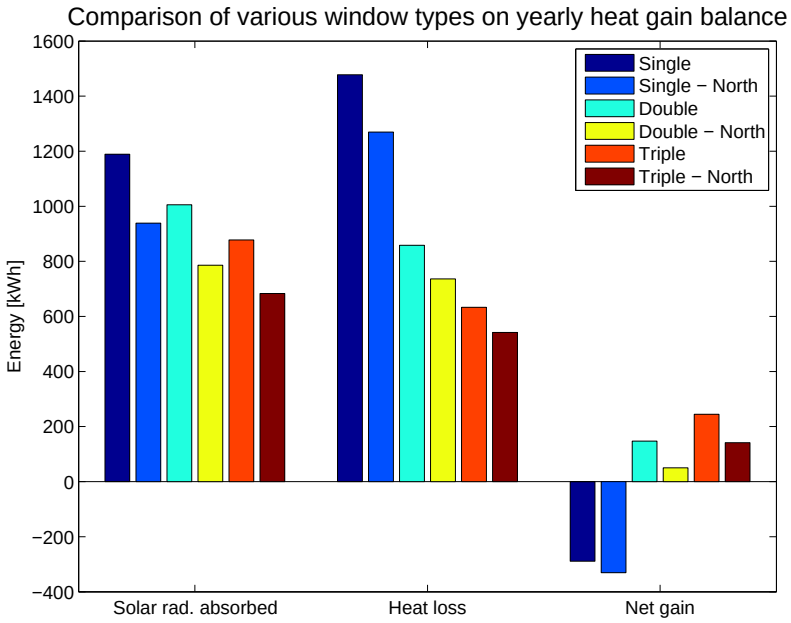

Figure 5.9: Yearly net gain for single, double and triple glazed windows for two window distributions.

The original hypothesis that moving all windows to the northern face of the building would lead to greater net gains than distributing the windows between the west, east and northern walls is shown to be invalid. For each single, double and triple glazed windows, distributing the windows between the three orientations leads to a better overall net gain. Triple glazing is shown to be the best performer as expected, however the extra cost of triple glazing is in many cases prohibitive.

It is therefore more effective to invest in good curtains than to upgrade from double to triple glazing. Greater solar gains are to be made during the day with double glazing, and curtains will provide the additional thermal resistance to heat loss during the night.

5.7 BIPV/T Design Optimisation

The next step is to minimise the deficit between BIPV/T energy gain and energy required. In other words, to maximise the fraction of yearly energy requirements that the BIPV/T system can satisfy.

Building energy requirements

The yearly electrical and heating requirements vary greatly through the year with a larger quantity of energy needed during the colder, darker months. This information would thus allow the optimum design parameters to be determined that minimise the year round energy deficit. Figure 5.10 shows the proportion of total energy usage for an average New Zealand household (BRANZ 2006). Energy usage also varies throughout New Zealand, generally increasing further south due to colder temperatures. The average electrical energy usage per occupant in Christchurch is $2900kWh/year$ (BRANZ 2006). Figure 5.10 shows the monthly variation in energy use for space heating, hot water, lighting and cooking. During winter, water heating usage increases by 60%, and cooking by 50%.

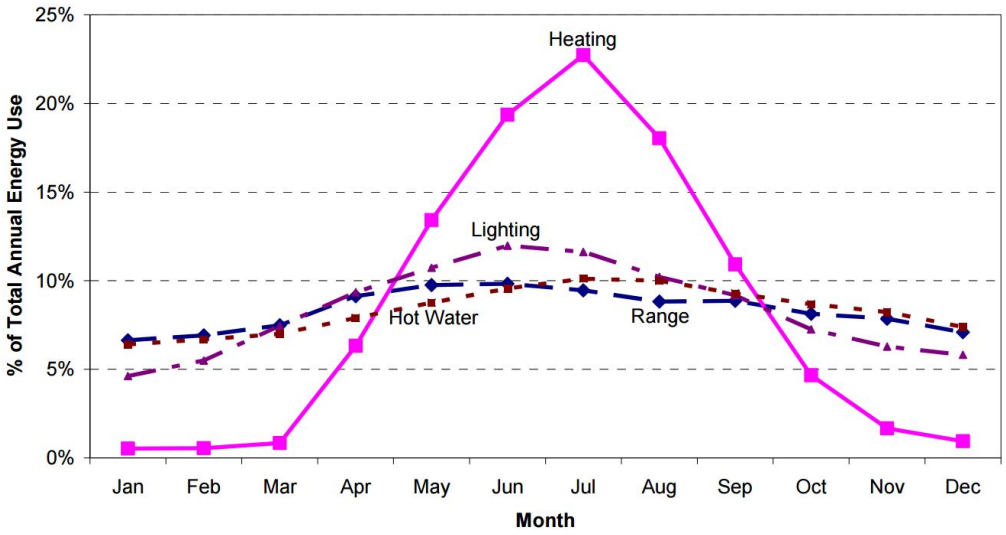

Figure 5.10: Energy use by end-use per month for average NZ household (BRANZ 2006).

Optimisation objective function

The objective function for this optimisation can now be defined as the yearly deficit between the energy requirements and energy gains.

$$\begin{aligned} &\text{minimize} && \left[\left(\frac{Q_{req} - Q_{gain}}{Q_{req}}\right)\right] \\ &\text{subject to} && Q_{req} > Q_{gain} \end{aligned}$$

where Q_{gain} is the overall balance of thermal gain, electrical gain and fan work as given in Equation (2.7.1). Each of these quantities has inherent dependencies on the BIPV/T parameters of channel height, tilt angle and flow rate, which are the three key features of the design to be optimised.

5.7.1 Optimal BIPV/T angle

The fixed tilt angle for a BIPV/T system has a large influence on the seasonal variation of total energy that can be gained. The optimal angle for electrical gain is well known as a rule depending on the latitude of the location. However, the optimal angle for thermal gain is not well researched and could potentially differ from the optimal electrical angle. The tilt angle also affects the flow rate during natural ventilation due to either wind or buoyancy effects. This analysis seeks to find the angle which covers the greatest proportion of the yearly energy requirements.

Results

TRNSYS simulations are performed for a range of tilt angles between $0° - 90°$. The hourly electrical and thermal energy gains are recorded for a one year period. These gains are integrated monthly, and for each month, the tilt angle which corresponds to maximum energy produced is recorded.

Figure 5.11 provides a useful reference for design to show the optimal angle of a BIPV/T system for each month of the year. The optimum tilt angle varies between 20° in the summer season, and about 60° during the winter months.

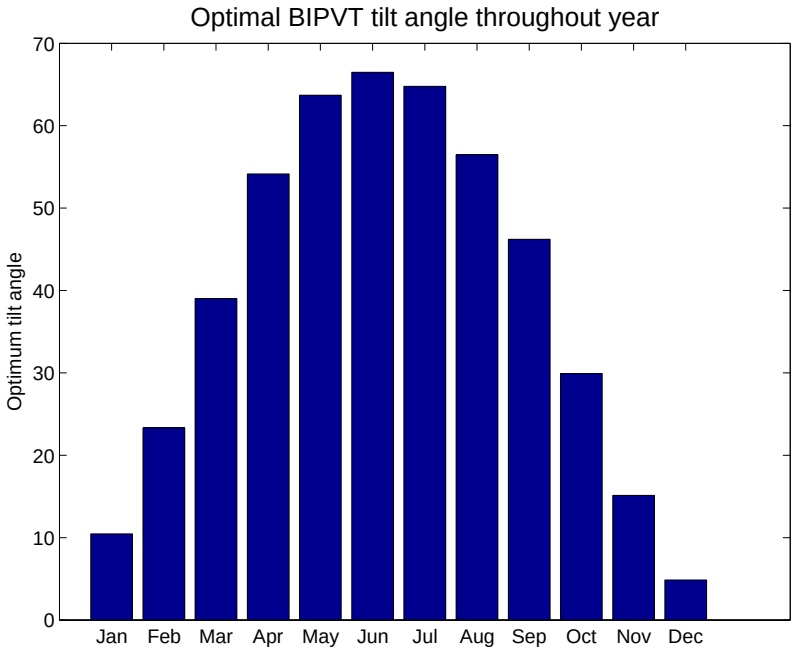

Figure 5.11: Monthly optimal angle for BIPVT gain

However, as the angles chosen for a building design must be fixed year-round, the optimal angle minimises the deficit between the total gains of the system and the energy requirements of the building over a whole year. Figure 5.12 shows the yearly energy requirement met by the BIPV/T system for a range of tilt angles.

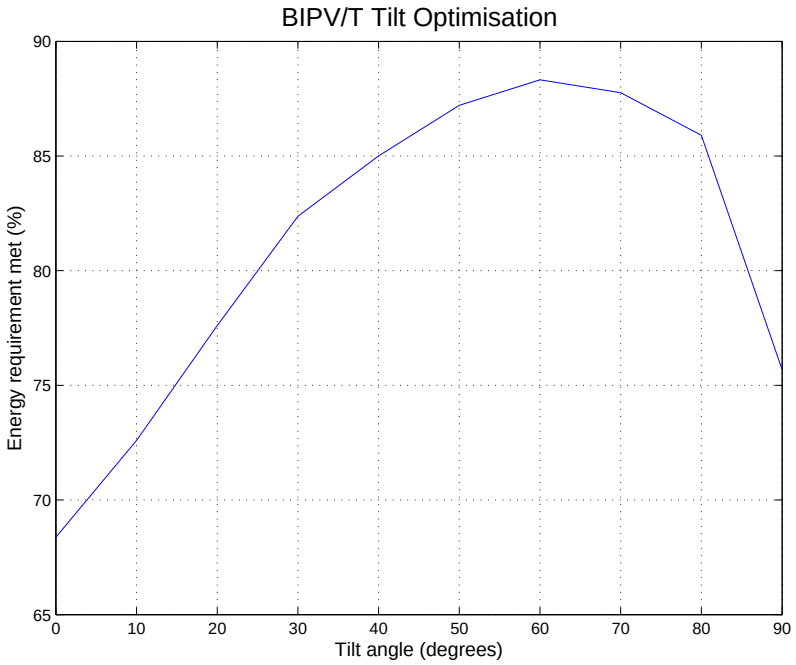

Figure 5.12: Fraction of yearly energy requirements met by BIPV/T system for a range of tilt angles.

The tilt angle significantly affects the percentage of energy requirements that are satisfied, with an additional 9% of energy at 60° tilt compared to the standard 20° tilt angle.

However, building regulations and design aesthetics restrict the allowable angle for a real building. Steep roofs are in many cases not practical. The Chapman Castle combines both vertical PV modules on northern walls with tilted PV modules on the 30° roof. This concept works well at the Chapman Castle for year round production, with the vertical surfaces enhancing winter thermal gains, and tilted surfaces maintaining high electrical gains year-round. This could work well in future iterations of this transportable building design.

5.7.2 Optimal channel depth

The height of the ducting between the PV surface and lower insulation surface is an important design consideration for a BIPVT system. A smaller channel depth will result in greater heat transfer, but will require greater fan work to overcome frictional losses. Hegazy (1999) claims that a general optimum

channel height to length ratio for solar air heaters under variable air flow rates exists and is defined:

$$\left(\frac{D}{L}\right)_{opt} = 2.5 * 10^{-3} \tag{5.7.1}$$

This general rule of thumb will be tested for the case of a BIPV/T system using yearly TRNSYS simulations over a range of channel depths for a constant mass flow rate.

Thermal benefit

The thermal benefit due to a lower channel height can be explained by the non-dimensional Nusselt number. According to the definitions of the Nusselt number in Equation (4.10.3) in section 4.10.2, the relationship between the heat transfer coefficient h and the channel height h_{CH} can be derived. Since the mass flow rate is kept constant, the Reynolds number $Re = \frac{4\dot{m}}{\mu\pi D_h} \propto 1/D_h$, and the heat transfer coefficient is defined:

$$h \propto \frac{Nu}{D_h} \propto \frac{Re^{0.8}}{D_h} \propto \frac{\left(\frac{1}{D_h}\right)^{0.8}}{D_h} \propto D_h^{-1.8} \tag{5.7.2}$$

The hydraulic diameter (D_h) increases almost linearly with channel depth (h_{CH}). Thus, Equation (5.7.2) shows that the heat transfer coefficient decays like the channel depth to the power of -1.8. In other words, the heat transfer between the PV surface and the air stream is much greater for a low duct than a high duct.

5.7.3 Results

The competing effects of frictional losses versus thermal gains can be qualified with the use of yearly simulation. A series of TRNSYS simulations are performed for a varying channel height, with all other variables held constant. The range of interest of channel heights for the BIPV/T system is $0.05m - 0.2m$.

Figure 5.13 shows that for this system, the optimal channel height is approximately $0.09m$. This height aligns closely with the claims made by Hegazy

(1999) summarised by equation 5.7.1, which predicts an optimum channel depth of $0.085m$.

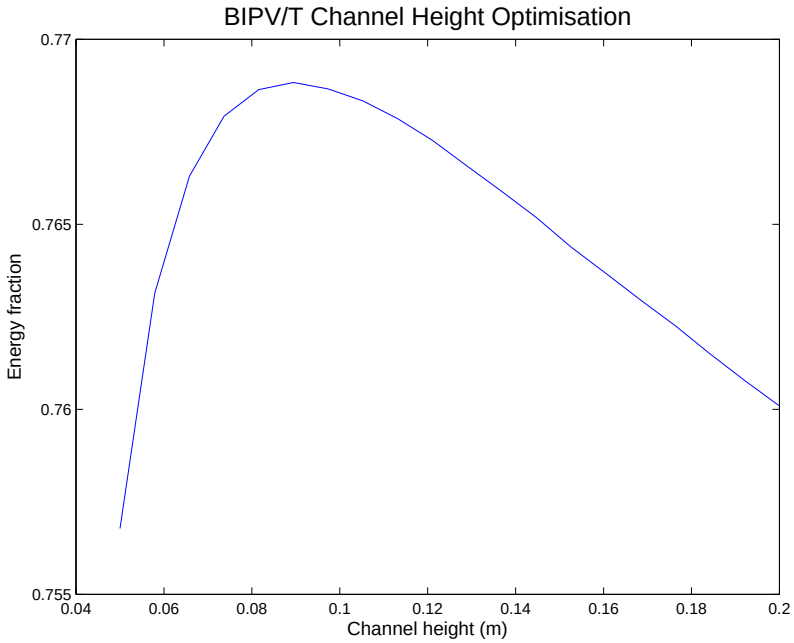

Figure 5.13: Yearly energy fraction variation with channel height

5.8 Final thermal performance

Figure 5.14 shows the monthly variation of thermal and electrical gains from the BIPV/T system, as well as a total energy gain curve (blue). The total required energy input is shown, which includes the auxiliary heating supplied to the building to maintain the desired set point temperature and the electricity for lighting and miscellaneous appliances.

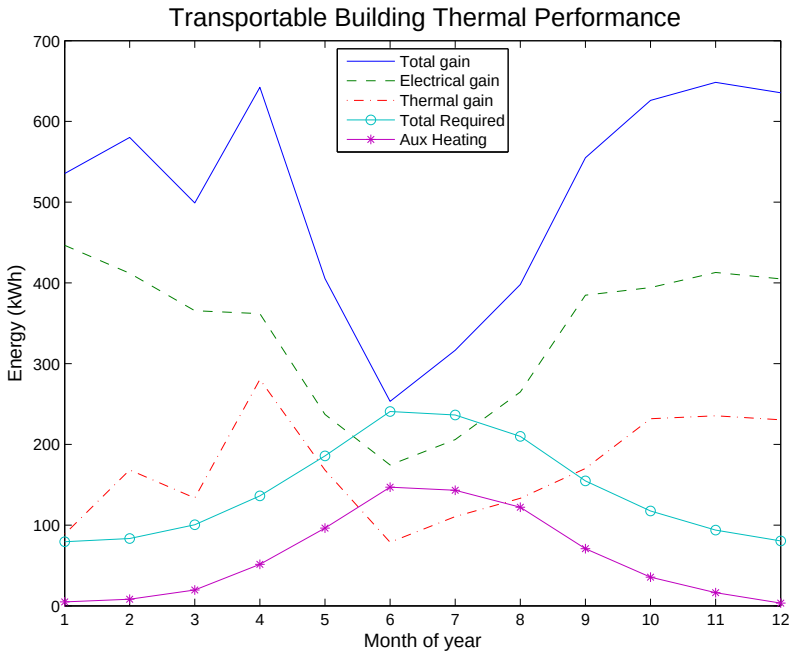

Figure 5.14: Monthly energy gains compared with requirements

The quantity of thermal heat gain from the BIPV/T system is the amount introduced into the building as a result of the various control strategies as described in Figures fig:controllogic2-fig:controllogic4 in section 5.4. It can be seen that the BIPV/T system is most effective in the autumn and spring months due to the requirement for heat due to colder ambient temperatures, and relatively good solar incidence angles and daylight hours. In winter, the thermal gains cover approximately one third of the total heating requirement, and the remainder is made up by the auxiliary heater.

5.8.1 Yearly savings

Economic analysis is an important final stage in evaluating the economic benefit of the BIPV/T system. Assuming an occupancy of two persons in this building, the total energy requirement is $6000kWh$ (BRANZ 2006). Figure 5.10 is used to estimate the yearly distribution of energy requirements throughout the year for lighting, cooking, hot water and other appliances. Yearly simulations are performed for the building using the optimal flow rate and optimal year-round tilt angle. The monthly distribution of thermal and electrical savings are then compared to the total year-round requirements.

A cost of $0.26 per kWh is assumed for the following calculation of energy savings, which allow the pay-back period for the system to be evaluated.

Electrical

The total quantity of electrical power production for one year is 5200 kWh. The total amount of this electrical energy that is used to operate the fans is 187 kWh. The net amount of electrical gain equates to a yearly saving of $1057 per year.

However, with uncertainty around energy prices and production in the future, solar energy is becoming more important. There are also many benefits with solar that cannot be valued monetarily, including independence from the grid, lower environmental impact, and self-sufficiency.

Thermal

Thermal energy savings are calculated by performing whole building simulations for the BIPV/T system on and off. The effective temperature rise due to BIPV/T system over the course of the year, subject to control mechanisms is totalled and an equivalent electrical saving for heating energy is estimated. This estimate is based on the auxiliary electrical energy that would be required to bring about the same change. The total amount of energy replacing auxiliary heating using the BIPV/T system is $500kWh$ across the whole year, equivalent to a yearly saving of $130. Additionally, if excess heat that is not required to heat the building is used to contribute to pre-heating water in the house with a heat-pump system, the BIPV/T has the potential to contribute a further 1530 kWh, equivalent to a saving of $400.

Pay-back period

The overall pay-back period for the BIPV/T system must take into account the cost of the complete PV system, extra materials used to construct the air ducts, and the savings made by not using standard roofing materials.

The number of 250W panels chosen in this design was 18, with total associated cost of $24,300, including a PV inverter, batteries and installation.

The extra cost of BIPV/T components include the ducting materials and fan units, estimated to cost $1400.

Savings made by replacing standard roofing materials with the PV system, assuming a cost of $\$9/m^2$ for roofing materials, are estimated at $3000.

The total cost is therefore $22,700. Yearly energy savings due to the BIPV/T system are $1180 for space heating only, and $1580 with space heating and water pre-heating. The pay-back period for the system is 19.2 years and 14.4 years respectively.

5.8.2 Commercial validity

The analysis in this section will be of use to StoneWood Homes to determine the commercial validity of this transportable building concept.

It has been shown through TRNSYS simulation that the additional thermal mass in the building reduces the severity of temperature fluctuations, and maintains warmth during winter. This effect, combined with excellent insulation, contributes to a more comfortable home environment.

The savings in space heating due to the BIPV/T system in the current design are low, and the design must be reviewed if the full potential of the BIPV/T system is to realised. The reason for the small savings in the current design is due to the tilt angle of the roof optimised for summer conditions, when very little energy is required. The future challenge is to incorporate a steeper roof angle into a traditional style building without sacrificing aesthetics.

The calculations above show that the BIPV/T system would be far better utilised with a heat-pump system for pre-heating water as implemented at the Chapman Castle, a move that would reduce the overall pay-back period of the system by 5 years.

Most promising from the results and the biggest driver for sales is that it is feasible the building could achieve 100% energy self-sufficiency across the year and not require back-up supply from the grid.

The major selling point for this StoneWood Homes design is that there is no other competing product on the market offering an all-inclusive, stand-alone building product. Therefore customers will be willing to pay a premium, since it is the first of its kind in New Zealand.

5.9 Conclusion

In this chapter, the transportable building conceptual design has been analysed in detail, with key design features described, and detailed thermal modelling performed. TRNSYS thermal modelling has been used to optimise various components of the design, including window distribution, building thermal mass, air flow rate through the BIPVT system and PV tilt angle. Control strategies were designed and implemented in simulations to ensure optimal operation of the BIPVT system depending on the building state and weather conditions. Long term thermal performance was evaluated using a TRNSYS simulation, and the overall thermal and electrical energy savings were determined based on estimated energy requirements. The commercial validity of the building was discussed.

Chapter 6

Conclusions

In this research, a comprehensive study of a building integrated photovoltaic thermal system has been carried out. A thermal energy model for the BIPV/T system and for the building envelope has been developed and validated using TRNSYS software to simulate the long-term performance of the overall system.

The TRNSYS transient system simulation software proved to be an effective tool to organise system components in a modular way, and to allow for a range of simulation methodologies: validation, optimisation and evaluation of long-term performance.

Numerous other engineering techniques supported the model development, both experimental and numerical.

An experimental apparatus was constructed, replicating the thermal behaviour of the Chapman Castle BIPV/T system. This test rig showed that a significant quantity of thermal heat energy could be transferred from a heated PV cell with an air stream, producing a signifcant temperature rise in both the air and water streams. The system was capable of overall efficiencies of up to 53% during autumn conditions. These experiments further validated the concept of BIPV/T and highlighted the potential for integrating this system onto buildings to supply both electrical and thermal energy. An optimal flow rate for this system was determined based on an energy balance approach.

Extensive data was collected from the Chapman Castle's various systems for validation of the model. A sensitivity analysis was performed to highlight the most influential model parameters of the simulation results. Further

experiments were then carried out to improve the prediction or measurement of these parameters. The tracer-gas method was used to measure the building infiltration rate which was correlated against wind speed to produce a better fit.

A computational fluid dynamics analysis was performed to study in finer detail the thermal and hydraulic implications of the unique BIPVT air duct geometry implemented at the Chapman Castle. Results showed a much higher heat transfer coefficient between the heated PV surface and air stream, and pressure-flow rate curves rate the extra effort required by the fans to overcome the extra friction in the duct. The TRNSYS model was adjusted to take into account the unique geometry by altering the channel height and keeping air flow rates constant. This approach improved the results of the validation study by a small yet measurable amount.

Validation of the TRNSYS model for both the building and BIPV/T systems were completed. An overall system validation involving the BIPV/T system linked with the building model was completed. Control strategies were implemented governing the operation of the BIPV/T motorised flaps and fans. Results showed satisfactory correlation for use in long-term simulations. The yearly performance and energy savings due to the BIPV/T system were evaluated.

A new transportable low-energy building concept designed by fellow Master's student Sean Cooney and was investigated using TRNSYS. Simulation results assisted with optimisation of the building design, indicating the relative thermal performance of various building materials, structural arrangements, and BIPV/T system configurations. The window arrangement was verified, and effect of the thermal mass in the structure justified. The tilt angle for the roof was analysed showing an optimal angle of 60° for optimum year round performance, however practical requirements were acknowledged. Optimisation for the BIPV/T system was carried out with respect to monthly energy requirements. The optimum channel depth was determined to be 90mm, which aligns closely with literature.

The various techniques used in this thesis has shown that it is possible to predict with sufficient accuracy the thermal performance of these systems leading to the development of an optimum design for any specific application.

Overall, photo-voltaic thermal systems present a cost-effective way to boost the combined thermal and electrical efficiency of a standard solar PV panel when integrated into a building structure. Yearly savings are shown to minimal using thermal gains for space heating alone for buildings with low roof

tilt angles. Savings could be greatly increased by using excess heat at other times in the year for water pre-heating to maximise utilisation of thermal gains, which would reduce reliance on other forms of auxiliary energy.

6.1 Future Work

6.1.1 Chapman Castle

Future work to be done for the Castle includes extending the existing model to include thermal analysis of the water-based HVAC systems to improve control strategies and performance. Further carbon-dioxide studies could be conducted to improve the ventilation systems for bedrooms. There is still scope for improvement in the validation of the building model and the overall system model. More advanced techniques are required to analyse the interactions between the thermal mass of the building and the air temperature. The distribution of thermal mass throughout the zone could be modelled in more detail to first validate the concrete temperature distribution. More measurements for each of the individual building surfaces in each zone would assist the calibration of the model for each component of the building structure. The constant damping coefficient for temperature rise and decay could be re-modelled to show piecewise behaviour, better representing the thermal inertia of the system, as shown in Figure 6.1. The term in the TRNSYS formulation that needs to be investigated is Q_{surf} (see Appendix C), which calculates the heat transfer due to internal convection from building surfaces to the inside air temperature.

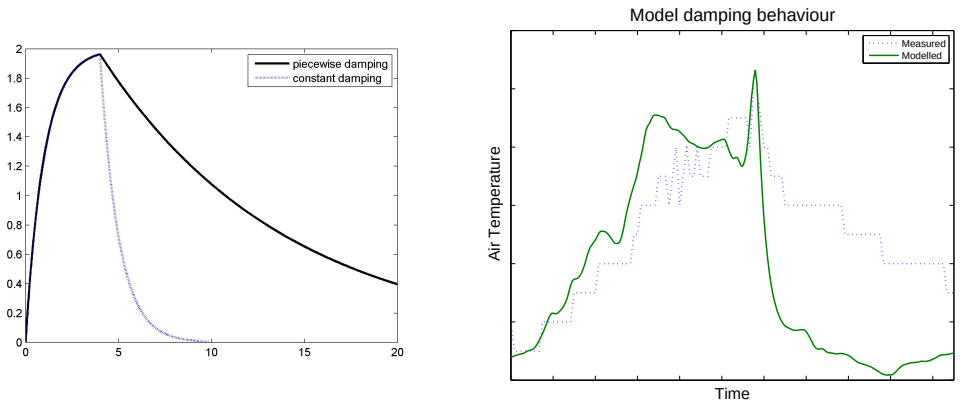

Figure 6.1: (a) Comparison of constant and piecewise damping coefficients (b) Behaviour of current model versus measured data

6.1.2 Transportable Building

The transportable building described and modelled in Chapter 5 is due to be constructed by the end of 2015 by Sean Cooney in association with StoneWood Homes and DARC Technologies. Upon completion of the construction of the first prototype of this building, a similar process as carried out in Chapter 4 will be conducted for this new building. A full validation of the transportable building's performance with real data will allow for much more accurate prediction of this product's performance and market value. Further optimisation of the design and control strategies will also be possible. Until then, an uncertainty analysis should be performed on the current predictions to show how robust the optimal design is to uncertainty in the model parameters. A more detailed economic analysis for the building design would be very useful to market the product as a whole, by considering the life-time savings of the BIPV/T system to calculate a more accurate payback period. This analysis could easily be reproduced for different locations around the world, for example Africa or the Pacific, where there is a greater solar resource.

Bibliography

Anderson, T. N. (2009), Investigation of thermal aspects of building integrated photovoltaic/thermal solar collectors, PhD thesis, The University of Waikato.

Bazilian, M. D., Leenders, F., van Der Ree, B. & Prasad, D. (2001), 'Photovoltaic cogeneration in the built environment', *Solar Energy* **71**(1), 57–69.

BRANZ (2006), Energy use in nz households, Technical Report SR 155, Department of Computer Science, Michigan State University, East Lansing, Michigan.

Candanedo, L. M., Athienitis, A. K., Candanedo, J. A., O'Brien, W. & Chen, Y. (2010), 'Transient and steady state models for open-loop air-based bipv/t systems.', *ASHRAE Transactions* **116**(1).

Chapman, D. (2010), *Designing the Castle*, DARC Technologies Ltd., Tai Tapu, Christchurch, NZ.

Chen, Y., Athienitis, A. & Galal, K. (2010), 'Modeling, design and thermal performance of a bipv/t system thermally coupled with a ventilated concrete slab in a low energy solar house: Part 1, bipv/t system and house energy concept', *Solar Energy* **84**(11), 1892–1907.

Diarra, D., Candanedo, L., Harrison, S. & Athienitis, A. (2008), 'An experimental investigation of air flow and heat transfer in roof-integrated photovoltaic thermal systems'.

Duffie, J. A. & Beckman, W. A. (2013), *Solar engineering of thermal processes*, John Wiley & Sons.

Emmel, M. G., Abadie, M. O. & Mendes, N. (2007), 'New external convective heat transfer coefficient correlations for isolated low-rise buildings', *Energy and Buildings* **39**(3), 335–342.

ENERGYAE (2015), 'Energy analysis and engineering consultants'.
URL: *http://energyae.com/*

Estep, G. M. (2013), Low-Cost Building-Integrated Photovoltaic/Thermal Module Prototype Design and Analysis, PhD thesis, UNIVERSITY OF COLORADO AT BOULDER.

Fabriek, P. (2013), Sensitivity analysis of residential building simulations: Model choice for specific applications and critical parameters, PhD thesis, TU Delft, Delft University of Technology.

Farshchimonfared, M., Bilbao, J. & Sproul, A. (2015), 'Channel depth, air mass flow rate and air distribution duct diameter optimization of photovoltaic thermal (pv/t) air collectors linked to residential buildings', *Renewable Energy* **76**, 27–35.

Han, G., Srebric, J. & Enache-Pommer, E. (2015), 'Different modeling strategies of infiltration rates for an office building to improve accuracy of building energy simulations', *Energy and Buildings* **86**, 288–295.

Hegazy, A. A. (1999), 'Optimum channel geometry for solar air heaters of conventional design and constant flow operation', *Energy conversion and management* **40**(7), 757–774.

Jones, G. (2014), Using fans in series and parallel: Performance guidelines, Technical report, ebmpapst.

Jones, M. (2010), *Coupling TRNSYS and MATLAB for genetic algorithm optimization in sustainable building design*, na.

Kalogirou, S. A., Florides, G. & Tassou, S. (2002), 'Energy analysis of buildings employing thermal mass in cyprus', *Renewable Energy* **27**(3), 353–368.

Liao, L., Athienitis, A., Candanedo, L., Park, K.-W., Poissant, Y. & Collins, M. (2007), 'Numerical and experimental study of heat transfer in a bipv-thermal system', *Journal of Solar Energy Engineering* **129**(4), 423–430.

Lomas, K. J. & Eppel, H. (1992), 'Sensitivity analysis techniques for building thermal simulation programs', *Energy and buildings* **19**(1), 21–44.

Malik, N. (1978), 'Field studies of dependence of air infiltration on outside temperature and wind', *Energy and Buildings* **1**(3), 281–292.

Mara, T. A., Garde, F., Boyer, H. & Mamode, M. (2001), 'Empirical validation of the thermal model of a passive solar cell test', *Energy and Buildings* **33**(6), 589–599.

Ogunsola, O. T., Song, L. & Wang, G. (2014), 'Development and validation of a time-series model for real-time thermal load estimation', *Energy and Buildings* **76**, 440–449.

(SEL), S. E. L. (2007), *TRNSYS 17 User Manuals*, Solar Energy Laboratories, Madison.

Solanki, S., Dubey, S. & Tiwari, A. (2009), 'Indoor simulation and testing of photovoltaic thermal (pv/t) air collectors', *Applied energy* **86**(11), 2421–2428.

SUNZ (2015), 'Solar energy specialists'.
URL: *http://www.sunz.co.nz/*

Sweet, M. L. & McLeskey Jr, J. T. (2012), 'Numerical simulation of underground seasonal solar thermal energy storage (sstes) for a single family dwelling using trnsys', *Solar Energy* **86**(1), 289–300.

Tiwari, A., Sodha, M., Chandra, A. & Joshi, J. (2006), 'Performance evaluation of photovoltaic thermal solar air collector for composite climate of india', *Solar energy materials and solar cells* **90**(2), 175–189.

TRANSSOLAR (2015), 'Trnsys 3d overview'.
URL: *http://www.transsolar.com/*

Wahab, H., Duke, M., Carson, J. & Anderson, T. (2011), Studies of control strategies for building integrated solar energy system, *in* 'Clean Energy and Technology (CET), 2011 IEEE First Conference on', IEEE, pp. 342–347.

Yakhot, V., Orszag, S., Thangam, S., Gatski, T. & Speziale, C. (1992), 'Development of turbulence models for shear flows by a double expansion technique', *Physics of Fluids A: Fluid Dynamics (1989-1993)* **4**(7), 1510–1520.

Zogou, O. & Stapountzis, H. (2011), 'Experimental validation of an improved concept of building integrated photovoltaic panels', *Renewable Energy* **36**(12), 3488–3498.

Appendix A

Measurement Instrumentation

Measurement Instrumentation

Figure A.1: RC-4H temperature and humidity data logger with LCD display. Blue Jay Technology Co., Ltd.

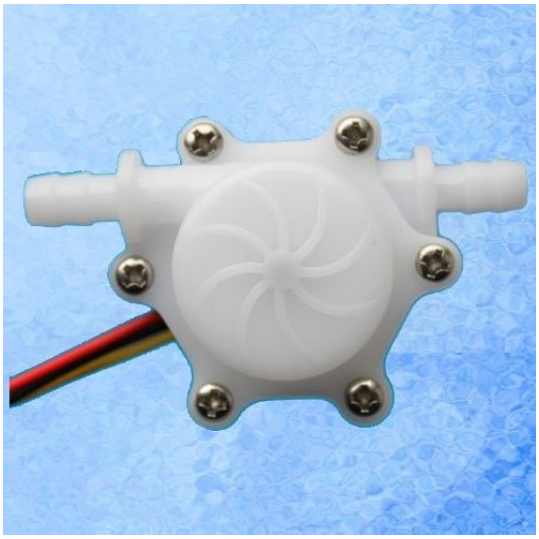

Figure A.2: Water flow sensor

Figure A.3: TES hot wire thermal anemometer with data logging unit (Sparker Instruments 2015)

Figure A.4: Apogee CS300 pyranometer (Campbell Scientific, Inc. 2014)

Figure A.5: CO2 data logger unit

Figure A.6: Wind speed and direction sensor. AliExpress model JL-FSX2

Appendix B

Automation of TRNSYS simulations

The following code automates the TRNSYS simulations in MATLAB. This code is used for the sensitivity analyses and parametric runs in the optimisation studies.

```
% AUTOMATED TRNSYS SIMULATION PROCEDURE %

% This MATLAB script runs a series of TRNSYS simulations automatically,
% changing the value of one parameter for each simulation.
% Author: Alastair McDowell
% Date: January 2015

% Initialise variables
x=linspace(0,1,10); % Variable parameter
resnorm=zeros(size(x)); % Initialise residual norm vector for results
deck_directory = 'C:\deck_file.dck'; % TRNSYS input file directory
parameter_number = 1;

% Loop through all values of the variable parameter 'x'
for i = 1:length(x)

    % Find substr that matches the line for 'parameter_number'.
    if parameter_number == 1
        oldsubstr =         '0.9        ! emissivity';
        newsubstr = sprintf('%.2f       ! emissivity',x(i));
    end
    % [Abbreviated - one if-end statements for each parameter]

    % Read in existing deck file
```

```
    fin = fopen(deck_directory);
    % Open output file to write new deck file
    fout = fopen('temp.txt','w');

    % Go through input file looking for a match for 'oldsubstr'.
    % Once found a match, replace line with 'newsubstr'
    while ~feof(fin) % while not at end of file
        s = fgetl(fin); % read line from file, discard newline character
        s = strrep(s, oldsubstr, newsubstr); % replace oldsubstr with newsubstr in
        fprintf(fout,'%s\n',s); % print updated string to new file
    end
    % Copy temporary output file to deck directory
    copyfile('temp.txt',deck_directory);
    % Close files
    fclose(fin);
    fclose(fout);

    % Execute TRNSYS Exe using the dos command with
    % TRNSYS deck file 'GH15.dck'
    % TRNSYS simulation results are written to a text file
    cmnd = sprintf('"C:\TRNSYS17\TRNExe.exe" "%s" /h',deck_directory);
    dos(cmnd);

    % Load TRNSYS simulation results from text file
    data = load('C:\TRNSYS17\TRNSYS_RESULTS.txt');

    % Extract relevant output variable from results data file
    T_simulated=data(:,2);

    % Calculate residual norm between simulated and measured values
    resnorm(i)=norm(T_simulated-T_measured);
end

% Visualise results: plot residual norm vector against value of the
% variable parameter
plot(x,resnorm)
```

Appendix C

Mathematical model of multi-zone buildings

The basis for the mathematical model of the multi-zone building in TRNSYS is an energy balance. Convective heat fluxes from the surfaces of a thermal zone, solar gains, infiltration and ventilation gains, boundary conditions and adjacent zones, and miscellaneous gains including people and equipment) are considered (SEL).

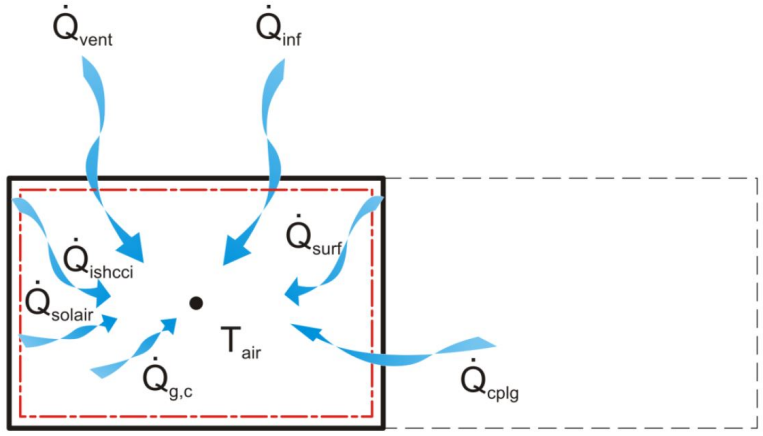

Figure C.1: Heat balance on an air node in a Type 56 building

The overall heat balance equation is:

$$\dot{Q}_{in} = \dot{Q}_{surf} + \dot{Q}_{inf} + \dot{Q}_{vent} + \dot{Q}_{g,c} + \dot{Q}_{adj} + \dot{Q}_{solar} + \dot{Q}_{ISHCC}. \qquad \text{(C.0.1)}$$

where:

$\dot{Q}_{surf}$ is the convective gain from all surfaces surrounding the air node.

$\dot{Q}_{inf} = \dot{V}\rho C_p(T_{outside} - T_{air})$ is the infiltration gain from outside air flow into the zone through gaps in the building envelope.

$\dot{Q}_{vent} = \dot{V}\rho C_p(T_{vent,air} - T_{air})$ is the ventilation gain from a user-defined HVAC air flow source into the zone.

$\dot{Q}_{g,c}$ is the internal convective gain from people, equipment and other internal heat gain sources.

$\dot{Q}_{adj}$ is the convective gain from adjacent thermal air zones.

$\dot{Q}_{solar}$ is the heat gain from solar radiation entering the zone through external windows transferred as convective gain to internal air.

$\dot{Q}_{ISHCC}$ is the absorbed solar radiation on all internal shading devices, such as curtains, which is transferred as a convective gain to the internal air.

Appendix D

Solar geometry

The **hour angle** ω of the sun is the angular displacement of the sun east or west of the local meridian, and can be calculated at any hour h of the day:

$$\omega = \frac{360}{24}(h - 12) \tag{D.0.1}$$

The **declination angle** δ is the angular position of the sun at solar noon with respect to the plane of the equator. This angle changes throughout the year with the rotation of the earth about its axis, and is defined by Cooper (1969) for time in days d:

$$\delta = 23.45^\circ \sin\left(\frac{360}{365}(d + 284)\right) \tag{D.0.2}$$

The **shift in solar time** with respect to local standard time must be accounted for. There are two corrections to be made. The first is constant and depends on the difference between the location's meridian, L_{loc}, and the meridian at which local standard time is taken, L_{st}. The second is the time dependant *equation of time* which relates to the time it takes the sun to cross the observer's meridian. The equation of time is:

$$\begin{aligned} E = 229.2(0.000075 + 0.001868\cos B - 0.032077\sin B \\ - 0.014615\cos 2B - 0.04089\sin 2B) \end{aligned} \tag{D.0.3}$$

where $B = (360/365)(d - 1)$. The total shift in solar time is:

$$SHIFT = Solartime - standardtime = 4(L_{st} - L_{loc}) + E \tag{D.0.4}$$

The angle of incidence θ between the sun direct beam and the normal vector for a general surface at a tilt angle β and azimuth angle γ at a location with latitude ϕ is defined:

$$\begin{aligned}\cos\theta = \sin\delta\sin\phi\cos\beta - \sin\delta\cos\phi sin\beta\cos\gamma + \cos\delta\cos\phi\cos\beta\cos\omega \\ + cos\delta\sin\phi\sin\beta\cos\gamma\cos\omega + cos\delta\sin\beta\sin\gamma\sin\omega\end{aligned} \tag{D.0.5}$$

The solar zenith angle θ_Z is the angle of incidence of beam radiation on a horizontal surface, and can be found using equation D.0.5 by substituting $\theta = \theta_Z$, $\beta = 0$:

$$\cos\theta_Z = \cos\phi\cos\delta\cos\omega + \sin\phi\sin\delta \tag{D.0.6}$$

Finally, the geometric factor R_B can now be calculated as the ratio of beam radiation on the tilted surface to that on a horizontal surface, which reduces down to the cosine ratio between the solar incidence angle and solar zenith angle:

$$R_B = \frac{\cos\theta}{\cos\theta_Z} \tag{D.0.7}$$

Appendix E

BIPVT coefficients

In section 2.6.6, the five energy balances of Equations (2.6.1)-(2.6.8) were solved to form an equation for the useful energy gain $q"_u$, across a differential section of the duct dx, as a function of the air temperature T_{air} in the form:

$$q"_u = aT_{air} + b \tag{E.0.1}$$

where a and b are a collection of the model parameters.

The parameter a is defined:

$$a = -2h_{fluid} + \frac{R_2 h_{fluid}^2}{m} + \frac{h_{fluid}^2}{j} + \frac{2R_2 h_{fluid}^2 h_{rad,1-2}}{mj} + \frac{R_2 h_{fluid}^2 h_{rad,1-2}^2}{mj^2} \tag{E.0.2}$$

The parameter b is defined:

$$\begin{aligned} b = {} & \frac{h_{fluid} h_{conv,back} T_{back}}{jH'} + \frac{h_{fluid} h_{rad,back} T_{back,rad}}{jH'} + \frac{h_{fluid} S}{G'm} + \frac{h_{fluid} h_{conv,top} T_{amb}}{F'G'm} + \\ & \frac{h_{fluid} h_{rad,top} T_{sky}}{F'G'm} + \frac{h_{fluid} R_2 h_{rad,1-2} h_{conv,top} T_{back}}{H'jm} + \\ & \frac{h_{fluid} R_2 h_{rad,1-2} h_{rad,back} T_{back,rad}}{H'jm} + \frac{h_{fluid} h_{rad,1-2} S}{G'jm} + \\ & \frac{h_{fluid} h_{rad,1-2} h_{conv,top} T_{amb}}{G'F'jm} + \frac{h_{fluid} h_{rad,1-2} h_{rad,top} T_{sky}}{G'F'jm} + \\ & \frac{h_{fluid} R_2 h_{rad,1-2}^2 h_{conv,back} T_{back}}{H'j^2 m} + \frac{h_{fluid} R_2 h_{rad,1-2}^2 h_{rad,back} T_{back,rad}}{H'j^2 m} \end{aligned} \tag{E.0.3}$$

Equations (E.0.2) and (E.0.3) are defined using the coefficients F', G', H', j, and m.

F' is defined:

$$F' = h_{rad,top}R_1 + h_{conv,top}R_1 + 1 \tag{E.0.4}$$

G' is defined:

$$G' = \frac{1}{R_1} + \frac{1}{R_2} + \frac{1}{R_1 F'} \tag{E.0.5}$$

H' is defined:

$$H' = 1 + R_3 h_{conv,back} + R_3 h_{rad,back} \tag{E.0.6}$$

j is defined:

$$j = h_{fluid} + h_{rad,1-2} + \frac{1}{R_3} - \frac{1}{H' R_3} \tag{E.0.7}$$

m is defined:

$$m = 1 - \frac{1}{R_2 G'} + R_2 h_{fluid} + R_2 h_{rad,1-2} - \frac{R_2 h_{rad,1-2}^2}{j} \tag{E.0.8}$$